UNIVERSIDADE ESTADUAL DE CAMPINAS

Faculdade de Engenharia Mecânica

MATHEUS BULHÕES BARBOSA

High-resolution microcontroller's based fiber Bragg grating array interrogator

Interrogador de array de grades de Bragg de alta resolução baseado em Microcontrolador

Campinas

2025

MATHEUS BULHÕES BARBOSA

High-resolution microcontroller's based fiber Bragg grating array interrogator

Interrogador de array de grades de Bragg de alta resolução baseado em Microcontrolador

Dissertation presented to the School of Mechanical Engineering of the University of Campinas in partial fulfillment of the requirements for the degree of Master in Mechanical Engineering, in the area of Mechatronics.

Dissertação apresentada à Faculdade de Engenharia Mecânica da Universidade Estadual de Campinas como parte dos requisitos exigidos para a obtenção do título de Mestre em Engenharia Mecânica, na área de Mecatrônica.

Orientador: Prof. Dr. Rodrigo Moreira Bacurau

ESTE TRABALHO CORRESPONDE À VERSÃO FINAL DA DISSERTAÇÃO DEFENDIDA PELO ALUNO MATHEUS BULHÕES BARBOSA, E ORIENTADA PELO PROF. DR. RODRIGO MOREIRA BACURAU.

Campinas

2025

Ficha catalográfica
Universidade Estadual de Campinas (UNICAMP)
Biblioteca da Área de Engenharia e Arquitetura
Rose Meire da Silva - CRB 8/5974

Barbosa, Matheus Bulhões, 2000-
B234h High-resolution microcontroller's based fiber Bragg grating array interrogator / Matheus Bulhões Barbosa. – Campinas, SP : [s.n.], 2025.

Orientador: Rodrigo Moreira Bacurau.
Dissertação (mestrado) – Universidade Estadual de Campinas (UNICAMP), Faculdade de Engenharia Mecânica.

1. Detectores de fibra ótica. 2. Fibras de grade Bragg. 3. Interferômetros de Fabry-Perot. 4. Microcontroladores. I. Bacurau, Rodrigo Moreira, 1988-. II. Universidade Estadual de Campinas (UNICAMP). Faculdade de Engenharia Mecânica. III. Título.

Informações complementares

Título em outro idioma: Interrogador de array de grades de Bragg de alta resolução baseado em microcontrolador
Palavras-chave em inglês:
Optical fiber detectors
Fiber Bragg gratings
Fabry-Perot interferometers
Microcontrollers
Área de concentração: Mecatrônica
Titulação: Mestre em Engenharia Mecânica
Banca examinadora:
Rodrigo Moreira Bacurau [Orientador]
João Marcos Salvi Sakamoto
Anderson Wedderhoff Spengler
Data de defesa: 08-07-2025
Programa de Pós-Graduação: Engenharia Mecânica

Objetivos de Desenvolvimento Sustentável (ODS)
Não se aplica

Identificação e informações acadêmicas do(a) aluno(a)
- ORCID do autor: https://orcid.org/0009-0005-0110-8456
- Currículo Lattes do autor: https://lattes.cnpq.br/6850230388839926

Prof. Dr. Rodrigo Moreira Bacurau, Presidente
DMC/FEM/UNICAMP

Prof. Dr. João Marcos Salvi Sakamoto
EFO/IEAv/DCTA

Prof. Dr. Anderson Wedderhoff Spengler
CEM/UFSC

A Ata de Defesa com as respectivas assinaturas dos membros encontra-se no SIGA/Sistema de Fluxo de Dissertação/Tese e na Secretaria do Programa da Unidade.

ACKNOWLEDGEMENTS

I would like to express my deepest gratitude to everyone who contributed to the successful completion of this project. This journey has been a rewarding experience, and I am thankful for the support and guidance I received.

First and foremost, I extend my heartfelt gratitude to my parents for their consistent support, encouragement, and understanding that has accompanied me throughout my entire college journey, right from the beginning.

To my professor, Rodrigo Bacurau, who provided me with the opportunity and has been a guiding presence throughout these past years. His support, attentiveness, and assistance have been invaluable.

To my lab colleagues, who not only provided multiple occasional assistance but also contributed to creating a more enjoyable and productive work atmosphere.

To all the friends I've made during my entire journey, and whom I plan to remain side by side through all the upcoming ones as well.

To IEAV, which financially supported me throughout this years, and without which this work would not have been possible.

Thank you very much.

RESUMO

Sensores em fibra óptica baseados em Grades de Bragg (FBG) têm recebido ampla atenção na indústria e na academia devido à sua resistência, imunidade eletromagnética, alta sensibilidade, capacidade de operar em ambientes adversos, segurança em atmosferas explosivas e facilidade de monitoramento em múltiplos pontos ao longo de grandes distâncias. Sensores FBG permitem medir, de forma intrínseca, temperatura e *strain*, e, quando acoplados a outros transdutores, podem ser usados para medir tensão elétrica, corrente, pressão, entre outras grandezas. Para extrair a grandeza de interesse, é necessário um interrogador que converta os sinais ópticos refletidos em sinais elétricos. Diversas técnicas de interrogação foram desenvolvidas, com diferentes características de desempenho e custo. Dentre elas, destaca-se o método das Grades Gêmeas, que utiliza uma FBG como filtro para medir a variação no comprimento de onda refletido por uma ou mais FBGs sensoras. Uma variação dessa técnica emprega um filtro de Fabry-Perot sintonizável no lugar da FBG filtro, oferecendo maior faixa de excursão e melhor estabilidade térmica, embora com maior custo. Objetivou-se nesse trabalho simular e projetar um sistema de interrogação para um array de FBGs utilizando as técnicas de grades gêmeas e filtro de Farby-Perot sintonizável. Os principais requisitos deste projeto são: alcançar alta capacidade de excursão (de pelo menos 5 nm - idealmente 100 nm), capacidade de monitorar sinais dinâmicos (com taxa mínima de 50 Hz - idealmente 500 Hz) e alta resolução (de pelo menos 5 pm, idealmente subpicométrica), possibilitando a interrogação de arrays de FBG com alta frequência e resolução. A metodologia adotada incluiu o desenvolvimento de algoritmos de processamento e *firmware* embarcado, a construção dos módulos óptico e eletrônico do interrogador, simulações para análise de ruído e resolução, e testes experimentais para validação do sistema completo. Foram conduzidos testes experimentais para verificar o desempenho do sistema que incluíram ensaios para verificação de resolução em diferentes taxas de aquisição, sensibilidade a variação térmica do interrogador e compensação de histerese da grade filtro. O interrogador desenvolvido neste trabalho mostrou-se capaz de realizar aquisição de array de FBGs com resolução de até 1,5 pm, taxa de até 500 Hz, com baixa sensibilidade a variações de temperatura, demonstrando desempenho similar ao dos principais equipamentos comerciais. Em trabalhos futuros serão desenvolvidas novas técnicas de interrogação de arrays de FBGs com taxa de aquisição superior a 1 KHz e novos atuadores de baixo custo para implementação do filtro sintonizável.

Palavras-chave: Interrogador, Fibra de Grade Bragg, Filtro de Fabry-Perot, Microcontrolador.

ABSTRACT

Fiber optic sensors based on Fiber Bragg Gratings (FBGs) have garnered significant attention in various industrial and academic fields due to their durability, immunity to electromagnetic interference, high sensitivity, ability to operate in harsh environments, safety in explosive atmospheres, and ease of monitoring at multiple measurement points over long distances. FBG-based sensors can intrinsically measure temperature and strain. Additionally, when coupled with appropriate transducers, they can be used to measure variables such as voltage, electric current, pressure, and other physical quantities. To extract the desired measurement from FBG-based sensors, an interrogator is required to convert the reflected optical signals into electrical signals. Several interrogation techniques have been developed, each with different trade-offs between performance and cost. Among them, the Twin Grating method stands out, using a tunable FBG as a filter to track the shift in the reflected wavelength of one or more sensing FBGs. A variation of this technique replaces the tunable grating with a tunable Fabry-Perot filter, offering a wider excursion range and improved thermal stability, albeit at a higher cost. The objective of this work was to design and develop an interrogation system for an array of FBGs using the twin grating technique and a tunable Fabry-Perot filter. The main requirements of this project include achieving a high excursion range (at least 5 nm - ideally 100 nm), the capability to monitor dynamic signals (with a minimum rate of 50 Hz - ideally 500 Hz), and high resolution (at least 5 pm, ideally sub-picometric), enabling the interrogation of FBG arrays with high temporal and spectral precision. The methodology included the development of embedded processing algorithms and firmware, construction of the optical and electronic modules of the interrogator, simulations for noise and resolution analysis, and experimental validation of the complete system. Experimental tests were conducted to assess system performance, including resolution evaluation at different acquisition rates, sensitivity to thermal variations in the interrogator, and hysteresis compensation of the tunable FBG filter. The interrogator developed in this work demonstrated the ability to acquire data from an array of FBGs with a resolution of up to 1.5 pm and acquisition rates of up to 500 Hz with low sensitivity to temperature variations, achieving performance comparable to leading commercial systems. Future work will focus on developing new interrogation techniques capable of operating at rates above 1 kHz and investigating low-cost actuators for implementation of the tunable filter.

Keyword: Interrogator, Fiber Bragg Grating, Fabry-Perot Filter, Microcontroller.

LIST OF FIGURES

LIST OF TABLES

CONTENTS

1 INTRODUCTION

1.1 Contextualization

Optical sensors are devices capable of measuring physical quantities through optical signals. Among the types of optical sensors, the ones based on Bragg grating fibers (FBG) have stood out in recent years. FBGs are structures made by periodic modulation of the refractive index of an optical fiber, resulting in a grating-shaped structure. When light passes through the FBG, part of it is reflected and the other is transmitted. By analyzing the reflected or transmitted spectrum of the FBG, it is possible to obtain information about physical quantities such as deformation, temperature, pressure, among others.

The good attributes of FBG sensors include their intrinsic multiplexing capability, which enables the deployment of multiple sensors on the same optical fiber, separated by distances ranging from a few millimeters to several kilometers. Furthermore, these sensors exhibit immunity to electromagnetic interference, have small dimensions and mass, thereby facilitating their installation in hard-to-reach locations, and can operate safely in environments with flammable materials. Moreover, FBG sensors display high sensitivity and robustness even in harsh environmental conditions (Othonos *et al.*, 2006).

As a result of these characteristics, FBG sensors have garnered significant interest in numerous domains, such as civil engineering, aerospace, and biomedical engineering. For example, in civil engineering, FBGs are used to monitor the structural health of buildings, bridges, and tunnels, and can detect deformations and cracks in these structures (Sahota *et al.*, 2020). In aerospace, FBGs are used to measure strain and temperature in aircraft wings, fuselage, and engines, as well as to monitor the performance of optical fibers in satellite communication systems (Hegde *et al.*, 2022). In biomedical engineering, FBGs are used to monitor vital signs such as heart rate and blood pressure, and can also be used for monitoring the deformation and strain of tissues and organs (Rohan *et al.*, 2023). Overall, FBGs have become a popular choice for sensing applications due to their robustness, high sensitivity, and ability to perform measurements in harsh environments.

In order to enable the utilization of FBG-based sensors, it is typically necessary to convert the optical signal that emerges from them into an electrical signal, a task executed by an interrogator. Over the past few years, a variety of interrogation techniques have been developed,

which vary in terms of the cost associated with their implementation and their performance characteristics, including resolution, sampling rate, susceptibility to interference, noise levels, and others. One particularly notable technique is the Twin-Grating method, which involves the deployment of two FBGs, with one acting as the sensor and the other as the filter. In this technique, the measurement of the optical power of the convolution between the profiles of the two FBGs, usually with one of them being tunable, is utilized to determine variations in the wavelength displacement of the FBG based sensors.

In addition to the Twin-Grating method, another variation of this technique involves the use of a tunable Fabry-Perot filter as a replacement for the tunable Bragg grating. The utilization of a tunable Fabry-Perot filter allows for a wider frequency spectrum excursion, enabling the interrogation of multiple FBGs across a broad operating range. Furthermore, it offers greater thermal stability compared to FBGs. However, it should be noted that the cost associated with a tunable Fabry-Perot filter is considerably higher than that of FBGs.

1.2 Related Works

In this section, we present a review of the works related to Fiber Bragg Grating (FBG) interrogation techniques, exploring different approaches employed in the field of FBG interrogation, aiming to clarify their performance, advantages, and limitations.

1.2.1 Interrogation techniques based on edge fiters

These next works present methods that use edge filters as the core technique for FBG interrogation, converting intensity variations into wavelength. Their simplicity makes them ideal for both static and dynamic sensing applications, particularly when paired with advanced processing techniques.

Fracarolli *et al.* (2019) describes an FBG interrogator with temperature compensation using digital proportional-integral (PI) controllers. The principle of operation involves setting the laser wavelength to the edge of the FBG spectrum, achieving convergence, and then locking the laser to maintain the reflected power. An analog controller and two digital controllers based on a microcontroller are employed. The system successfully compensated for slow temperature changes and detected a 50 kHz acoustic pulse, demonstrating its capability to measure high-frequency signals. This interrogator utilizes a two-stage controller design and the edge-filter technique. In the first stage, the initial wavelength of the laser source is set, while in the second stage, the wavelength is locked to follow the reflected optical power. The system demonstrated its temperature compensation capabilities by maintaining a constant reflected power within a relative error of about 1% despite temperature variations from 25 to 60 ºC. Dante (2016) describes a similar technique of temperature compensation using twin gratings applied for high-voltage monitoring, but instead using a tunable laser, he employed an FBG to operate as a wavelengh filter. However, these techniques are not suitable for the interrogation of FBG arrays since the tunable light wavelengh is locked to a single FBG, which does not allow for a wide wavelength excursion.

Pereira *et al.* (2023) proposed a simple and cost-effective FBG interrogation system using ultra-short fiber Bragg gratings (USFBG) as edge filters. These gratings, produced in silica optical fibers and PMMA microstructured polymer optical fibers, were designed with broader reflection spectra, making them suitable for filtering operations. The system converts wavelength shifts into optical power variations, enabling interrogation with a standard photodetector instead of expensive equipment like optical spectrum analyzers. By determining

the initial position of the FBG's reflected wavelength within the spectrum and monitoring the corresponding power detected by the photodetector, the system can accurately identify both the direction and magnitude of the wavelength variation. The USFBGs, combined with uniform FBGs in a multiplexed configuration, demonstrated high accuracy for dynamic and static sensing applications, with minimal cross-sensitivity to temperature. Furthermore, the proposed system allows for the interrogation of multiple USFBGs along a single fiber. However, this method does not allow for absolute Bragg wavelength determination, only for relative wavelength variation.

Díaz *et al.* (2017) proposed a low-cost FBG interrogation technique for dynamic measurements. The system employs an in-line Fabry-Perot interferometer as an edge filter constructed from recycled optical fibers. The proposed interrogator system demonstrated resolutions of 3.6 pm and 2.4 pm in tests involving an optical accelerometer and a carotid pulse waveform sensor, respectively. The experimental setup includes a broadband light source, optical circulators, and a photodetector, with signal acquisition handled by an analog-to-digital converter (ADC) at 5 ksps. The system achieves dynamic monitoring at frequencies up to 5 kHz, and its performance has been compared against commercial spectrometers, showing reliable performance with a maximum root-mean-square error of 0.05. Nevertheless, its performance is limited by the resolution of the ADC and the edge filter's susceptibility to temperature variations, and the technique is demonstrated only for individual FBG sensors rather than arrays.

In Zhang *et al.* (2020), the authors propose an enhanced FBG interrogation system utilizing an edge-filter approach with a tunable Fabry-Perot filter (TFP), specifically designed for high-resolution strain measurements in planetary gearboxes. The system uses the TFP filter to adjust its wavelength in real-time, directly tracking FBG wavelength shifts without reconstructing the entire spectrum. To compensate the drift in the piezoelectric actuator's displacement over time, a feedback mechanism was implemented to ensure stable and accurate performance of the system over time. Moreover, the system was successfully applied to detect strain variations associated with planetary gear faults, and its tunable edge-filter interrogation method allows the simultaneous interrogation of multiple FBGs across a broad wavelength range.

Jeong *et al.* (2017) proposed an FBG interrogator based on a tunable Fabry-Perot filter and a broadband light source, controlled by a LabVIEW program with appropriate signal processing algorithms. The experimental setup comprises an optical circulator, a photodetector module, and cascaded wavelength-multiplexed FBGs. In contrast to previous studies, this work

does not incorporate an edge filter into the interrogation process. Instead, the proposed method determines the Bragg wavelengths of the FBGs by applying a Gaussian curve fitting to the detected sharp peaks. Experimental results showed that the system achieves accuracy comparable to optical spectrum analyzers (OSAs), with reduced standard deviation as the number of samples increases. However, the interrogator's performance is constrained by the signal-to-noise ratio of the FBG reflection spectrum and the FWHM of both the F-P filter and the FBGs. Additionally, the system requires thermal compensation due to the temperature dependence of the F-P filter.

1.2.2 High-speed interrogation techniques

These next works present high-speed interrogation methods designed to handle rapidly changing physical phenomena, making them specifically useful for capturing dynamic events like impacts and monitoring vibrational behavior.

The study presented by Lei *et al.* (2016) explains two types of interrogation techniques for FBG sensors: non-interferometric and interferometric schemes. Non-interferometric methods, employing frequency discriminators, are simple and cost-effective but suffer from limitations such as reduced resolution due to power fluctuations. In contrast, interferometric schemes convert wavelength shifts into phase changes, offering higher resolution but are sensitive to environmental disturbances and have limited speed and dynamic range. To address the need for high-speed, high-resolution interrogation of multiple FBG sensor systems, mode-locked fiber lasers are introduced as pulsed optical sources. These lasers overcome limitations of conventional pulsed lasers, enabling ultrafast and single-shot measurements. The authors demonstrate an ultrahigh-speed multiplexed FBG sensor interrogation system using a home-made broadband mode-locked fiber laser. The system maps wavelength to time through dispersion modules, allowing for accurate interrogation. The performance is evaluated, showing the feasibility of wavelength-to-time mapping and the linear relationship between wavelength shift and time shift. The experimental setup includes an array of five FBGs, demonstrating the system's capability for simultaneous interrogation of multiple sensors utilizing a wavelength-division-multiplexed (WDM) fiber coupler.

Fernández *et al.* (2019) proposed a high-speed and high-resolution FBG interrogation technique that combines crossed Gaussian filters with wavelength-to-time mapping using a highly dispersive medium. This method converts the reflected FBG spectrum into a temporal

waveform, enabling Bragg wavelength determination through amplitude comparison between signals filtered by two Gaussian functions. The proposed system eliminates distortions caused by residual power from FBG sidelobes and extends the linear operational range. Proof-of-concept experiments demonstrated an interrogation speed of 264 MHz and a resolution better than 20 pm. Moreover, the authors state that the method is directly suitable for quasi-distributed sensing networks by enabling the interrogation of multiple FBGs multiplexed through time-division and wavelength-division multiplexing techniques.

Elaskar *et al.* (2021) describes a high-speed FBG interrogator that employs a Sagnac interferometer and phase-generated carrier demodulation. The system has detection bandwidth of 280 kHz and a 1 MS/s sampling rate, and implements a multitone-mixing scheme to reduce distortion. By combining Sagnac interferometers with a lithium-niobate phase modulator, the system achieves fast FBG interrogation with high signal-to-noise ratio enhancement. The system demonstrates real-time Phase Generated Carrier (PGC) demodulation, allowing for the detection of mechanical signals up to 42 kHz with a signal-to-noise ratio of over 65 dB. The interrogator system includes a fiber-optic Sagnac interferometer with high-birefringent sections, a superluminescent diode (SLED) source, a piezoelectric actuator-mounted FBG, and an InGaAs photodiode for signal detection. A portion of the FBG signal is sent to a commercial FBG interrogator for reference. The acquired signal is processed in real-time by a low-cost FPGA system, utilizing multitone mixing to reduce distortion. The system is capable of measuring FBGs within the 1500 - 1600 nm wavelength range and can be multiplexed to measure multiple FBG signals by employing wavelength division filters. However, it limits the sensing FBGs to center wavelengths that match the filters' pass-bands. The measurement results show comparable noise performance between the FPGA system and the commercial interrogator, with the presence of harmonics attributed to the nonlinear response of the piezoelectric actuator.

1.2.3 Innovative interrogation techniques

These next works present FBG interrogation methods based on innovative optical techniques, including vertical-cavity surface-emitting lasers (VCSEL), Mach-Zehnder Interferometers (MZI) and diffraction gratings.

In Dai *et al.* (2022), it was presented a fiber grating interrogation system that utilizes Vertical Cavity Surface Emitting Laser (VCSEL) technology, which offers a low-power and miniaturized solution for temperature and stress monitoring. Traditional FBG interrogation

systems often rely on costly tunable lasers, while systems using broadband light sources have complex structures and higher costs. In contrast, VCSEL-based systems benefit from low power consumption and temperature-free operation. The proposed system achieves a tuning range of 3.5 nm and consumes less than 100 mW of power, meeting the requirements for low power consumption, small size, and low cost. The measurement principle leverages the spectral output characteristics and temperature dependence of a long-wavelength VCSEL module. The system demonstrates accurate temperature monitoring with a mean square error ranging from 1.1 pm to 2.3 pm at different temperatures. It also achieves a scanning wavelength range of approximately 1647.4 nm to 1650.9 nm, meeting the desired 3.5 nm tuning range. Given its limited tuning range, it is rendered impractical for the effective interrogation of a large number of FBGs.

Guo *et al.* (2019) introduced a high-speed FBG interrogation system based on a vertical-cavity surface-emitting laser (VCSEL) array as a low-power-consumption tunable source. The system uses a Fabry-Perot filter to calibrate the dynamic wavelength behavior of individual VCSELs across different sweep rates. By multiplexing five VCSELs, a broadband light source was constructed, enabling a sweeping bandwidth of 10 nm at a scanning rate of 4 kHz. The interrogation process involves a high-speed electronic switch circuit to alternate between VCSELs, ensuring consistent operation during dynamic strain tests. Experimental results during low-velocity impact testing of a composite plate demonstrated a wavelength detection error of 2.7% compared to a high-speed swept laser.

In Marin *et al.* (2017), the authors discuss the experimental demonstration of a miniaturized and cost-effective readout unit for Fiber Bragg Grating sensors, aiming to make them competitive with conventional electronic sensors. The proposed integrated FBG interrogator utilizes an actively monitored unbalanced Mach-Zehnder Interferometer (MZI) with phase-generated carrier demodulation, which enables precise estimation of phase variations – more information about the MZIs can be found in Ji *et al.* (2003). The device incorporates input and output grating couplers for signal coupling and an external arrayed waveguide grating for multiplexing multiple FBGs. Experimental results demonstrate a dynamic strain resolution of 72.3 $n\epsilon/Hz$, showcasing the potential of the photonic integrated circuit on the silicon-on-insulator (SOI) platform for high-density integration and cost-effective interrogation of numerous FBGs. In Marin *et al.* (2019), it is also presented the development of a wavelength division multiplexed FBG sensor interrogator on a silicon-on-insulator SOI platform. The interrogator achieves wavelength division multiplexing of multiple FBGs by combining the MZI and a ar-

rayed waveguide grating (AWG) on the same chip. The SOI platform, with its high-density photonic integrated circuits and compatibility with CMOS processes, offers a cost-effective and high-volume manufacturing solution for FBG readout units. The text describes the device's design and fabrication process, as well as the experimental results that demonstrate its performance compared to a commercial spectrometer-based FBG readout unit.

In Tkachenko *et al.* (2016), the authors present the development of a single-frequency ytterbium fiber laser that sweeps its frequency in a specific wavelength range. This laser is thermally controlled to allow the adjustment of the sweeping range. A prototype of a fiber sensor interrogator based on this laser is developed and tested on a sensor line consisting of 6 FBG sensors. The interrogator employed an optical fiber Mach-Zehnder interferometer for continuous wavelength measurement and specific signal processing techniques based on pulse intensity, and has characteristics such a 1057 to 1076 nm sweeping range, 0.8 nm/sec sweeping rate, exhibiting a considerably slow rate, 55 mW output power and spectral resolution of approximately 5.5 MHz. When comparing the developed device to commercial OSA devices, it demonstrates significantly higher spectral resolution. However, the proposed device's characteristics are not as good in terms of sweeping range and rate as those of tunable lasers with specialized tuning elements. Nonetheless, as mentioned in the article, with further optimization, it would be possible to increase the sweeping range and rate, making the device more suitable for practical sensor systems.

Xiaolin *et al.* (2021) proposed a miniaturized, low-cost, and portable FBG interrogation system designed for remote real-time monitoring. The system uses a superluminescent light-emitting diode (SLED) as a broadband light source, combined with a 4-channel optical switch and a Raspberry Pi as the data processing core. The interrogation method relies on a diffraction grating to spatially separate the reflected spectrum, with a linear image sensor capturing the wavelength shift information. A Gaussian fitting algorithm processes the data to determine the central wavelength with high precision, while a moving average method reduces noise. The system operates over a wavelength range of 1510–1595 nm, achieving an interrogation resolution of 0.1 pm, a precision of 5 pm for the FBG central wavelength, stability within ±1.1 pm, and an interrogation frequency of 4 kHz and supports the interrogation of FBG arrays.

Tosi (2015) proposed an interrogation technique for Fiber Bragg Grating (FBG) and Fabry-Perot Interferometer (FPI) sensors based on the Karhunen-Loeve Transform (KLT) to overcome challenges associated with noisy and coarsely sampled optical fiber sensor data.

By decomposing the spectral information into eigenvalues, the KLT algorithm effectively distinguishes signal components from noise, achieving sub-picometer accuracy in monitoring FBG wavelength shifts and high precision in FPI cavity length detection. Experimental results revealed the algorithm's ability to interrogate individual FBG and FPI sensors with greater accuracy than conventional Fourier-based approaches, even when employing low-resolution spectrometers.

Tosi (2017) provides a comprehensive review and comparison of peak tracking techniques for FBG sensors, outlining their algorithmic implementations and performance under varying conditions. The study categorizes methods into direct estimation, interpolation, correlation, resampling, transforms, and optimization-based approaches, evaluating each technique through simulations based on coupled-mode theory. Performance metrics include accuracy and immunity to noise, revealing trade-offs between computational complexity and signal-to-noise ratio sensitivity. Notable findings highlight that interpolation and correlation-based methods exhibit superior accuracy in high-resolution setups, while transform and optimization methods provide robustness against noise and practical implementation flexibility.

Next, Table 1.1 summarizes the key characteristics of all the FBG interrogation techniques reviewed in this chapter. The comparison highlights the methods' capabilities in terms of multiplexing, resolution, interrogation speed, bandwidth, and notable remarks, providing a comprehensive overview of their contributions and applications. Additionally, the table includes the results obtained in this work for direct comparison with state-of-the-art techniques.

Table 1.1 – Summary of FBG interrogation techniques reviewed.

Article	Interrogation Technique	Multiplexing Capability	Wavelength Resolution	Interrogation Speed	Wavelength Bandwidth	Remarks
Fracarolli (2019)	Edge filter with two-stage digital PI controller	No	-	< 50 kHz	-	Temperature compensation
Pereira (2023)	Ultra-short FBGs as edge filters	Yes	-	-	1520-1560 nm	Cost-effective and temperature compensation
Díaz (2017)	In-line Fabry-Perot interferometer as edge filter	No	2.4 pm	5 kHz	Fabry-Perot[1]	Low cost and dynamic measurements
Zhang (2020)	Tunable Fabry-Perot edge-filter interrogation	Yes	0.1 pm	5 kHz	Fabry-Perot[1]	Specifically designed for planetary gearboxes
Jeong (2017)	Tunable Fabry-Perot filter with Gaussian fitting	Yes	$\sim$ 3 pm	-	Fabry-Perot[1]	Not robust against noise and thermal variation
Lei (2016)	Time-stretch method with mode-locked fiber laser	AWG[2]	-	$\sim$ 200 MHz	84.2 nm range	Very high interrogation speed

Continued on the next page...

[1] The article does not explicitly specify the wavelength bandwidth. However, since the method employs a Fabry-Perot filter or interferometer, it is reasonable to assume that the wavelength bandwidth is comparable to that of a standard commercial Fabry-Perot device, approximately between 1520 and 1570 nm.

[2] The article proposes that multiplexing can be achieved using an Arrayed Waveguide Grating (AWG). However, this method requires a dedicated acquisition system for each wavelength range in operation.

Article	Interrogation Technique	Multiplexing Capability	Wavelength Resolution	Interrogation Speed	Wavelength Bandwidth	Remarks
Fernandez (2019)	Wavelength-to-time mapping with Gaussian filters	AWG[2]	$\sim$ 20 pm	264 MHz	-	Very high interrogation speed
Elaskar (2021)	Sagnac interferometer with FPGA real-time processing	AWG[2]	-	280 kHz	1500-1600 nm	High interrogation speed
Dai (2022)	VCSEL-based low-power interrogation system	No	$\sim$ 2 pm	-	1647.4–1650.9 nm	Low power consumption
Guo (2019)	VCSEL array swept source with high-speed switch	No	$\sim$ 10 pm	20 kHz	1548-1558 nm	Low-power consumption and scalability with additional VCSELs
Marin (2016)	Integrated MZI with active phase demodulation	AWG[2]	-	$<$ 1 kHz	at least 1548-1562 nm	High dynamic resolution
Lobach (2016)	Self-sweeping fiber laser with MZI-based interrogation	Yes	2 pm	0.05 Hz	1058-1076 nm	High spectral resolution
Xiaolin (2021)	Diffraction grating with spectral shifting technique	Yes	0.1 pm	4 kHz	1510–1595 nm	Portable and low-cost remote monitoring
This work	Microcontroller-based twin-grating interrogation using tunable FBG and Fabry-Perot filter	Yes	1.5 pm	500 Hz	1520-1570 nm	Real-time processing; thermal and hysteresis compensation

1.3 Objectives

The objective of this work is to project, develop, and build an interrogation system for a FBG sensor array. This system must feature high excursion capabilities (> 5 nm), allowing for the interrogation of the FBG arrays. It must also be suitable to dynamic measurements (at least 50 Hz acquisiditon rate) with high resolution (at least 5 pm). To accomplish this goal, the project has established the following objectives:

1. Acquire an in-depth comprehension of the interrogation techniques utilized for Fiber Bragg Gratings;
2. Design, construct, and characterize a tunable Bragg Grating filter module employing a piezoelectric actuator;
3. Design and build the optical circuit of the interrogator;
4. Implement algorithms that enable efficient acquisition, filtering, and processing of data from the FBG sensor arrays;
5. Incorporate the capability to perform FBG characterization via deconvolution of the signal obtained from the sensor-grating scan by the filter-grating;
6. Develop and implement thermal compensation techniques;
7. Perform an experimental comparative analysis of the interrogator using FBG-based tunable filter and Fabry-Perot filter;
8. Design and build an electronic circuit for the interrogator;
9. Development of a sensor noise model that includes the main optical and electronic noises;
10. Develop a LabVIEW program for interfacing with the interrogator.
11. Evaluate the performance of the developed interrogator.

1.4 Structure

This work is organized as follows: Chapter 2 provides a theoretical review of FBG sensors, piezoelectric actuators, and the signal processing techiniques employed in this work. In the Chapter 3, the methods used in the study, along with details on implementation and

design are presented. In Chapter 4, an analysis of the experimental results and performance of the developed interrogators are presented. Finally, Chapter 5 presents a critical evaluation of the study's contributions, analyzing its characteristics and limitations, and proposing future improvements. Appendix A presents the source code of the noise analisys and interrogation algorithm simulation developed in Matlab; Appendix B contains the full schematic and PCB layout of the developed interrogator; and Appendix C describes the procedure used to assemble and bond the FBG to the piezoelectric mechanical structure.

2 THEORY REVIEW

This chapter provides an overview of the fundamental theoretical aspects related to the central elements of the present study: Fiber Bragg Gratings (FBGs), interrogation and signal processing techniques and piezoelectric, and Fabry-Perot filters actuators. The discussion is focused on the most relevant subjects for this work, as well as basic concepts necessary for comprehending the study.

2.1 Fundamentals of optical fibers and optoelectronic

Optoelectronics are the study of devices that rely on the interaction between electromagnetic radiation and solids, liquids, or gases. This field has experienced remarkable growth in recent years, with the development of devices such as lasers, light-emitting diodes, photodetectors, liquid crystal displays, and fiber optic communication systems. The latter in particular has revolutionized the telecommunications industry, providing high-speed data transfer over long distances, with minimal signal degradation (Wilson *et al.*, 1984).

The fundamental component of fiber optic communication systems is the optical fiber, which allows for the transmission of light pulses over long distances with minimal signal loss. The propagation of light in a fiber optic cable is governed by complex physical properties, including total internal reflection and the presence of propagating and evanescent waves. These properties, along with the physics of semiconductor materials and optics, form the basis of optoelectronics and are essential for the development of high-performance optoelectronic devices (Buck; Jacobs, 1996).

2.2 FBG sensors

The photosensitivity of optical fibers was discovered in 1978 by Ken Hill and his collaborators at the Canadian Communications Research Center (CRC). With this discovery, it was possible to develop new technologies with significant importance in optical communications and sensing. The creation of permanent gratings in an optical fiber was first made in 1978 by researchers applying intense radiation with an argon ion laser to a germanium-doped optical fiber. The researchers realized that after some time there was an increase in the intensity of the reflected light, which grew until almost all the light was reflected by the fiber. In the spectral

measurements, it was proved that a very narrow band Bragg grating filter had been formed along 1 m of optical fiber length (Hill *et al.*, 1978).

The fiber Bragg grating sensors (FBGs) are devices that use an optical fiber as the sensing element. The basic structure of an FBG (Figure 2.1) consists of a periodic modulation of the refractive index of the optical fiber core, obtained by exposing the core to an intense optical interference pattern. As a result, when a broad-spectrum light source falls on the FBG, a narrow range of wavelengths is reflected, while the rest are transmitted.

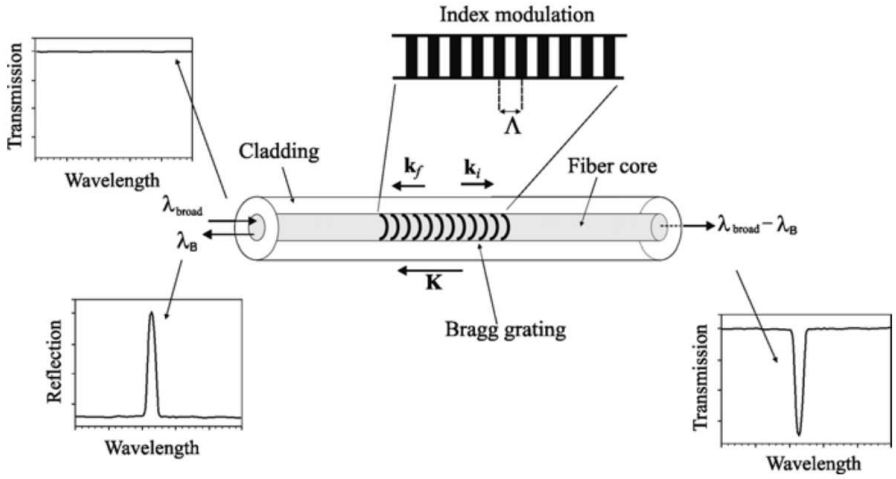

Figure 2.1 – Illustration of a uniform FBG (Othonos *et al.*, 2006).

The three main parameters of a FBG are the Bragg wavelength, the full-width-half maximum (FWHM) bandwidth, and the reflectivity. The Bragg wavelength represents the central wavelength of the incident light that is back-reflected by the grating and is influenced by the effective refractive index of the fiber core. The FWHM bandwidth measures the spectral width of the grating's reflectivity, indicating the range of wavelengths where the reflection intensity is at least half of the maximum value. The reflectivity depends on the amplitude of the induced refractive index perturbation and the grating length, with larger perturbations and longer gratings resulting in increased reflectivity, as shown in the Figure 2.2.

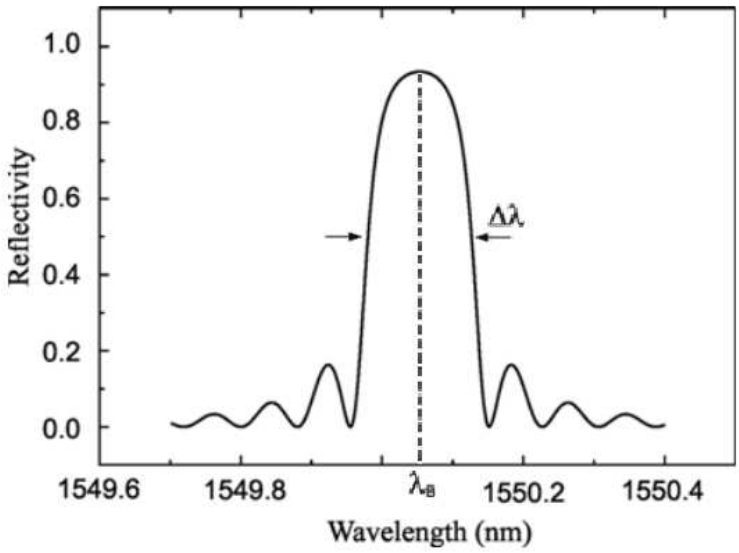

Figure 2.2 – Bragg wavelength (λ_B), FWHM ($\Delta\lambda$) and reflectivity of a FBG (Othonos *et al.*, 2006).

2.2.1 Sensitivity of FBG to temperature and strain

The central wavelength of the reflected light portion, or simply Bragg wavelength, is influenced by the changes in temperature and strain applied to the FBG. Specifically, an increase in temperature and tensile strain causes the Bragg wavelength to shift towards longer wavelengths, while cooling and compressive strain result in a shift towards shorter wavelengths.

Analytically, the Bragg wavelength (λ_B) is given by the Equation (2.1)

$$\lambda_B = 2n_{eff}\Lambda, \tag{2.1}$$

where n_{eff} is the effective refractive index of the fiber core and Λ is the grating period. Both characteristics can be changed by variations in physical parameters such as temperature and strain, thereby changing the value of the Bragg wavelength. Taking advantage of this, it is possible to use FBGs as sensors by detecting the change in the reflected wavelength (Othonos *et al.*, 2006).

It is possible to mathematically determine the result of the variation of (λ_B) in relation to the change in temperature (T) and mechanical stress ($\epsilon = \frac{\Delta L}{L}$), from the partial derivative of Equation (2.1):

$$\Delta\lambda_B = 2\left[\Lambda\frac{\delta n_{eff}}{\delta L} + n_{eff}\frac{\delta\Lambda}{\delta L}\right]\Delta L + 2\left[\Lambda\frac{\delta n_{eff}}{\delta T} + n_{eff}\frac{\delta\Lambda}{\delta T}\right]\Delta T, \tag{2.2}$$

the first term of Equation (2.2) refers to the effect of strain, while the second describes the effect of temperature variation on the optical fiber. Both terms can be rewritten in a way that directly relates to the physical parameters of interest and constant properties of an FBG, resulting in:

$$\frac{\Delta\lambda_B}{\lambda_B} = (1 - p_e)\epsilon + (\alpha_\Lambda + \alpha_n)\Delta T, \tag{2.3}$$

where p_e is the opto-mechanical coefficient on the refractive index of the fiber core, α_Λ is the thermal expansion coefficient of the optical fiber, and α_n is the thermo-optic coefficient on the refractive index of the fiber core.

Thus, given a typical FBG with λ_B = 1550 nm, it has a mechanical sensitivity of approximately 1.2 $pm/\mu m$ and a thermal sensitivity of approximately 13.7 $pm/°C$ (Othonos *et al.*, 2006).

2.2.2 FBG manufacturing techniques

The discovery of FBG occurred through an internal recording technique using ultraviolet radiation. It was observed that the light reflected by the fiber formed an intense interference pattern, resulting in the permanent modulation of the refractive index of the fiber core and characterizing an FBG. However, this technique had drawbacks such as the low level of refractive index alteration and the limitation of wavelength ranges. These disadvantages were overcome with the advent of external recording techniques about ten years later (Hill *et al.*, 1978).

The internal recording method has been replaced by the holographic external interferometric method in 1989, that involves exposing the optical fiber to an interference pattern created by two UV radiation beams incident on the external surface of the fiber. This allows for the creation of gratings with various center wavelengths in different types of germanosilicate fibers (Meltz *et al.*, 1989).

The holographic method enables the formation of FBGs quickly at higher power levels, and there are no length limitations due to saturation effects. The refractive index of the

fiber core can be tailored to achieve the desired transmission or reflection filter characteristic by shaping and tilting the writing pattern through control of the included angle and divergence of the beams. This method also allows for the variation of the modulation period of the refractive index of the fiber core by adjusting the incidence angle between the two beams. (Othonos *et al.*, 2006). This makes it possible to choose the center wavelength of the FBG. Moreover, multiple FBGs with different center wavelengths can be created on the same optical fiber, which has made the production of quasi-distributed FBG sensors easier and more cost-effective (Meltz *et al.*, 1989). This method, however, also have its disadvantages. Firstly, it is susceptible to mechanical vibration, which affects the quality of the interference pattern produced. Additionally, variations in air density between the different optical components can degrade the interference pattern (Othonos *et al.*, 2006).

The phase mask technique, developed by Ken Hill in 1993, is an important innovation in the manufacturing of FBGs. This technique involves creating grooves on a UV-transparent material plate, like high-purity silica, to make a diffraction grating which constitutes the mask of phase, as shown in the Figure 2.3 (Hill *et al.*, 1993).

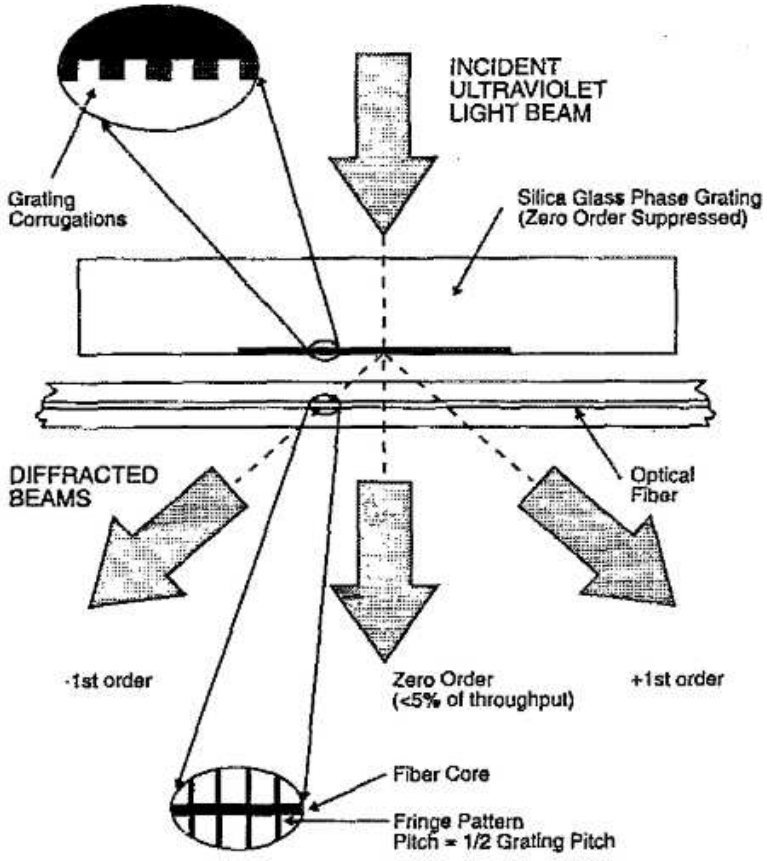

Figure 2.3 – Schematic of photolithographic apparatus for photoimprinting a refractive index Bragg grating in a photosenstive optical fiber waveguide (Hill; Meltz, 1997).

Then, the phase mask is positioned directly onto the exposed optical fiber at the point where the FBG will be inscribed. When the UV radiation beam passes through the mask, it diffracts and produces an interference pattern on the fiber's core, forming the FBG. The distance between the grooves on the phase mask determines the FBG's pitch.

This technique has a significant advantage over other methods because of its precise lithographic corrosion processes, which were already widely used in microelectronics at the time of its invention. These processes enable the accurate determination of the groove spacing and depth of the mask, allowing for the modulation of the refractive index of the fiber in a non-uniform manner by carefully designing the mask's profile. This feature helps create FBGs with highly specific characteristics (Hill *et al.*, 1993).

2.3 FBG interrogation techniques

Interrogation techniques refer to the methods used to extract information from FBGs such as wavelength shift, which can be translated into a physical quantity. The traditional approach to interrogate FBG sensors involves the use of an optical spectra analyzer or a scanning Fabry Perot (F-P) filter, which can be expensive and complex (Wu *et al.*, 2010). In order to address the issues of high cost and complexity associated with this solution, various approaches have been proposed. In this section, we explore some of these techniques that attempt to overcome these disadvantages and provide more efficient and cost-effective ways to obtain information from FBG sensors.

2.3.1 Twin-Grading technique

The twin-grating technique, also known as the tunable filter interrogation technique, is a method of interrogating FBG sensors that relies on the convolution of the reflection profiles of two FBGs. The technique involves partially overlapping the reflection profiles of two FBGs, one being the FBG Sensor and the other FBG acting as a filter, so that the convolution between the two profiles can be measured. The optical power of the convolution is then used for sensor interrogation. In summary, the partial overlap between the two FBGs causes the optical power of the convolution to vary with the physical quantity being measured by the sensor.

The Tunable FBG employed in the twin-grating technique can be utilized in different modes of operation depending on the application requirements. Specifically, it can be

operated either in tracking or scanning mode, which enables the system to interrogate either a single or multiple FBG elements (Othonos *et al.*, 2006).

In tracking mode, the Tunable FBG is locked to the Bragg wavelength of the FBG sensor using a feedback loop, as shown in Figure 2.4. This allows the system to track any changes in the Bragg wavelength caused by external perturbations, such as temperature or strain, and provides a real-time measurement of the physical parameter being monitored. This mode is particularly useful for applications where high accuracy and fast response time are critical, such as in structural health monitoring or industrial process control.

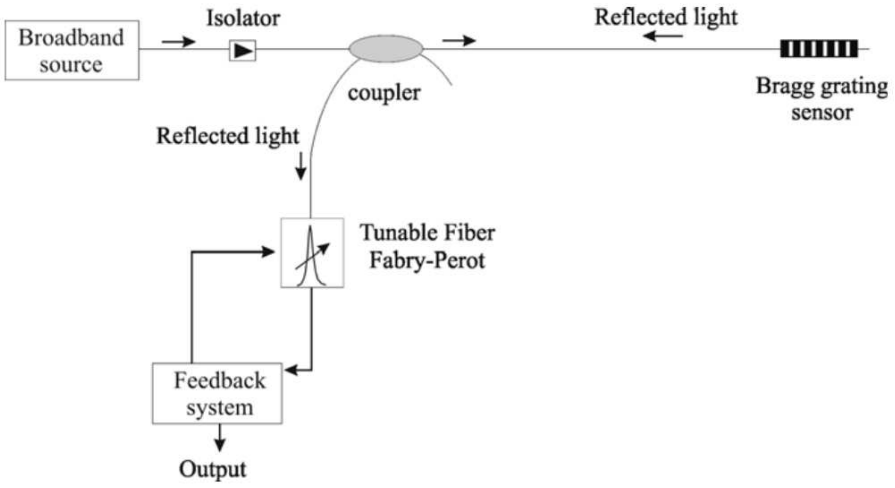

Figure 2.4 – Schematic of tuned filter-based interrogation technique for fibre Bragg grating sensors (Othonos *et al.*, 2006).

In scanning mode, the Tunable FBG is used to address multiple FBG elements along a fiber path, as shown in Figure 2.5. This is achieved by scanning the wavelength of the Tunable FBG over a range that covers the Bragg wavelengths of all the FBGs in the array. The reflected signals from each FBG element are then detected using a photodetector, providing a spectral signature that can be used to determine the physical parameters being measured. This mode is useful for applications where multiple sensors need to be monitored simultaneously.

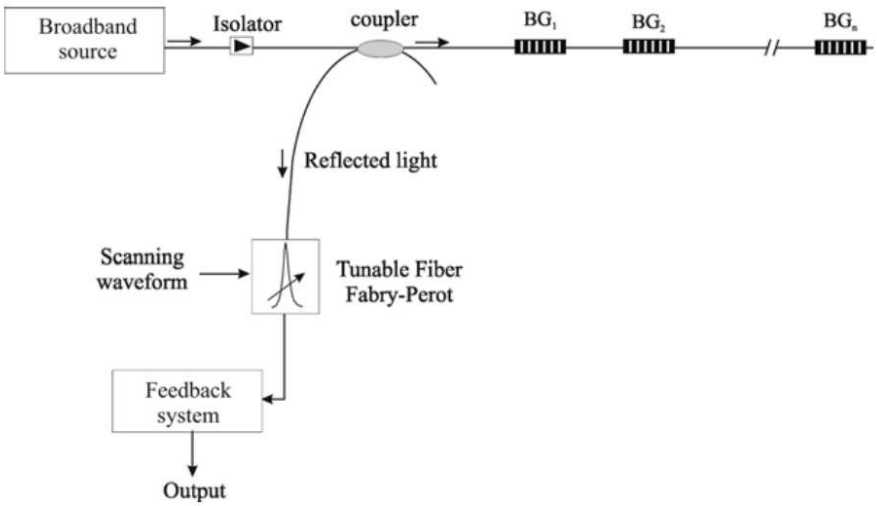

Figure 2.5 – Schematic of multiplexed fibre Bragg grating sensor array with scanning filter (Othonos *et al.*, 2006).

2.4 Actuators employed in the present work

In the following discussion, we explore the actuators utilized in the present work, specifically focusing on piezoelectric actuators and Fabry-Perot filters. We explore the fundamental principles and key considerations associated with these technologies. The aim is to gain a better understanding of how these actuators work and the important factors to take into account when using them.

2.4.1 Multilayer piezoelectric actuators

Piezoelectricity, that basically means pressure electricity, was discovered by Jacques and Pierre Curie in 1880. It describes the ability of certain solid materials to generate electric charge when subjected to mechanical stress. This phenomenon, called the piezoelectric effect, involves the production of electrical charges under pressure. Despite the initial discovery, it took several decades to fully understand the practical applications of piezoelectric materials (Panda; Sahoo, 2015).

Piezoelectric actuators are devices that utilize the inverse piezoelectric effect to convert electrical energy into mechanical motion. When an electric field is applied to a piezoelectric material, it causes the material to deform due to the rearrangement of its internal charges. This deformation leads to a subsequent mechanical displacement or strain. The relationship between the applied electric field and the resulting strain is given by the Equation 2.4

$$\epsilon = d_{ij} * E, \tag{2.4}$$

where d_{ij} represents the piezoelectric coefficient of the material, typically expressed in m/V. The subscripts i and j denote the orientations of the applied electric field E and the measured deformation, respectively.

Multilayer piezoelectric actuators represent an advanced implementation of piezoelectric technology, where multiple thin layers of piezoelectric material are stacked together to enhance performance. This multilayer design allows for larger displacements and higher forces at lower operating voltages compared to single-layer actuators. By increasing the number of layers while maintaining a small individual layer thickness, these actuators achieve higher electric fields within the material without requiring high voltage inputs, making them more efficient and practical for various applications (Yao *et al.*, 1999).

The performance of PZT actuators is influenced by several factors, including hysteresis, a common characteristic of piezoelectric materials, characterized by a non-linear relationship between the applied electric field and the resulting strain. This hysteresis is driven by complex processes intrinsic to the material's microstructure, like domain wall motion and pinning, defect interactions, and polarization switching (Damjanovic, 2006). For applications such as actuators and sensors, where precise control of displacement or force is required, hysteresis in PZT can introduce significant errors, reduce efficiency, and cause the device's behavior to gradually change during prolonged use. While material scientists seek to mitigate this effect through microstructural engineering, device engineers often rely on feedback systems to linearize the response and minimize inaccuracies related to hysteresis.

The Curie temperature is also a critical factor in the behavior of piezoelectric materials. It refers to the temperature at which the crystal structure of a material undergoes a phase transition, causing a loss of its piezoelectric properties. This implies that the process in which the piezoelectric actuator will be utilized must be ensured to operate below this temperature, which varies from material to material. Typically, for PZT ceramics, the Curie temperature ranges between 150 and 350 degrees Celsius. It is crucial to consider this temperature limitation to prevent any loss of piezoelectric properties and ensure the effective functioning of the actuator in practical applications (Heywang *et al.*, 2008).

2.4.2 Tunable Fabry-Perot filters

Fabry-Perot filters are essential components in optical communication networks and sensing applications. These filters operate based on the principle of creating a resonant cavity between two parallel mirrors (Sadot; Boimovich, 1998). When light enters the cavity, it undergoes multiple reflections between the mirrors, leading to constructive interference at certain wavelengths. As a result, the transmission of light through the filter is maximized at these specific wavelengths. By altering the length of the cavity between the fibers, either through heat or piezoelectric techniques, the filter's resonant properties can be adjusted, allowing for tunable filtering capabilities (Milne *et al.*, 2009).

Tunable Fabry-Perot Filters are characterized by several important parameters. Finesse refers to the sharpness of the transmission peaks and is a measure of the filter's ability to resolve closely spaced wavelengths; an interferometer with a higher finesse will produce narrower transmission peaks than one with a lower finesse. The Free Spectral Range (FSR) is the range of wavelengths over which the filter exhibits a single transmission peak before repeating, essentially defining the filter's wavelength span (Thorlabs, 2024). Bandwidth (BW) describes the width of the transmission peak at half its maximum intensity, which affects how much of the spectrum can be passed through at once. Finally, the operational range is the spectrum of wavelengths over which the filter can be tuned and effectively used, dependent on the tuning mechanism employed, such as thermal or piezoelectric adjustments.

2.5 Signal processing techniques

Signal processing techniques encompass a broad range of methods and algorithms that are employed to manipulate and analyze data. By applying these techniques, we can enhance the quality of signals, extract meaningful features, and make informed decisions based on the processed data. They encompass both classical and advanced methods. Classical techniques include filtering, modulation, demodulation, and Fourier analysis, among others. These methods have been extensively used for decades and form the basis of many signal processing applications. On the other hand, advanced techniques such as machine learning, deep learning, and wavelet analysis have emerged with the development of more powerful computing technologies. These techniques enable us to tackle complex signal processing problems, including pattern recognition, anomaly detection, and signal reconstruction.

One of the fundamental goals of signal processing techniques is to extract relevant

information from noisy or distorted signals. Noise can corrupt signals during acquisition, transmission, or storage, and it can significantly affect the accuracy and reliability of the processed data. Signal processing techniques provide us tools to mitigate noise or extract valuable information from noisy signals even without entirely eliminating the noise itself.

2.5.1 Polynomial interpolation

Polynomial interpolation is a signal processing technique that involves fitting a polynomial curve to a set of data points, aiming to estimate an unknown function. It is commonly applied in various fields such as data analysis, function approximation, and image processing. By relating data samples to a polynomial curve, polynomial interpolation allows us to obtain a smooth and continuous representation of the underlying signal. This technique is particularly valuable when dealing with noisy signals, as it can effectively capture and analyze signal patterns even in the presence of noise. In this work, polynomial interpolation serves as a powerful tool to determine the peak or maximum point of a curve, enabling reliable analysis of the signal degraded by noise.

One of the primary approaches to fitting sampled data into a polynomial curve involves minimizing the error between the observed data points and the polynomial model. The general model of this approach can be expressed as:

$$y = \beta_0 + \beta_1 x + \beta_2 x^2 + \beta_3 x^3 + \cdots + \beta_n x^n + \varepsilon. \tag{2.5}$$

In this equation, the coefficients $\beta_0, \beta_1, ..., \beta_n$ are the parameters to be estimated, x represents the independent variable, y is the dependent variable, and ϵ denotes the random error term. The degree of the polynomial, denoted by n, determines the flexibility of the curve and the number of coefficients to estimate (Ostertagová, 2012).

Upon analyzing the polynomial regression equation for a given set of data points, it is possible to express this equation in terms of a design matrix $\mathbf{X}$, a response vector $\mathbf{Y}$, a coefficient vector β, and a vector ε of random errors. Each row of the design matrix $\mathbf{X}$ and the response vector $\mathbf{Y}$ corresponds to the x and y values, respectively, of the i-th data sample. Consequently, the model can be represented as a system of linear equations:

$$\begin{bmatrix} y_1 \\ y_2 \\ y_3 \\ \vdots \\ y_n \end{bmatrix} = \begin{bmatrix} 1 & x_1 & x_1^2 & \dots & x_1^m \\ 1 & x_2 & x_2^2 & \dots & x_2^m \\ 1 & x_3 & x_3^2 & \dots & x_3^m \\ \vdots & \vdots & \vdots & \ddots & \vdots \\ 1 & x_n & x_n^2 & \dots & x_n^m \end{bmatrix} \begin{bmatrix} \beta_0 \\ \beta_1 \\ \beta_2 \\ \vdots \\ \beta_m \end{bmatrix} + \begin{bmatrix} \varepsilon_1 \\ \varepsilon_2 \\ \varepsilon_3 \\ \vdots \\ \varepsilon_n \end{bmatrix}, \tag{2.6}$$

or, using the matrix notation:

$$\mathbf{Y} = \mathbf{X}\beta + \varepsilon. \tag{2.7}$$

The estimation of the optimal coefficients is achieved through a widely used technique known as least squares. This method aims to minimize the squared differences between the observed data points and the corresponding predictions generated by the polynomial model. By reducing these differences, the coefficients that yield the most suitable fit for the polynomial curve can be determined. In practical applications, numerical methods are commonly employed to solve the least squares problem and obtain the optimal coefficients. These numerical techniques employ iterative algorithms that progressively refine the coefficient estimates, converging towards a solution that minimizes the discrepancies between the observed data and the polynomial curve (Ostertagová, 2012).

3 INTERROGATOR DESIGN

In this chapter, we delve into the development of the FBG interrogator. We cover the requirements, both hardware and software design, and provide comprehensive explanations of each component.

FBG sensors offer versatile applications for measuring dynamic deformations, such as mechanical vibrations, as well as indirectly assessing quantities such as AC voltage and current when used in conjunction with piezoelectric or magnetostrictive materials that deform in response to electrical or magnetic fields, respectively. However, ensuring precise and accurate measurements of these variables across the required bandwidth, dynamic range and imunity to environmental changes demands a dedicated interrogator system. Over the past few years, various interrogation techniques, as discussed in Chapter 2, have been developed, each with its unique advantages and disadvantages in terms of performance, size, weight, cost, and other factors.

The interrogator developed in this work was designed based on a variation of the Twin-Grating interrogation technique. In this technique, an FBG is employed as a tunable optical filter, and the center wavelength of the sensing FBG is estimated by identifying the wavelength of the filter FBG at which the convolution of the reflected spectra from both FBGs yields maximum optical power. Our adaptation of this technique employs a tunable filter with a high excursion capacity. With it, a cyclical scan is conducted between a minimum and maximum wavelength, passing through multiple sensor gratings. During each cycle, we can obtain the convolution spectrum between the tunable filter and each one of the sensing grading and, consequently, their current Bragg wavelength. Besides, a second operational mode in our interrogator involves acquiring the complete reflection spectrum of a single FBG, rather than the Bragg wavelength of all FBGs.

Table 3.1 presents all the functional and non-functional requirements that have been considered for the proposed work. Functional requirements embraces all user interactions with the system, including parameter definition and visualization. Non-functional requirements embraces performance, safety, and testability specifications of the system.

In the rest of the chapter, we present the details of the developed hardware and software.

Table 3.1 – Requirements table.

Functional	
1	Monitor the Bragg wavelength of an array of FBGs
2	Obtain the spectrum of a single FBG
3	Allows for the configuration of the scanning frequency
4	Allows for the configuration of the scanning bandwidth
5	USB communication with the control and data acquisition computer
6	Be able to automatically identify the number of sensing FBGs
Non-Functional	
1	Operate in real-time
2	Robustness against noise
3	Robustness against thermal variation
4	Minimum resolution of 5 pm
5	Have a maximum scanning frequency of at least 50 Hz

3.1 Optoelectronic circuit

In this section we focus on the hardware components of the project. Figure 3.1 presents a diagram of the optoelectronic circuit. The light source generates a transmission spectrum broad enough to intersect with the reflection from all the FBGs. This light is incident on the circulator, in which the light entering the Terminal 1 exits at Terminal 2, and the light entering the Terminal 2 exits at Terminal 3. As a result, the light from the source reaches the FBGs, and the resulting reflection spectrum exits the circulator at point 3. At this stage, part of the signal first reflects off a reference FBG, which is maintained under constant thermal conditions. This reference grating is used to correct offsets and temperature-induced drifts, since its Bragg wavelength remains constant. After passing through the reference FBG and the FBG array, the light reaches the splitter. Within this component, 95% of the light is directed to the tunable fiber, while 5% is captured to compensate for instant fluctuations in light power from the light source. In the tunable fiber, the reflection is the result of the convolution between the signals from all sensing FBGs and the reflected signal from the tunable fiber. The light power from this convolution, as well as the 5% of the reflection spectrum, each reaches a photodetector, converting this light power into electrical current. If the system uses a Fabry-Perot

filter instead of a tunable FBG, the fiber connected to the dashed output in the diagram is used instead. Subsequently, in the acquisition circuit, this electrical current is transformed into electrical voltage using transimpedance amplifiers. This resultant voltage is then captured by the microcontroller's analog to digital (A/D) converter. In parallel, the microcontroller controls a PZT actuator responsible for tuning the filter grating using a digital to analog (D/A) converter. Additionally, there is a local operation interface that uses LEDs for status indications and alerts of potential faults. There is also a computer-assisted operation interface utilizing the LabVIEW software, where the acquired information from the interrogator can be displayed.

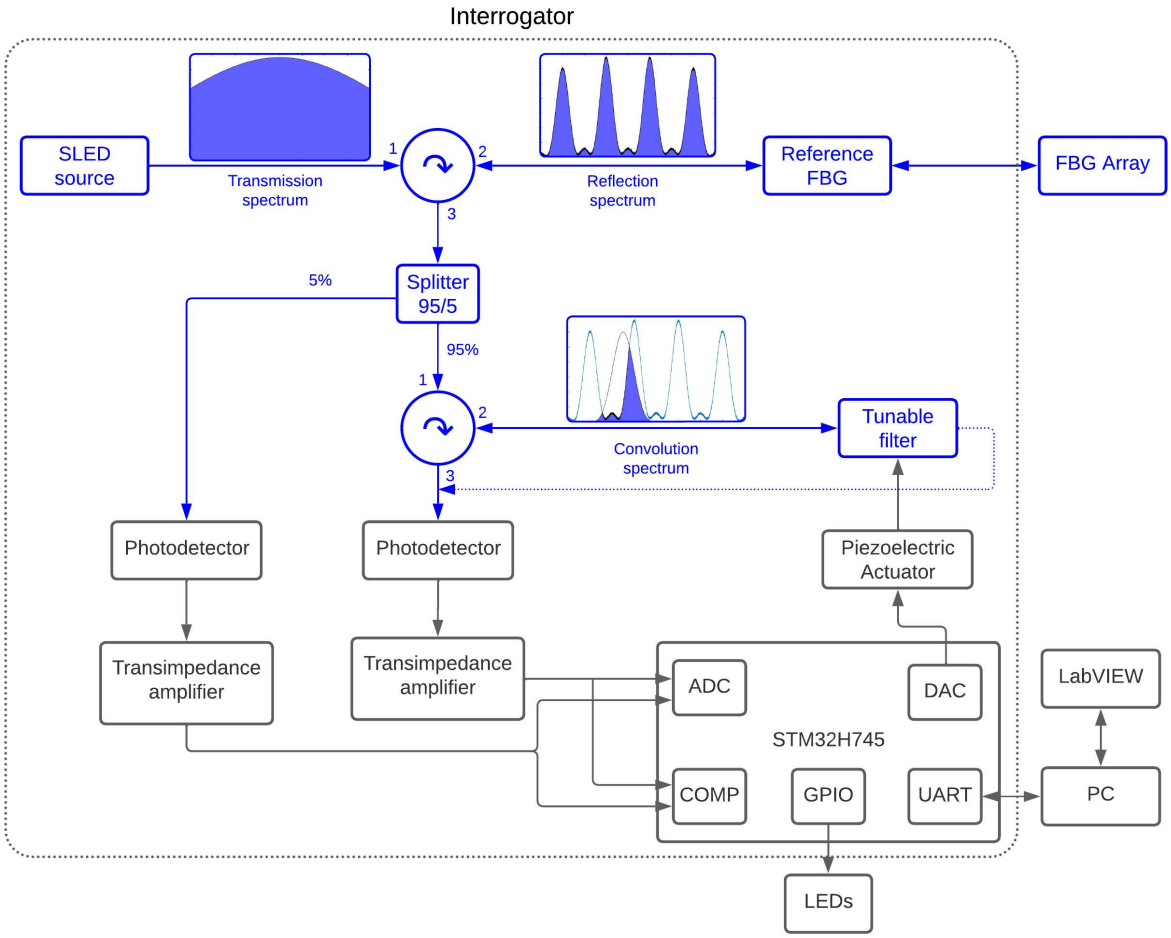

Figure 3.1 – Optoelectronic circuit diagram.

Microcontroller

The microcontroller selected for this project is the STM32H745ZIT6 by STMicroelectronics Inc (STM Microelectronics, 2023), featuring a RISC architecture with two cores and a 32-bit data bus width. The most relevant specifications for this project context are as follows:

- Arm® Cortex®-M7 32-bit core with maximum operating frequency of 480 MHz.
- On-board ST-LINK debugger/programmer with USB re-enumeration capability: mass storage, Virtual COM port, and debug port.
- 2 MB of internal Flash memory.
- 1 MB of internal SRAM memory.
- DMA controllers.
- Timers capable of generating PWM signals.
- 3 A/D converters, with key attributes including:
  - Up to 16-bit resolution.
  - Differential and single-ended analog inputs.
  - Maximum sampling frequency of 3.6 Msps.
  - Typical SINAD (Signal-to-Noise and Distortion) of 75.2 dB.
- 2 12-bit D/A converters with maximum operating frequency of 1 MHz.
- 2 ultra-low-power analog comparators.

SLED source

In the selection of the light source for this project, specific criteria were established, particularly concerning emission spectrum and optical power. The chosen light source, the Inphenix IPSDS1509-0311 (Inphenix, 2023), features characteristics that align with our project's requirements. One of the main prerequisites for this project was a light source with a sufficiently wide emission spectrum to cover the entire reflection spectrum of the FBGs employed in the system, including their maximum wavelength shifts. Table 3.2 presents some of the key specifications that make this particular light source a good choice for our system.

Optical circulator and coupler

As illustrated in the schematic diagram presented in Figure 3.1, the optical circuit also includes two optical circulators and a 2x2 optical coupler with a nominal coupling ratio of 95:5. The 95:5 split is required to obtain the light source's instantaneous power, mitigating

Table 3.2 – SLED main specifications.

Center Wavelength	1550 nm
Optical Bandwidth	90 nm
Optical Output Power	8 mW
ASE Ripple	Up to 0.5 dB
Optical Power Stability (8hr)	±0.1 dB

issues related to power fluctuations. Based on the experimental measurements, it was observed that the total power loss from the light source to the main photodetector is approximately -3 dB.

Fabry-Perot filter

The selected Fabry-Perot filter, Luna Innovations's FFP-TF-1520-1570-7.5G-2000-3-065 (Luna, 2020), have features that align with our project's requirements. A particular one is the maximum tuning range of 50 nm, providing a broad scanning capacity that accommodates the entire reflection spectrum of the Fiber Bragg Gratings (FBGs) used in the system, including their maximum wavelength shifts. Other relevant characteristics are presented in Table 3.3.

Table 3.3 – Fabry-Perot filter specifications.

Parameter	**Value**
Wavelength Range Min	1520 nm
Wavelength Range Max	1570 nm
Free Spectral Range (FSR)	120 nm
Finesse	2000
FWHM	60 pm
Insertion loss	< 3 dB
Maximum input Power	15 mW
Connector	FC/APC
Capacitance	< 3 µF
Tuning voltage	12 V/FSR
Tuning voltage maximum	70 V
Tuning rate	2500 Hz/FSR

FBGs

In this work, commercial FBGs were used for both the tunable grating and the FBG array employed for the testing and validation of the system. These FBGs are characterized by a Full Width at Half Maximum (FWHM) of 0.25 nm and a maximum reflectivity of -3 dB.

Estimation of expected optical acquisition power

This section presents the calculations performed to estimate the optical power reaching the acquisition circuit, considering two scenarios: when the Fiber Bragg Grating (FBG) is used as the tunable filter of the system and when the Fabry-Perot filter is used. The expected power is obtained based on the source characteristics, FBG and Fabry-Perot Filter properties and optical component losses.

The calculations are based on the following parameters:

- **Source Power:** $P_{Source} = 8\,\text{mW}$
- **Source Spectral Width (FWHM):** $\Delta\lambda_{Source} = 90\,\text{nm}$
- **FBG Spectral Width (FWHM):** $\Delta\lambda_{FBG} = 0.25\,\text{nm}$
- **FBG Reflectivity:** $R_{FBG} = -3\,\text{dB}\ (\approx 70\%)$
- **Optical Component Losses:** $Loss_{Total} = -3\,\text{dB}\ (\approx 70\%)$
- **Fabry-Perot Spectral Width (FWHM):** $\Delta\lambda_{FP} = 60\,\text{pm}$
- **Fabry-Perot Insertion Loss:** $Loss_{FP} = -3\,\text{dB}\ (\approx 70\%)$

The amount of optical power directed from the source into each sensing FBG was considered to be proportional to the spectral width of the FBG relative to the spectral width of the source. Additionally, the reflectivity of the FBG was also taken into account:

$$P_{FBG} = P_{Source} \cdot \frac{\Delta\lambda_{FBG}}{\Delta\lambda_{Source}} \cdot R_{FBG} \tag{3.1}$$

$$P_{FBG} = 8\,\text{mW} \cdot \frac{0.25\,\text{nm}}{90\,\text{nm}} \cdot 0.7 \tag{3.2}$$

$$P_{FBG} = 15.55\,\mu\text{W} \tag{3.3}$$

Considering the losses in the optical components, the final expected power for each sensing FBG becomes

$$P_{post-loss} = Loss_{Total} \cdot P_{FBG}, \tag{3.4}$$

$$P_{post-loss} = 0.7 \cdot 15.55\,\mu\text{W}, \tag{3.5}$$

$$P_{post-loss} = 10.88\,\mu\text{W}. \tag{3.6}$$

When the FBG is used as a tunable filter, the expected output power is calculated by applying the FBG reflectivity once more

$$P_{FBG-Tunable} = R_{FBG} \cdot P_{post-loss}, \tag{3.7}$$

$$P_{FBG-Tunable} = 0.7 \cdot 10.88\,\mu\text{W}, \tag{3.8}$$

$$P_{FBG-Tunable} = 7.62\,\mu\text{W}. \tag{3.9}$$

For the Fabry-Perot filter, the expected power is calculated considering its spectral width and insertion loss

$$P_{FP} = P_{post-loss} \cdot \frac{\Delta\lambda_{FP}}{\Delta\lambda_{FBG}} \cdot Loss_{FP}, \tag{3.10}$$

$$P_{FP} = 10.88\,\mu\text{W} \cdot \frac{60\,\text{pm}}{250\,\text{pm}} \cdot 0.7, \tag{3.11}$$

$$P_{FP} = 1.83\,\mu\text{W}. \tag{3.12}$$

The final results for the expected optical power are as follows:

- **FBG as Tunable Filter:** $P_{FBG-Tunable} = 7.62\,\mu\text{W}$,
- **Fabry-Perot Filter:** $P_{FP} = 1.83\,\mu\text{W}$.

Acquisition circuit

The typical circuit for a transimpedance amplifier consists of a photodiode, a transimpedance amplifier, and an analog-to-digital (A/D) converter, which, in this project, is integrated into the microcontroller. The photodiode converts the optical signal from the interrogator's optical circuit into an electrical current, which is then further transformed into voltage by the transimpedance amplifier. Then, the processed voltage signal is directed to the microcontroller's ADC input.

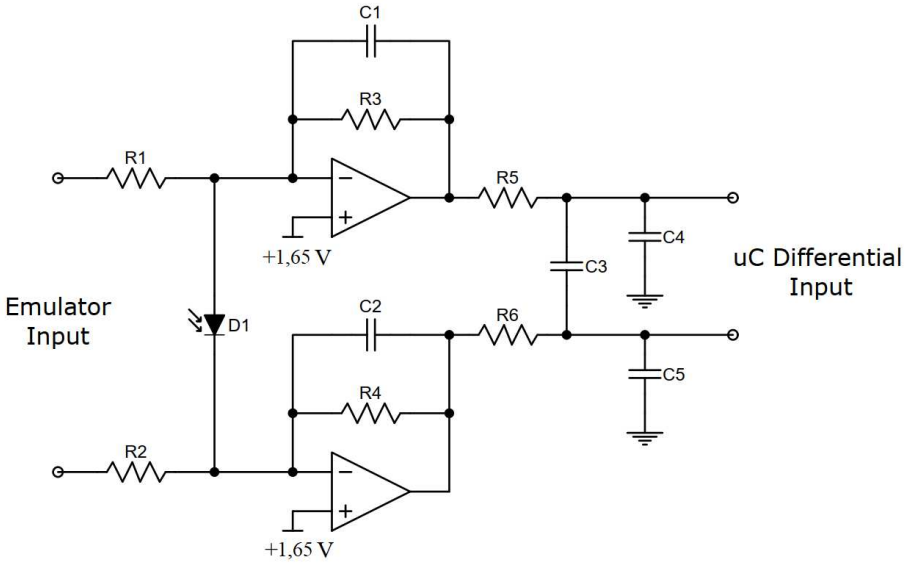

Figure 3.2 – Acquisition circuit.

In order to improve interference immunity, the acquisition circuit shown in Figure 3.2 employs two transimpedance amplifiers, with each output directed to one of the microcontroller's A/D converter terminals, configured with the differential input settings. In this design, the upper and lower branches are identical, with components such as R1 equal to R2, C1 equal to C2, and so on. This symmetry results in the voltage generated in the upper branch being of equal magnitude to that produced in the lower branch but with opposite polarity. The STM32H745 A/D converter's differential configuration requires that the input voltage at its terminals be centered at its reference voltage, which in our configuration is 1.65 V. To achieve this, the positive terminals of both Op-Amps are connected to a 1.65 V reference voltage.

The circuit also features a differential input, intended for connection to an emulation of the optical signal. Resistors R1 and R2 are required to ensure that the emulated voltage matches the voltage generated by the optical circuit. The emulation system is executed using the microcontroller's digital-to-analog (D/A) converters and will be further elaborated in the Section 3.3.1.

The components were selected with the objective of minimizing the signal-to-noise ratio. Also, the Op-Amps are expected to exhibit bias current in the order of a few picoamperes, low voltage and current noise and a high gain-bandwidth product, making the requirements for this component very restrictive. Since no single device presents all of these characteristics, it was necessary to select a balanced one, the OPA2356 (Texas Instruments, 2001). In Table 3.4, we provide a detailed overview of the key parameters of the Op-Amp utilized in the tran-

simpedance amplifier implementation within the acquisition circuit. The utilized photodiode has a responsivity of 0.9 A/W. The resistor values were selected to ensure that the gain of the amplifiers was both necessary and sufficient to amplify the maximum current generated by the photodiode, based on the optical power previously calculated in this section, to a differential voltage of up to 3.3 V. This maximum current was determined considering the optical convolution power equal to the total reflected power of an FBG with a full width at half maximum (FWHM) of 0.25 nm. The capacitor values were chosen such that the cutoff frequency of the low-pass filter formed by each resistor and capacitor pair matched the Nyquist frequency of the system, which is half the sampling rate of the A/D converter. These values can be found in Table 3.5.

Table 3.4 – OPA2356 parameters

Parameter	**Value**
Gain-Bandwidth Product	200 MHz
Bias Current	3 pA
Slew Rate	360 V/µs
Common-Mode Input Voltage	-0.1 V to 3.5 V
Supply Voltage (single-supply)	2.5 - 5.5 V
Voltage Noise Spectral Density (at 1 MHz)	5.8 nV/√Hz
Current Noise Spectral Density (at 1 MHz)	50 fA/√Hz

In this configuration, the transimpedance circuit achieves a transimpedance gain of 100 kV/A and a bandwidth of 1 MHz.

Actuator and driver

The tunable FBG reflection shifts are achieved through controlled application of mechanical stress to the FBG, using a multilayer piezoelectric actuator (PZT). In this project, the AN0X/8500b actuator, manufactured by EPCOS, is employed, and its datasheet is provided in Figure A.1 in Annex A. This device requires a pre-load of 15-20 MPa to prevent damage to the actuator caused by tensile loading. The driver used to control the PZT actuator is the MX200 V10 (PiezoDrive, 2021), and its main relevant specifications for this project are presented in Table 3.6. The tunable FBG sweep is driven by a sinusoidal control signal, which mitigates

Table 3.5 – Components values

Component	Value
R1	100 kΩ
R2	100 kΩ
R3	100 kΩ
R4	100 kΩ
R5	1.5 kΩ
R6	1.5 kΩ
C1	1.5 pF
C2	1.5 pF
C3	27 pF
C4	54 pF
C5	54 pF

signal distortions caused by the bandwidth limitations of the electronic circuitry and enables higher sweep rates by ensuring smoother transitions throughout the scan.

Table 3.6 – MX200 PiezoDrive parameters

Parameter	Value
Power Supply	24 V
Output Voltage Range	±100 V
Peak Output Current	1 A
Power Bandwidth (180 Vp-p)	106 kHz
Signal Bandwidth (100nF Load)	200 kHz
Slew Rate	60 V/us
Gain	20 V/V
Max. Output Noise	100 uV RMS

3.1.1 Noise analyzes

In every measurement system, there are always random variations in the measurement of the variable of interest, which are characterized as noise. Regarding its origin, elec-

tronic noise can be either external, caused by interference, or internal, inherent to the electronic circuit and its components. Noise cannot be entirely eliminated, but there are techniques and precautions that can be taken to ensure that the noise level falls within an acceptable range for the specific project's application. The noise analysis of the acquisition and conditioning electronics of optical signals is fundamental for a optimized design. It enables us to anticipate and control the accuracy of the acquired signal, the level of certainty in the output signal, as well as identify components that may be predominant in the sensor's noise, opening opportunities for optimization. External noise can be largely reduced through proper grounding and shielding of the acquisition and conditioning electronics. In the proposed interrogator, the current generated from the photodiodes are amplified by a differential transimpedance amplifier and measured by the microcontroller's A/D converter configured with differential input. This approach is useful to provide greater immunity to external interference.

In this project, the primary sources of noise are optical, compose mainly by shot noise and excess photon noise, as well as the operational amplifiers, feedback resistors and the A/D converter.

The shot noise consists of random fluctuations in photocurrent, mainly due to the discrete nature of photons and electrons. It corresponds to the standard deviation of the photon arrival rate at the photodetector. Shot noise is proportional to the square root of the optical power. The spectral density of shot noise is represented by

$$N_{sn} = 2\,e\,i_{cc} \quad (\mathrm{A}^2/\mathrm{Hz}), \tag{3.13}$$

where e is the elementary charge ($e \approx 1,6 \cdot 10^{-19}\ C$) and i_{cc} is the photodetector current.

Excess photon noise, also referred to as quantum noise or photon noise, is a fundamental source of noise caused by random collisions among all frequency components of a wide-spectrum signal. The spectral density of photon noise is represented by

$$N_{epn} = \frac{i_{cc}^2}{\Delta v_e} \quad (\mathrm{A}^2/\mathrm{Hz}), \tag{3.14}$$

where Δv_e represents the effective spectral bandwidth of the light source in the frequency domain.

It is important to note that shot noise is proportional to the square root of the light power, which means its effect can be reduced by increasing the light power, as the generated signal scales proportionally. However, excess photon noise cannot be similarly mitigated since it is directly proportional to the light power.

With regard to electronic components, the primary source of noise is associated with resistor's thermal noise. Thermal noise results from the agitation of electrons and is directly proportional to temperature. The power spectral density of thermal noise is

$$N_r = 4KTR \quad (\mathrm{V}^2/\mathrm{Hz}), \tag{3.15}$$

where K is the Boltzmann constant, T is the temperature in Kelvin, and R is the resistance value.

In addition, we also have the voltage and current noises from the transimpedance amplifier, as well as the input noises of the A/D converter. These values depend on the design features of these devices and are typically specified in their datasheets. There is also the ADC quantization noise resulting of errors caused by the discretization of the analog signal and is described by

$$AD_Q = \frac{\frac{V_{ref}}{2^N}}{\sqrt{12}} \quad (\mathrm{V}_{\mathrm{RMS}}), \tag{3.16}$$

where V_{ref} is the full-scale voltage range of the ADC, and N is the number of bits of the A/D converter.

The total noise should be calculated by taking the root-sum-square of all the noises that affect the system. Some of them are current noises, which are then converted to voltage noise through the transimpedance amplifiers by multiplying them by their gain. The input and quantization noises of the A/D converter must be converted to spectral density by squaring and dividing by the acquisition frequency of the system. Thus, the total spectral noise density of the system can be expressed as

$$N_t = A^2 \left(N_{sn} + N_{epn} + N_{Ai}\right) + N_{Av} + \frac{AD_i}{\Delta f} + \frac{AD_Q}{\Delta f} + \sum_{k=1}^{n} N_{r_k} \quad (\mathrm{V}^2/\mathrm{Hz}), \tag{3.17}$$

where A is the gain of the amplifiers, N_{Ai} is the current noise of the amplifiers, N_{Av} is the voltage noise of the amplifiers, AD_i is the input noise of the A/D converter, and Δf is the interrogation acquisition frequency.

Considering the maximum power emitted by the SLED source and the responsivity of the diode used in the circuit, it is possible to easily calculate the values of shot noise and excess photon noise using equations 3.13 and 3.14.

$$N_{sn} = 5.127 \cdot 10^{-23}\ \mathrm{A}^2/\mathrm{Hz}, \quad N_{epn} = 2.277 \cdot 10^{-21}\ \mathrm{A}^2/\mathrm{Hz}. \tag{3.18}$$

With respect to the noise related to the OP-AMP, these are detailed in Table 3.4. It is only necessary to square the values found to standardize with the unit used in all equations.

$$N_{Ai} = 100 \cdot 10^{-30}\ \mathrm{A}^2/\mathrm{Hz}, \quad N_{Av} = 33.64 \cdot 10^{-18}\ \mathrm{V}^2/\mathrm{Hz}. \tag{3.19}$$

The quantization and input noises of the A/D converter were experimentally obtained by short-circuiting the module's differential inputs and logging the acquired value for 5 minutes. Subsequently, the RMS value was calculated, and from it, the power spectral density of the noise was determined. Then, this obtained value can be compared to the quantization noise derived from Equation 3.16, allowing us to determine which of these two noise sources is dominant.

$$\frac{AD_i}{\Delta f} + \frac{AD_Q}{\Delta f} = 1.674 \cdot 10^{-16}\ \mathrm{V}^2/\mathrm{Hz}. \tag{3.20}$$

$$AD_Q = 7.268 \cdot 10^{-6}\ \mathrm{V_{RMS}} \quad then, \quad \frac{AD_Q}{\Delta f} = 1.056 \cdot 10^{-16}\ \mathrm{V}^2/\mathrm{Hz}. \tag{3.21}$$

In this way, we can verify that the ADC quantization noise and the input noise are equally dominant in terms of order of magnitude.

Finally, the thermal noise was calculated based on the values of resistors R3 and R4 from Table 3.5. The thermal noise for resistors R5 and R6 is also calculated in the same manner. However, their values will be significantly lower compared to R3 and R4, as they have much higher resistance values.

$$\sum_{k=1}^{n} N_{r_k} = 2.652 \cdot 10^{-15}\ \mathrm{V}^2/\mathrm{Hz}. \tag{3.22}$$

With all these calculated values, it is possible to compute the total noise power spectral density and, consequently, the RMS value of the noise in the bandwidth of 1 MHz.

$$Nt = 2.334 \cdot 10^{-13}\ \mathrm{V}^2/\mathrm{Hz}. \quad Nt = 0.483\ \mathrm{mV\ RMS\ (1\ MHz\ bandwidth)} \tag{3.23}$$

3.1.2 Printed circuit board (PCB)

The electronic schematic and PCB layout of the interrogator system were developed using Altium Designer and are presented in Appendix B. The appendix includes the full schematic diagrams, as well as the top and bottom layers of the PCB layout, organized by functional blocks, providing implementation details for all the functionalities described throughout the chapter.

3.2 Mechanical structure

To enable controlled strain application on both the sensing and filter FBGs and thus shift their Bragg wavelengths, a mechanical mechanism was developed incorporating a piezoelectric actuator and a pre-loading spring. The optical fiber is fixed onto this mechanism in such a way that the FBG region is precisely positioned between the two surfaces that are displaced by the action of the piezo element. This configuration ensures that the induced deformation occurs directly on the grating region. The developed tunable filter actuator, based on a multilayer PZT stack and a Fiber Bragg Grating (FBG), is presented in Figure 3.3.

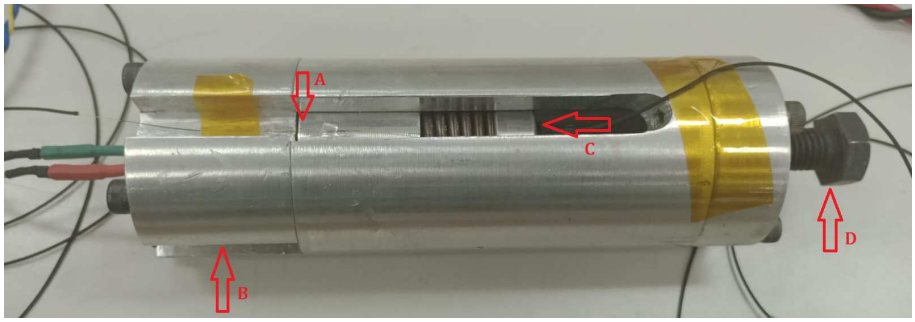

Figure 3.3 – FBG-PZT-based tunable filter module: (A) filter FBG, (B) multilayer piezoelectric actuator, (C) pre-load mechanism, (D) screw used to adjust the pre-load.

Further implementation details regarding the mechanical assembly process are provided in Appendix C. This includes a step-by-step description of how the exact position of the FBG along the fiber was identified and aligned with the mechanical structure, as well as the procedures and precautions taken to bond the fiber to the mechanism.

3.2.1 Estimation of Bragg wavelength range

To evaluate the wavelength excursion capacity of the proposed actuator, it is necessary to consider the mechanical strain induced on the fiber and its relationship with the Bragg wavelength shift. The sensitivity of an FBG to axial strain is approximately $1.2\ \text{pm}/\mu\varepsilon$. According to typical datasheets, optical fibers can withstand mechanical strain in the range of $5,000$ to $15,000\ \mu\varepsilon$, corresponding to a maximum Bragg wavelength excursion of approximately 6 nm.

Given a standard optical fiber diameter of $125\ \mu$m, its cross-sectional area is $A = 1.227 \times 10^{-8}\ \text{m}^2$, and the Young's modulus of silica is around 70 GPa. The maximum axial force F_{max} required to achieve this level of strain is calculated using:

$$F = E \cdot \varepsilon \cdot A \tag{3.24}$$

$$F_{\text{max}} = 70 \times 10^{9}\ \text{Pa} \cdot 5 \times 10^{-3} \cdot 1.227 \times 10^{-8}\ \text{m}^2 \approx 0.44\ \text{N} \tag{3.25}$$

The actuator used in this work is a piezoelectric transducer with a maximum free displacement of $40\ \mu$m under dynamic conditions (pre-load of 800 N at 160 V, $25°$C). Since the FBG is bonded over a 10 mm fiber segment, the induced strain is given by:

$$\varepsilon = \frac{\Delta L}{L} = \frac{40 \times 10^{-6}}{10 \times 10^{-3}} = 4 \times 10^{-3} = 4,000\ \mu\varepsilon \tag{3.26}$$

$$\Delta\lambda_B = \varepsilon \cdot 1.2\ \frac{\text{pm}}{\mu\varepsilon} = 4,800\ \text{pm} = 4.8\ \text{nm} \tag{3.27}$$

Therefore, the maximum Bragg wavelength tuning range of the developed actuator is estimated to be 4.8 nm, limited primarily by the displacement capacity of the piezoelectric element and the length of the fiber region being stretched.

Finally, with the use of a 12-bit digital-to-analog converter to control the actuator, the voltage resolution results in:

$$R = \frac{4,800 \text{ pm}}{2^{12}} \approx 1.17 \text{ pm} \tag{3.28}$$

This value corresponds to the minimum wavelength shift that can be applied to the tunable FBG through the actuator control.

3.3 Interrogator firmware

The proposed embedded system was designed to acquire the optical signals (convolution signals from the FBGs and the reference signal from the light source), control the tunnable filter, process the acquired signal and estimate the Bragg wavelength of every FBG, as well transmit the data in real time through UART/USB communication. Realizing these functions in real-time and at high frequencies presents significant challenges. The system must operate at precise acquisition rates for the A/D conversions (2 MHz) and D/A updates (1 MHz). Working at such high acquisition speeds, traditional polling methods become impractical. The use of polling can lead to data losses, delays, and difficulties in multiplexing tasks. Even with a high-speed processor, employing many command instructions might not be fast enough when trying to manage multiple resources and execute different tasks in real-time at high frequencies. These challenges demand a optimized approach that combines precise timing and synchronization to ensure the system can effectively handle the demanding requirements of signal acquisition. Due to these constraints, FPGAs are commonly employed for implementing high-performance FBG interrogators. However, development on FPGAs is inherently more complex than on microcontrollers, as it typically involves hardware description languages and low-level design practices. Nevertheless, by leveraging specific hardware features available in certain microcontrollers—such as high-speed ADCs, DMA controllers, and hardware timers—it is possible to implement FBG interrogation systems in a more efficient and accessible manner, without significantly compromising performance. Much of the system's functionality was integrated directly into the microcontroller's hardware, minimizing the use of polling and even interruptions. This was achieved through automatic synchronization of modules, using Direct Memory Access (DMA) for efficient data transfer.

Before we delve into the embedded software of the system itself, it's crucial to understand how the microcontroller's modules were configured to operate at the hardware level. In the Figure 3.4, we present a diagram to aid in comprehending each module and its interactions, followed by a more detailed explanation of the functionality of each module.

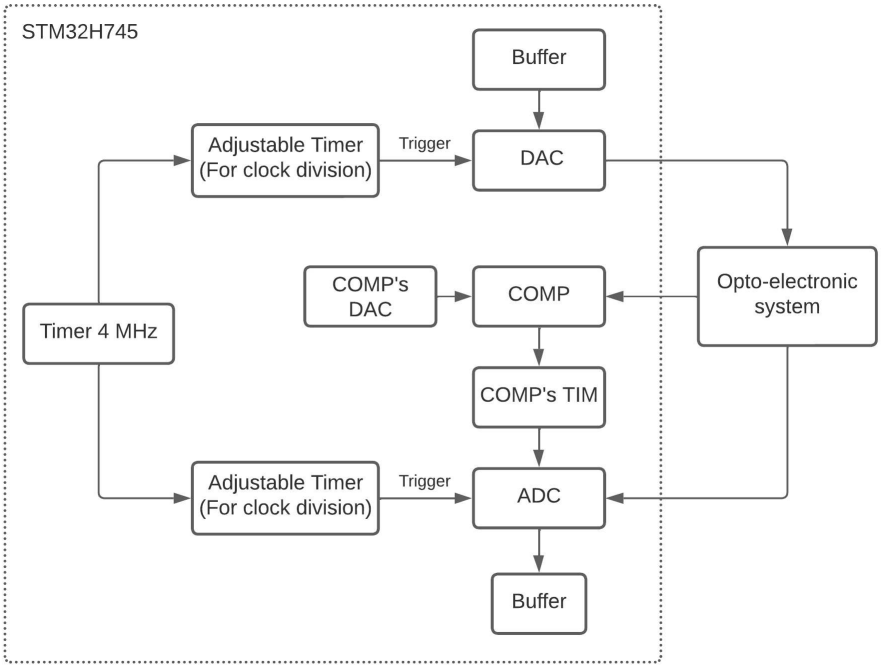

Figure 3.4 – Microcontroller's modules diagram.

DAC (Digital-to-Analog Converter): The microcontroller's DAC is responsible for transmitting the signal to the tunable filter. The signal to be written is sent through DMA from a circular static buffer that contains one period of a sinusoidal signal, and the conversion triggers are set by a timer with an adjustable prescaler to control the system's scanning rate. This approach, despite requiring more memory to store the modulation signal, does not demand any processing power, neither to generate the samples of the sinusoidal signal nor to send it to the DAC.

ADC (Analog-to-Digital Converter): The microcontroller's ADC records the convolution power received from the optoelectronic circuit into a buffer of constant size using DMA. The conversion triggers for the ADC is also be driven by the same timer used by the DAC with another adjustable prescaler to control the system's aquisition rate. The ADC module is configured to perform oversampling on the input signal, reducing high-frequency noise and improving signal quality. Although this decreases the number of points for analysis, tests indicated that increasing the number of points resulted in little gain in resolution, while significantly increasing processing time.

COMP (Comparator): The microcontroller's analog comparator identify when the convolution spectrum exceeds a certain threshold signal, generated by another DAC represented as *COMP's DAC* in the diagram. It detect the intersections between the spectrum reflected by

the FBGs and the tunable filter. It also makes use of an auxiliary TIM module to implement a digital edge filter, ensuring that an edge is only registered when the comparator output remains stable for at least 32 clock cycles. This prevents false edge detections caused by noise or oscillations near the threshold, which would otherwise introduce significant errors in the wavelength calculation. When the comparator detects both a rising and falling edge on its input, it captures the current DMA address where either the ADC is writing to or the DAC is reading from. This process helps determine the buffer positions that represent the start and end of an intersection.

Tunable filter hysteresis compensation

To correlate each DAC output value with its corresponding Bragg wavelength of the tunable grating, or the Fabry-Perot filter's center wavelength, a lookup table approach was adopted. This table maps each discrete point of the sinusoidal excitation signal to its associated wavelength, allowing the system to estimate the tunable filter's wavelength corresponding to any DMA address provided by the comparator in reference to the DAC output.

For the developed FBG-PZT-based actuator, the values of this lookup table were obtained experimentally by driving the tunable FBG with the same sinusoidal waveform used in the interrogator and simultaneously acquiring the reflected wavelength values through an commercial interrogator (Luna SI-155). Subsequently, the average of several scanning periods is computed in order to obtain a more robust and accurate lookup table.

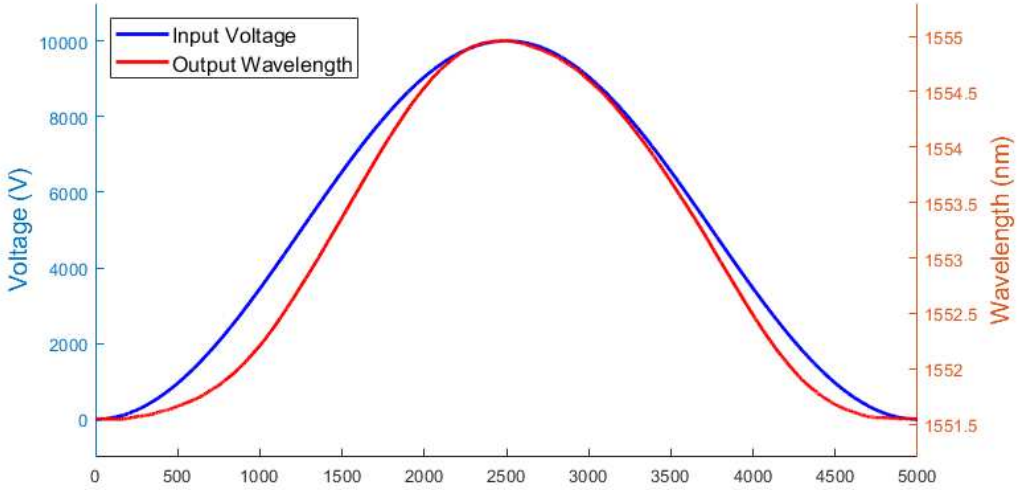

Figure 3.5 – Comparison between the input sine wave applied to the tunable grating and the actual wavelength response.

As shown in Figure 3.5, the actual response of the filter exhibits hysteresis, causing

an asymmetry between the rising and falling slopes of the wavelength modulation. This nonlinea behavior can be attributed to factors such as the mechanical coupling mechanism and intrinsic nonlinearities of the piezoelectric actuator driving the FBG.

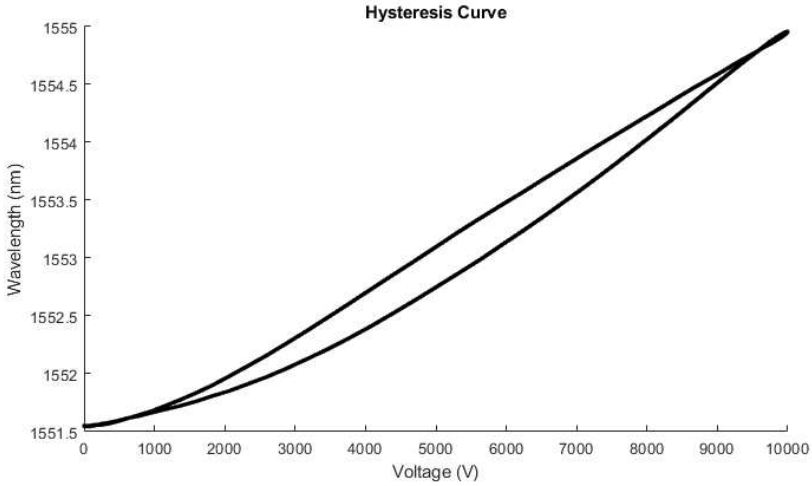

Figure 3.6 – Hysteresis Curve - Bragg Wavelength x Applied Voltage.

Figure 3.6 presents the complete hysteresis cycle obtained experimentally, evidencing how the Bragg wavelength depends not only on the instantaneous input voltage but also on the scan direction. Despite this behavior, by using a lookup table directly derived from real measurements, the system inherently compensates for these effects, providing more accurate wavelength estimations during both rising and falling edges of the modulation.

3.3.1 Embedded software

In this section, flowcharts related to the main routines executed by the FBG interrogator's firmware are presented. These include the callback of the TIM interrupt corresponding to the COMP module, which handles the start and end of FBGs convolution signal acquisiton; and the Bragg wavelength calculation function, which takes the vector containing the convolution signal points of an FBG and returns the current Bragg wavelength of that FBG.

TIM-COMP callback

The TIM-COMP callback is responsible for identifying the intersection between the power spectrum of each sensing FBG and the tunable filter, enabling the calculation of their respective Bragg wavelengths. Its flowchart is represented in Figure 3.7. At the beginning of each comparator interruption, the algorithm first checks whether it corresponds to a rising or

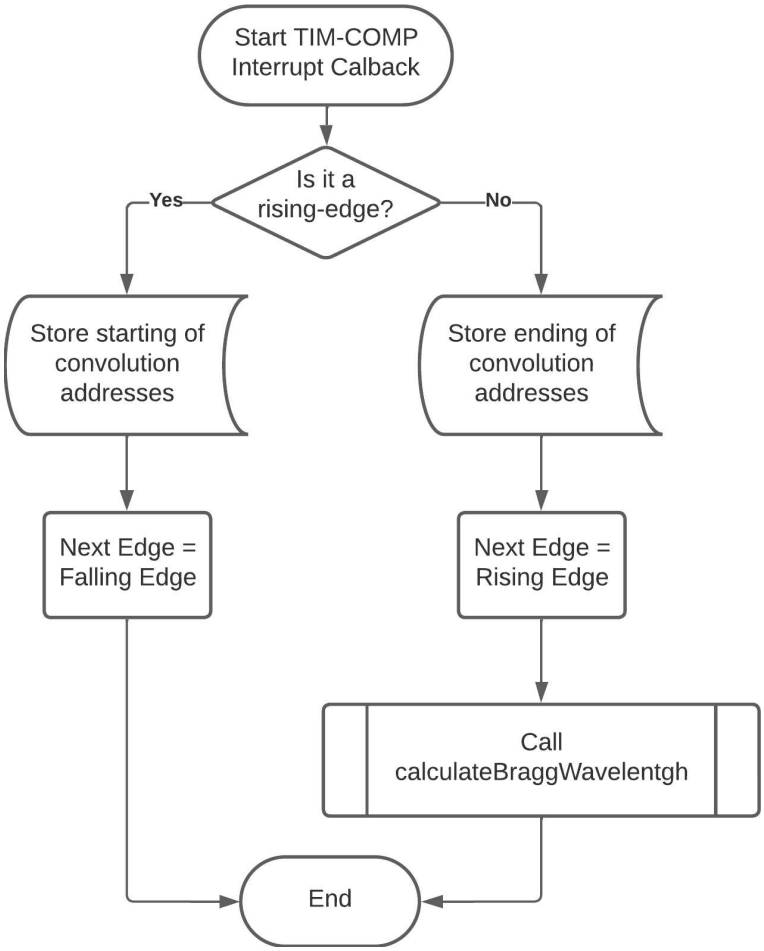

Figure 3.7 – TIM-COMP callback flowchart.

falling edge. For a rising edge, the current DMA addresses of both the ADC and DAC are saved as the starting point of a convolution event. In contrast, for a falling edge, the current addresses are saved as the ending point of the convolution. These addresses will later be used to identify which portion of the ADC buffer corresponds to the power convolution between a specific FBG and the tunable filter and which portion of the DAC buffer corresponds to the Bragg wavelength values of the tunable filter. Once a full convolution interval is identified (from rising to falling edge), the Calculate Bragg Wavelength function is called. This function uses the start and end DMA addresses to extract the relevant portion of the signal and perform the wavelength estimation.

Calculate Bragg wavelength function

The Bragg wavelength calculation function, illustrated by the flowchart in Figure 3.8, takes as inputs the DMA addresses, the buffer for A/D conversion, and the hysteresis lookup table. These parameters are utilized to construct two vectors containing all the rele-

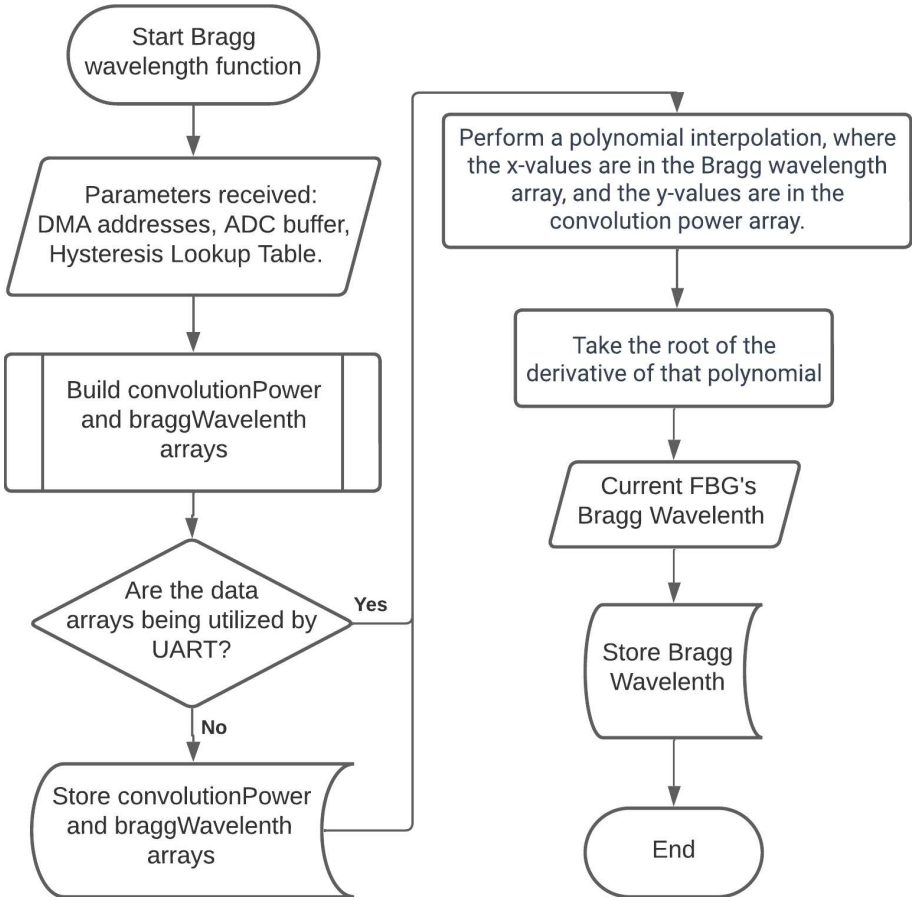

Figure 3.8 – Calculate bragg wavelength flowchart.

vant FBG-related values. One vector stores the convolution power data, while the other records the wavelength values.

The building of the arrays involves accessing the ADC buffer and the lookup table starting from the respective initial DMA point, sequentially recording values into the vector positions. Due to circular DMA configuration, the buffer access might reach its last position before vector completion. In such cases, the buffer access variable resets to zero, and the writing sequence in the vector continues. When the convolution power value drops to or below the initial convolution power value, the algorithm finalizes the array construction. This approach ensures that the final signal is symmetrical, regardless of whether the system is in the ascending or descending sweep of the tunable filter, thus providing better results in polynomial interpolation.

In the sequence, both vectors are stored in data memory (RAM) as global variables, to be later transmitted via UART to the interface for the visualization of the FBG spectrum. If the interface command state machine is currently sending these arrays to the user interface, a flag is set to bypass this storage process, preventing the function from overwriting the arrays while they are being transmitted.

Subsequently, these vectors are used to calculate the Bragg wavelength of the current FBG. This can be accomplished by identifying the wavelength value at which the convolution power reaches its maximum. However, obtaining this information by receiving the highest value from the convolution power vector is prone to errors due the signal noise. Additionally, the acquisition frequency might not provide an adequate number of data points for a precise estimation of the FBG's peak value. Therefore, to accurately determine the maximum value of the convolution power, a polynomial interpolation is first performed to approximate the convolution power and its respective wavelengh to a second-degree polynomial. Subsequently, the polynomial is differentiated, and the root of the derivative provides the wavelength value where convolution power is maximum, approximating the Bragg wavelength of the FBG. This obtained value is then stored in memory for later access from the user interface.

Interface command state machine

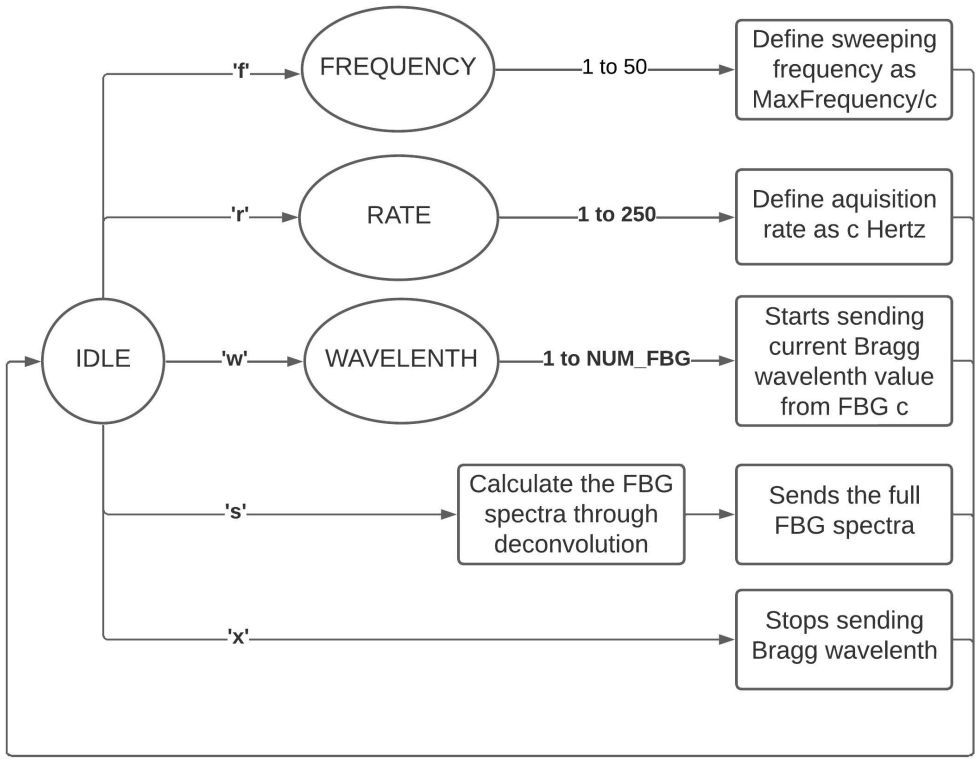

Figure 3.9 – Interface command state machine block diagram.

The proposed FBG array interrogator will be controlled via a computer using a USB/UART interface. This interface will allow for the configuration of parameters such as scanning rate and acquisition rate, and will also enable the retrieval of values such as the cur-

rent wavelength of the FBG or the complete spectrum of an FBG. The function described by the flowchart represented on Figure 3.9 serves as the core of a state machine designed to control system operations based on input received from the LabVIEW interface through UART communication. Some commands require an additional parameter, and there are specific states for each one of them after receiving the command to wait for this parameter. Whenever it receives a character that is not a valid command or a parameter outside the expected range, it returns the state machine to the Idle State, waiting for a valid command again. This approach minimizes the number of characters received per command. Here is a detailed breakdown of each command and its corresponding action:

Command "f" (frequency): This command puts the state machine into the Frequency State, waiting for the parameter indicating the frequency divisor. When the parameter is received, it adjusts the analog signal's output frequency by modifying the DAC timer's prescaler, ensuring the system's final scanning frequency is equal to the maximum frequency divided by the received parameter.

Command "w" (wavelength): Triggering this command initiates the process of reading the Bragg wavelength associated with a specific FBG, determined by the parameter received in wavelength State. The system initializes a timer with a frequency specified by the user through the "r" command. In this timer's interruption, the system transmits the current Bragg wavelength value associated with the identified FBG.

Command "r" (rate): Upon receiving this command, the system adjusts the frequency of the timer used by the "w" command to the corresponding parameter received in Rate State. This command should be received before starting the Bragg wavelength reading process, allowing control over the sampling rate of the user's interface.

Command "x" (exit): This command serves as a stop signal to the wavelength command, halting the timer used to send the current Bragg wavelength and stopping this process.

Command "s" (spectra): This command triggers the transmission of the FBG spectra by performing a deconvolution of the currently stored convolution power spectra with the tunable filter's profile. Once the deconvolution process is done, the system transmits the data in pairs, comprising wavelength and reflectivity values. During this sequence, it ensures that the Calculate Bragg Wavelength function does not overwrite any of these arrays, safeguarding the integrity of the data being sent or being used in the deconvolution calculations.

3.3.2 LabVIEW user interface

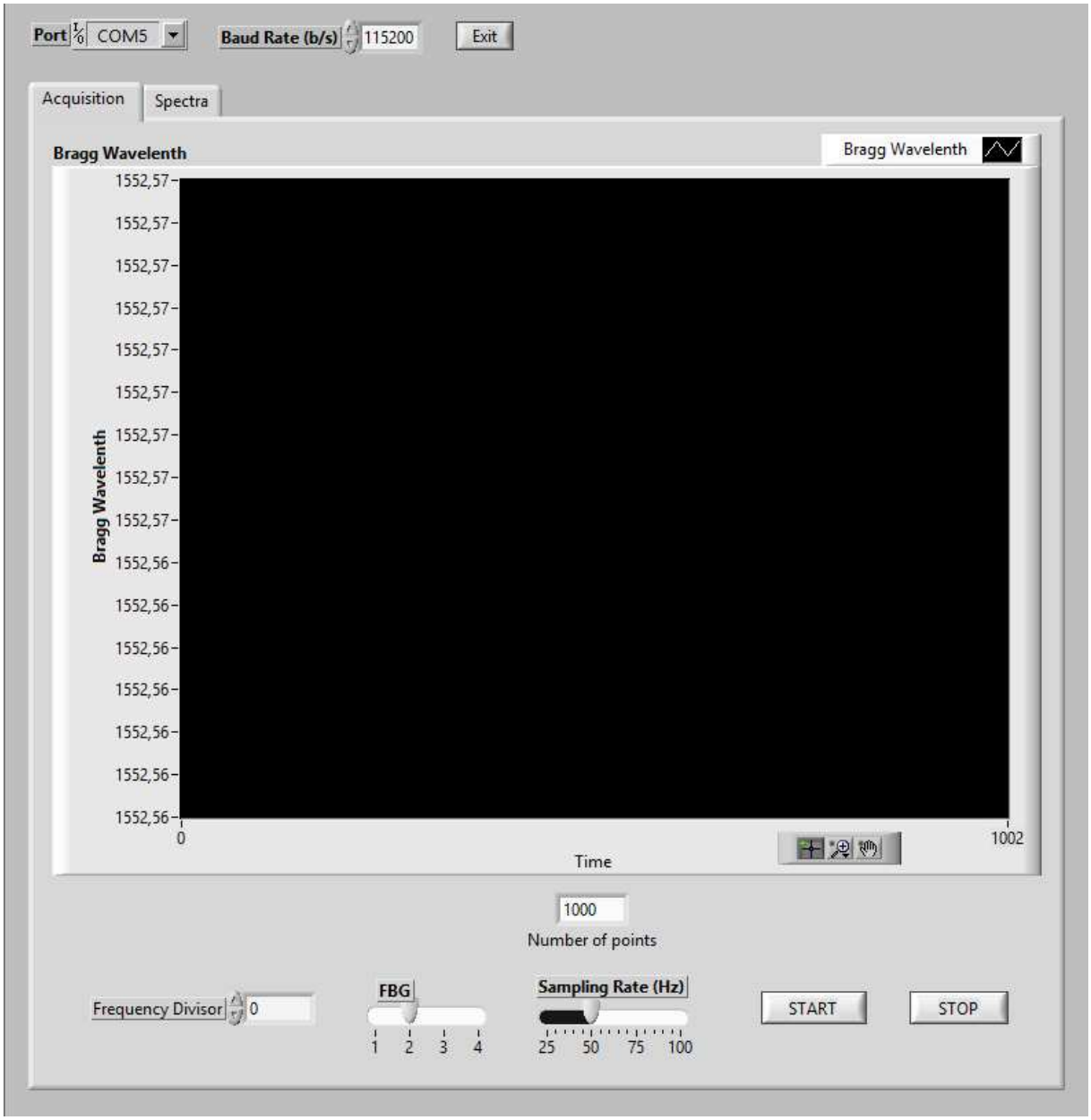

Figure 3.10 – LabVIEW user interface - Acquisition tab.

In the LabVIEW interface (Figures 3.10 and 3.11), users can perform multiple actions related to communication and data visualization with the microcontroller. The interface consists of two tabs, which can be switched using a the buttons "Acquisition" and "Spectra". Each tab provides access to different functionalities and displays.

Initially, they select the appropriate COM port and baud rate settings to establish communication by inserting these values on the corresponding boxes. To terminate the communication session, users can use the "Exit" button.

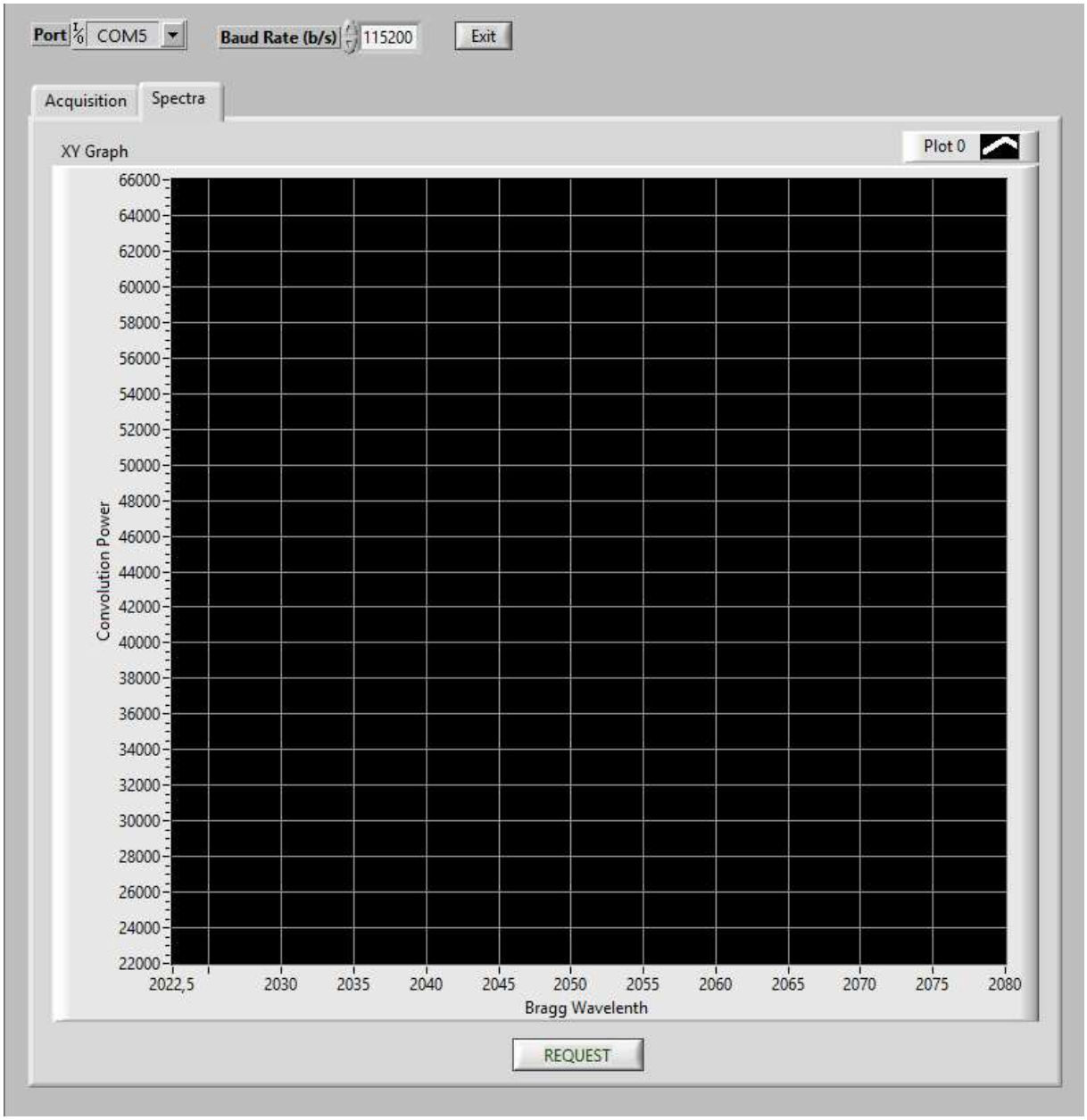

Figure 3.11 – LabVIEW user interface - Spectra tab.

Once the communication is established, users can engage in four main functionalities, which communicate with the microcontroller using the commands presented in the Interface command state machine section:

Changing scan frequency: Users can adjust the scanning frequency by selecting the desired frequency divisor in the provided box. This action triggers LabVIEW to send an "f" command to the microcontroller.

Initiating Bragg wavelength reception: In the "Acquisition" tab, users can select the FBG and set the sampling rate in the related pointer slides and then click the "Start" button in order to receive Bragg wavelengths. This action triggers the LabVIEW to send an "r" command

followed by a "w" command to microcontroller. As a result, Bragg wavelengths start showing on the graph.

Stopping Bragg wavelength reception: Before performing any other action in LabVIEW, users must stop the Bragg wavelength reception by clicking the "Stop" button. This action sends an "x" command to the microcontroller.

Requesting current spectra: Switching to the "Spectra" tab, users can retrieve the current spectra data and display it on the graph by clicking the "Request" button. This action prompts LabVIEW to send an "s" command to the microcontroller.

3.4 Temperature compensation module

To improve the accuracy of the FBG interrogation system measurement, a temperature stabilization module was implemented. This module controls the temperature of the reference FBG, which is used as a static baseline for compensation of thermal drift across the tunable grating.

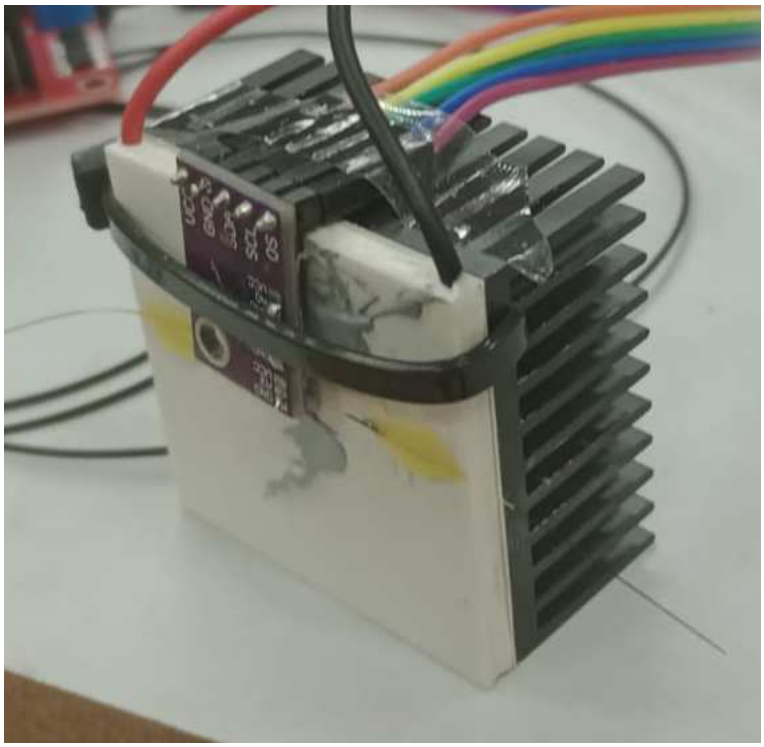

Figure 3.12 – Temperatrue stabilization module.

The temperature stabilization module, presented in Figure 3.12, consists of a Peltier element as the thermal actuator, driven by an H-bridge circuit. For feedback, it uses the LM75A temperature sensor (NXP, 2007), positioned on the hot side of the Peltier element.

A proportional-integral (PI) controller was selected to regulate the surface temperature of the hot side of the Peltier element, with a setpoint fixed at 50°C - slightly above ambient conditions. Operating at this elevated temperature improves system stability by taking advantage of the fact that the Peltier, when not refrigerated by a very efficient cooling system, warm up the cold side to temperatures above the ambient. Attempting to regulate near room temperature would lead to excessive self-heating and difficulty maintaining the set point. This controlled thermal environment ensures reliable temperature stabilization for the reference FBG.

The reference FBG is attached directly to the surface of the Peltier, where the temperature is actively regulated. Because this FBG is not subjected to any mechanical strain and its temperature remains constant, its Bragg wavelength is expected to remain unchanged. Assuming that any deviation between the expected and measured Bragg wavelength of the reference FBG results from thermally induced variations in the tunable filter—and that these variations behave approximately linearly within the operating range—the temperature compensation algorithm applies a dynamic offset correction. Whenever a Bragg wavelength is calculated within a narrow range around the known value of the reference FBG, the interrogator algorithm computes the difference between the measured and predefined wavelength. This difference is stored as an offset and is subsequently subtracted from all Bragg wavelength measurements of the sensing FBGs in the array.

4 SIMULATION AND EXPERIMENTAL VALIDATION

In this chapter, we present both simulated and preliminary experimental results of the interrogation system. Overall, two primary simulation methodologies have been implemented. First, we performed an analysis of the algorithms employed in the interrogator using Matlab software. This involved simulating the FBGs data while systematically varying signal and algorithm parameters to estimate the performance of the actual system in advance. The codes used for these simulations are presented in Appendix A.

Furthermore, the firmware and key interrogator algorithms were developed on the STMH745 (STM Microelectronics, 2023) board, employing the microcontroller's D/A converters to emulate the signal derived from the FBGs and direct it to the inputs of both the A/D converter and comparator.

Finally, this chapter concludes with practical measurements obtained from the operational interrogator system implemented in the laboratory. These results include the Bragg wavelength tracking of a single FBG sensor subjected to constant mechanical stress, with data collected and processed using LabVIEW and MATLAB. Additionally, several validation experiments are presented, including tests for the temperature compensation module, hysteresis compensation, strain tracking under dynamic excitation, and a final evaluation using a Fabry-Perot tunable filter.

4.1 Matlab results

The Matlab simulation of the interrogator involved the simulation of an FBG signal with a Full Width at Half Maximum (FWHM) of 0.25 nm and a Bragg wavelength of 1550 nm by approximating the reflection curve to a sinc function. A noise component, characterized by the RMS value determined in the noise analysis stage introduced in the Chapter 3, was then added to this signal. Additionally, several parameters were defined: (i) the discretization period, which represents the wavelength difference between two points acquired in the real system and varies with the acquisition frequency and the system's scanning speed; (ii) the noise multiplier, utilized to estimate the system's robustness by adjusting it during simulation; (iii) threshold values, related to the thresholds defined in the COMP module of the microcontroller as explained in the Software section of the Interrogator Design chapter; (iv) and the degree of the polynomial

to be considered in polynomial interpolation.

With the generated signal and defined parameters, the algorithm performs a sequence similar to the one designed for the microcontroller. This involved discretizing the original signal based on the discretization period, simulating the interrogator's acquisition process. The algorithm then selectively retained discrete signal points corresponding to the peak reflection of the FBG based on the defined thresholds, simulating the COMP module's operation. Subsequently, it performs a polynomial interpolation with these points, then evaluates this polynomial in the wavelength working interval and finds its maximum value, simulating the process of finding the Bragg wavelength, as explained in the Section 3.3.1 of the Interrogator Design chapter. All the steps performed on the simulated FBG signal are illustrated in Figure 4.1.

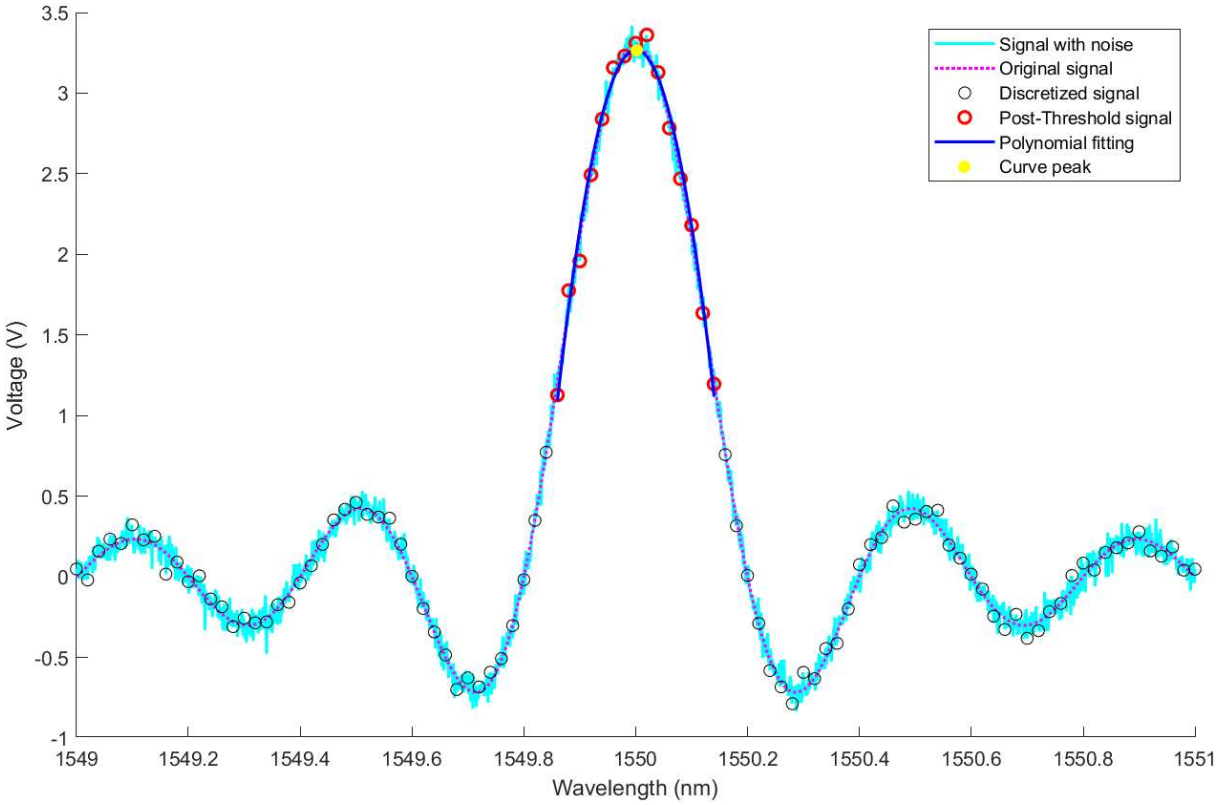

Figure 4.1 – Simulation of the interrogator algorithm.

Finally, the algorithm calculates the error associated with the resulting Bragg wavelength and the actual value of the simulated FBG's Bragg wavelength. Through repeated iterations of this procedure, it is possible to find values such as average error and standard deviation. Moreover, it is possible to vary all the previously defined parameters to establish a ratio between each of these parameters and the obtained average error and standard deviation. This facilitated the estimation of factors such as the system's robustness or optimal conditions for minimizing error.

Varying noise multiplier

In the first step, we vary the variable responsible for multiplying the previously computed noise, spanning a range from 1 to 800. The interrogator algorithm was then applied to a simulated noisy signal for each multiplier value. Subsequently, the average error and standard deviation were computed across 1000 distinct instances of the simulation, comparing each outcome with the known Bragg wavelength of the corresponding signal. Also, in each instance, the simulated Bragg wavelength was randomly altered within a range of -50 pm to +50 pm relative to the original wavelength. This ensures the robustness of the results even when the Bragg wavelength varies, as is expected to happen in practical scenarios. A graphical representation (see Figure 4.2) was constructed to outline the correlation between the multiplied value over the system's base noise and the resulting average error and standard deviation.

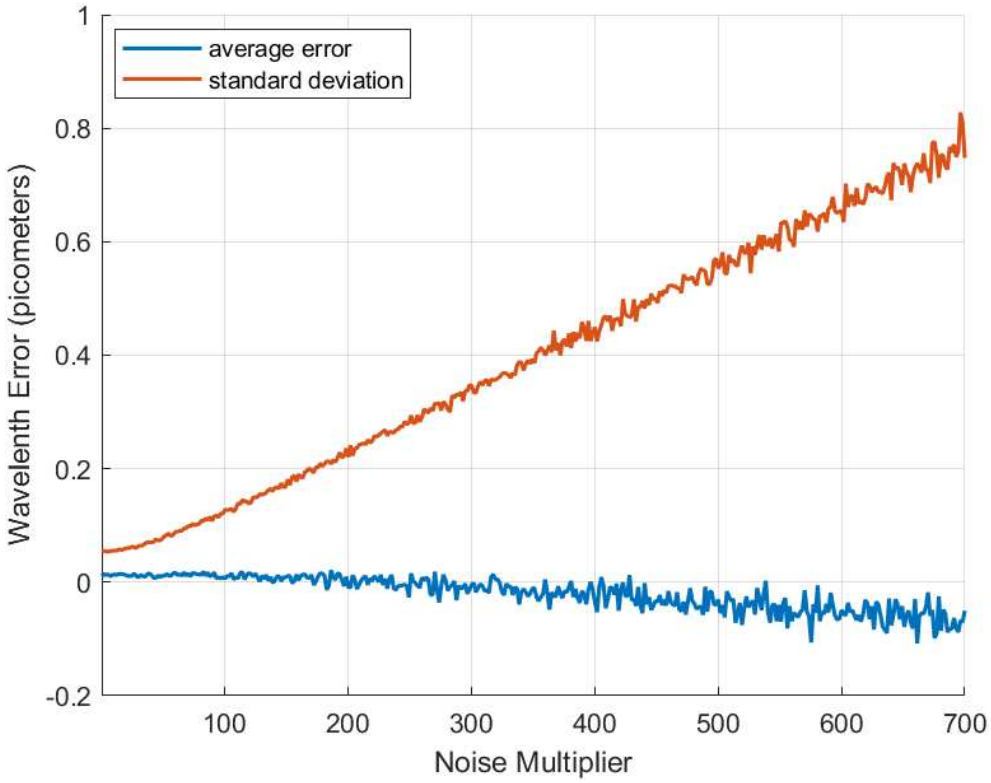

Figure 4.2 – Average Error and Standard Deviation vs. Noise Multiplier Graph.

The graph reveals an approximately linear correlation between the standard deviation and the noise, while the average error remained consistently close to zero. Furthermore, even for noise levels up to 500 times the calculated value, the standard deviation does not exceed 0.6 pm and shows small fluctuation. It's important to note that the average error is directly related to the algorithm's accuracy and may indicate any systematic errors present, whereas the standard deviation is related to the algorithm's precision, which will affect the system's resolu-

tion. These results suggest that the system exhibits significant resilience to noise, ensuring that any potential imperfections in the interrogator's electronic development have a minimal impact on the expected performance.

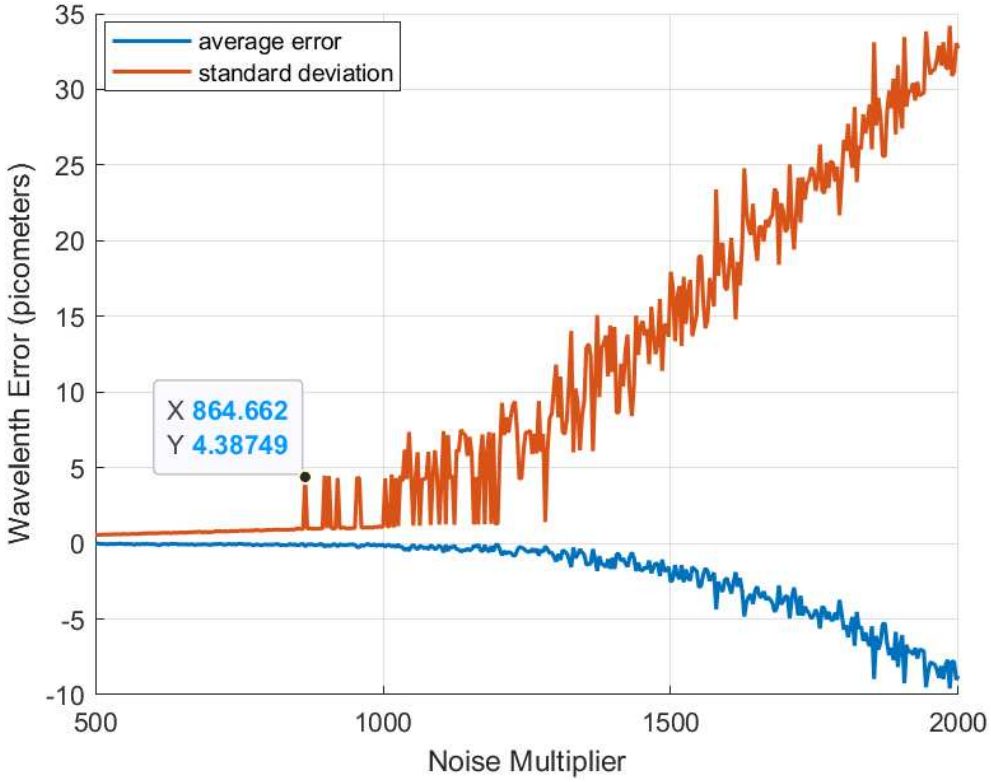

Figure 4.3 – Average Error and Standard Deviation vs. Noise Multiplier Graph - Higher noise values.

After establishing the linear correlation between noise levels and system resolution, we proceeded to conduct further simulations with increased noise levels to identify the point at which the algorithm begins to lose accuracy in detecting the Bragg wavelength of the FBG. Figure 4.3 presents a graph where the noise multiplier ranges from 500 to 2000. As depicted, there is a noticeable deviation from the expected linear trend at a noise multiplier of approximately 864, where the error values begin to escalate significantly. To investigate the underlying cause, we performed a detailed analysis of the FBG spectrum for all simulated signals, as illustrated in Figure 4.4.

From this simulation, it is evident that the main cause of the high error is that the noise amplitude may surpass the difference between the two thresholds used in the comparator. As a result, the algorithm could mistakenly identify a falling edge very close to the initial point, leading to an incomplete identification of the FBG spectrum. To address this issue under high noise conditions, a simple solution would be to increase the gap between the thresholds to a

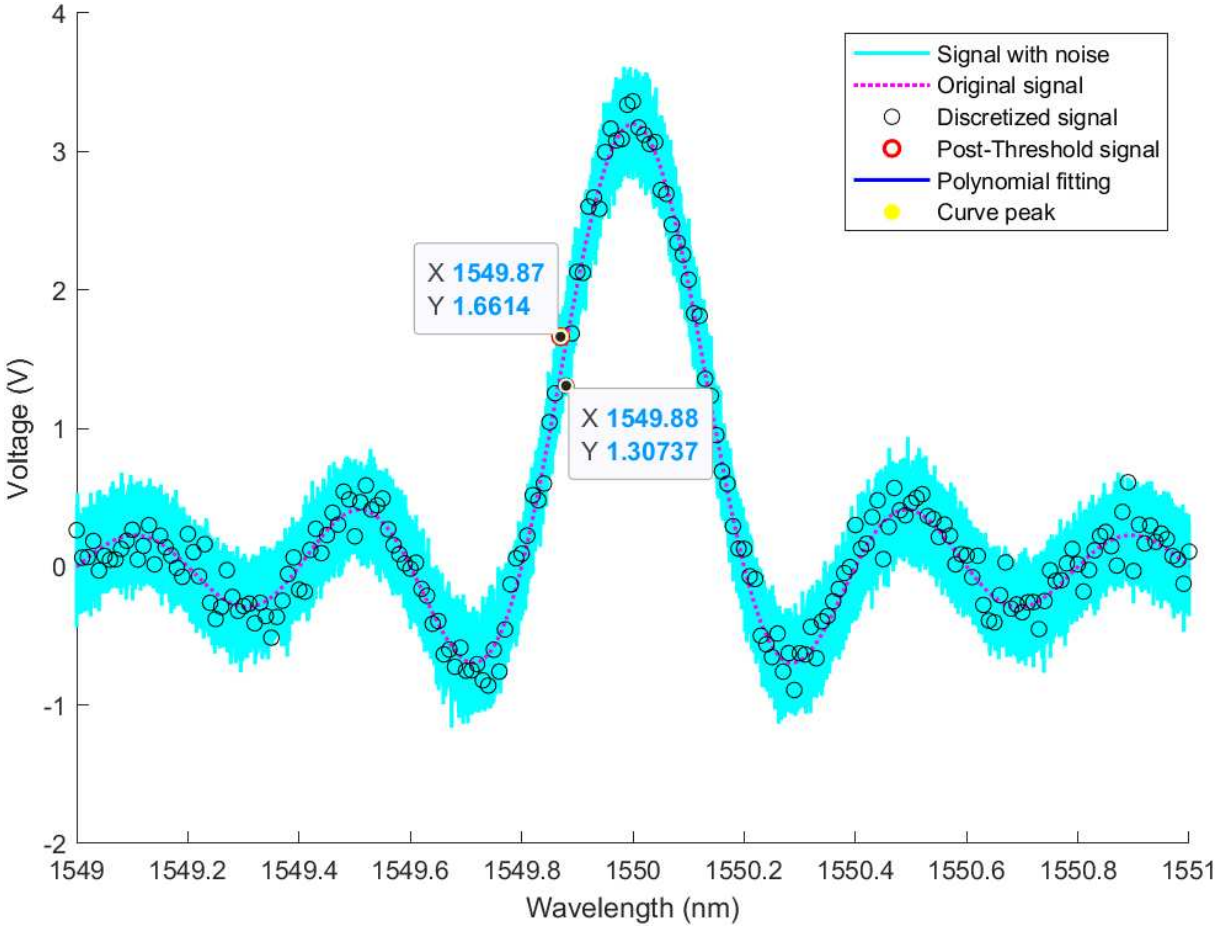

Figure 4.4 – Simulation of the interrogator algorithm for a noisier signal.

value greater than the noise amplitude. However, since the expected noise level is much lower than the value that would cause this situation, this adjustment could be considered for future implementation to further enhance the system's robustness against noise.

Varying other parameters

We systematically adjusted other parameters to understand their effects on the interrogator's performance, focusing specifically on the wavelength discretization distance, representing the distance between two discrete wavelength points, which is inversely proportional to the acquisition rate; the threshold value in the comparator; and the degree of the polynomial used for interpolation. Throughout these investigations, we maintained the signal noise at the level calculated in the previous chapter. Moreover, we maintained a constant value of 0.006 pm for the wavelength discretization distance, 40% for the threshold, and 2 for the polynomial degree across all simulations, except for the parameter under variation in each case. The outcomes of these parameter variations are illustrated in Figures 4.5, 4.6, and 4.7.

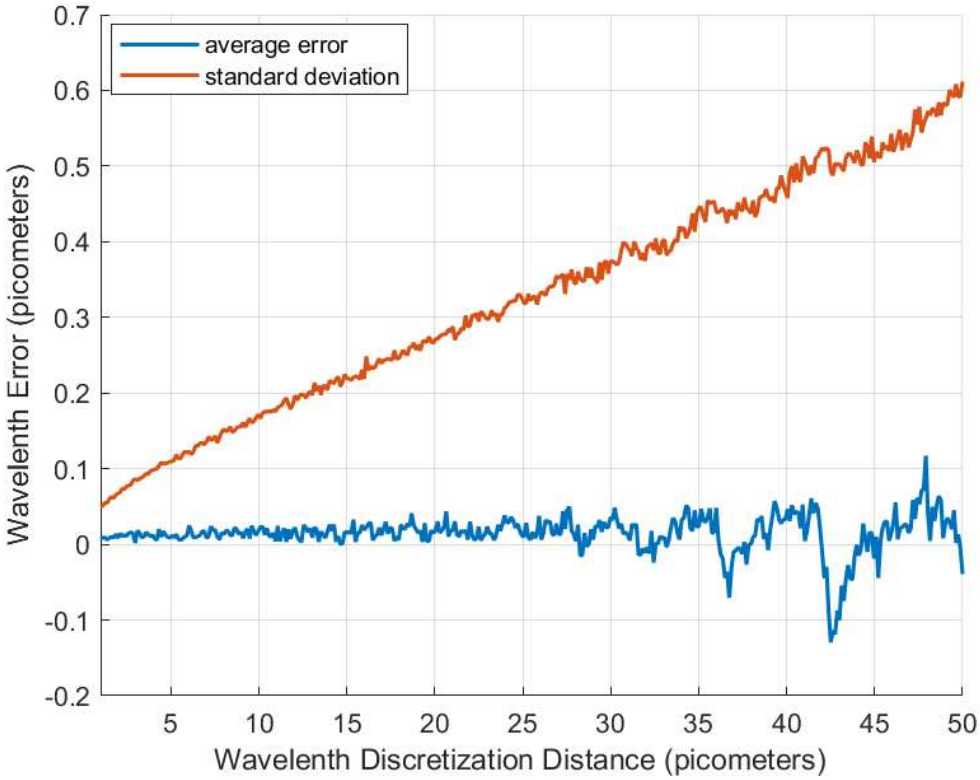

Figure 4.5 – Average Error and Standard Deviation vs. Wavelength Discretization Distance Graph for a Low-Noise Signal.

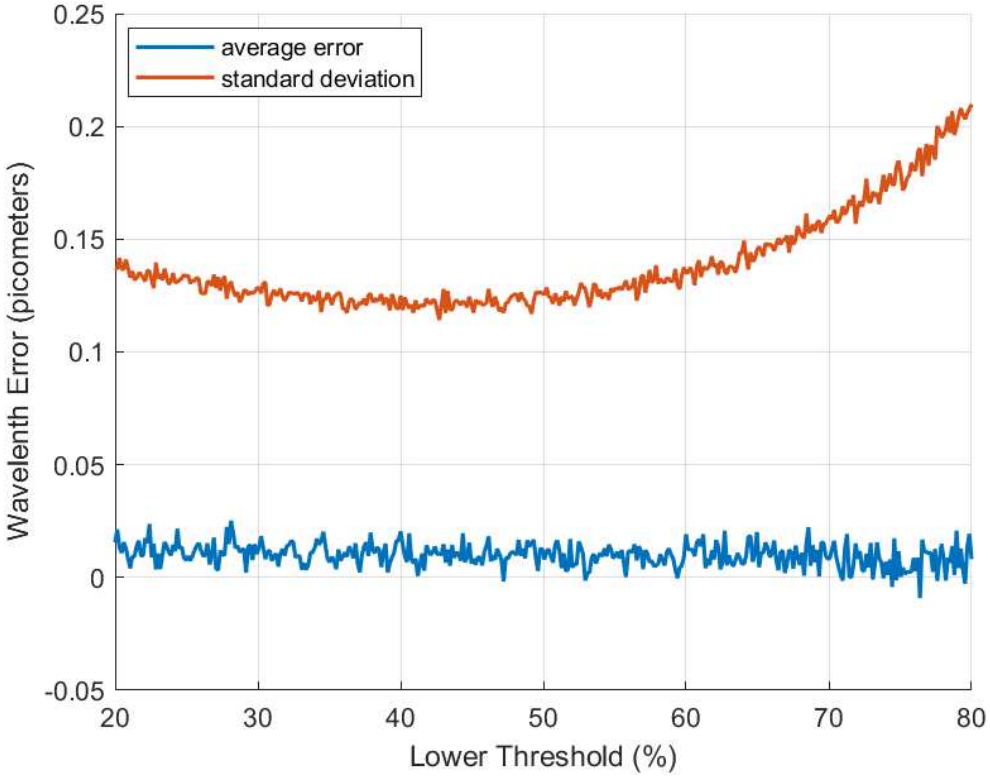

Figure 4.6 – Average Error and Standard Deviation vs. Threshold Graph for a Low-Noise Signal.

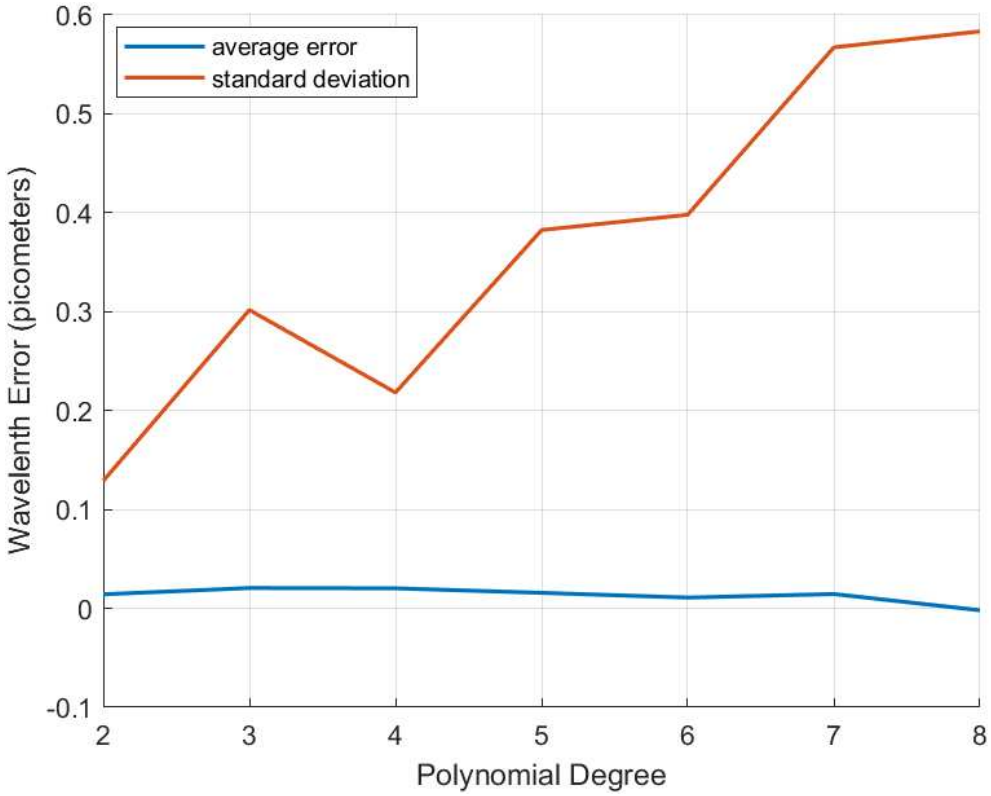

Figure 4.7 – Average Error and Standard Deviation vs. Polynomial Degree Graph for a Low-Noise Signal.

The tests involving variations in the wavelength discretization distance (Figure 4.5) revealed a linear correlation with the standard deviation and a significant, systematic fluctuation in the average error as the wavelength discretization distance increased. One plausible explanation for this observation is that polynomial interpolation may yield considerably better results for determining the curve peak value when there is more sample points of the fitting curve. With few points, the noise and the fact that the sampled points are not symmetrically distributed around the peak may introduce peak identification error. In practical scenarios, the reflected spectrum's width for different FBGs is unlikely to be as perfect and predictable as the sinc function, making the expected results worst than the presented in these simulations. Regarding the threshold values (Fig, 4.6), it was noted that the average error remained close to zero across all thresholds, while the standard deviation reached its minimum value for thresholds between 40% and 50%. Lastly, in the variation of the polynomial degree (Figure 4.7), it is evident that the standard deviation increases as the polynomial degree rises, with the 2nd and 4th degrees yielding the lowest standard deviation values. Next, to corroborate the robustness of the outcomes obtained from the preceding three graphs, additional simulations were executed with variations in the same parameters (wavelength discretization distance, threshold and

polynomial degree). However, these simulations were conducted under conditions of noise 800 times higher. The Figures 4.8, 4.9 and 4.10 present the results of these simulations.

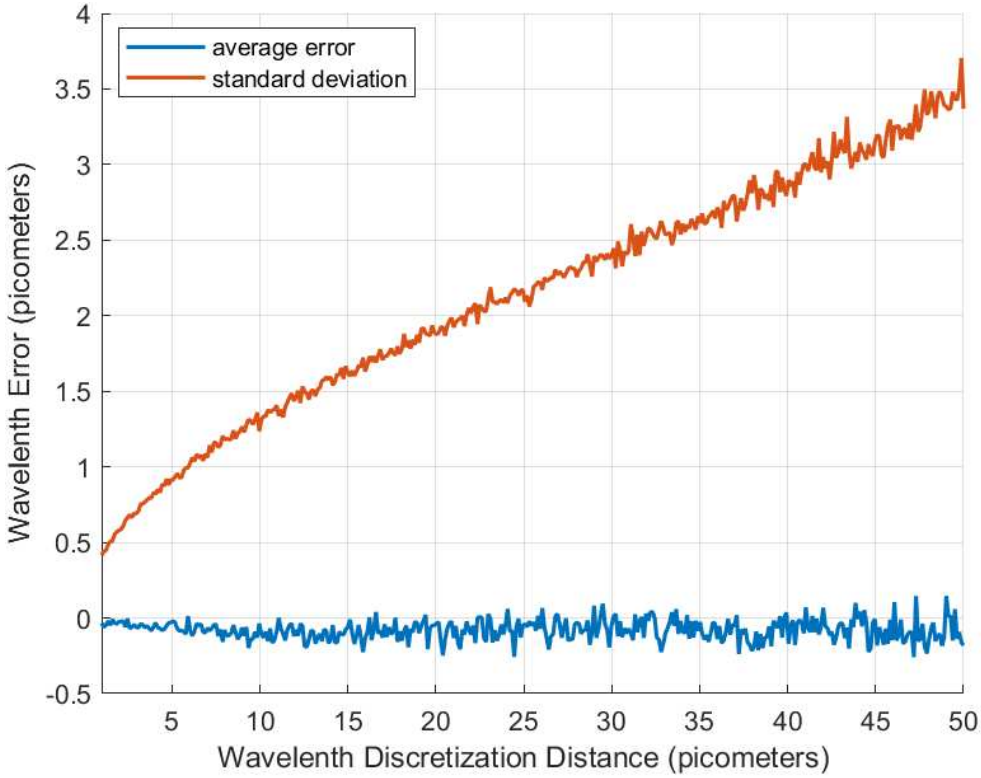

Figure 4.8 – Average Error and Standard Deviation vs. Wavelength Discretization Distance Graph for a High-Noise Signal.

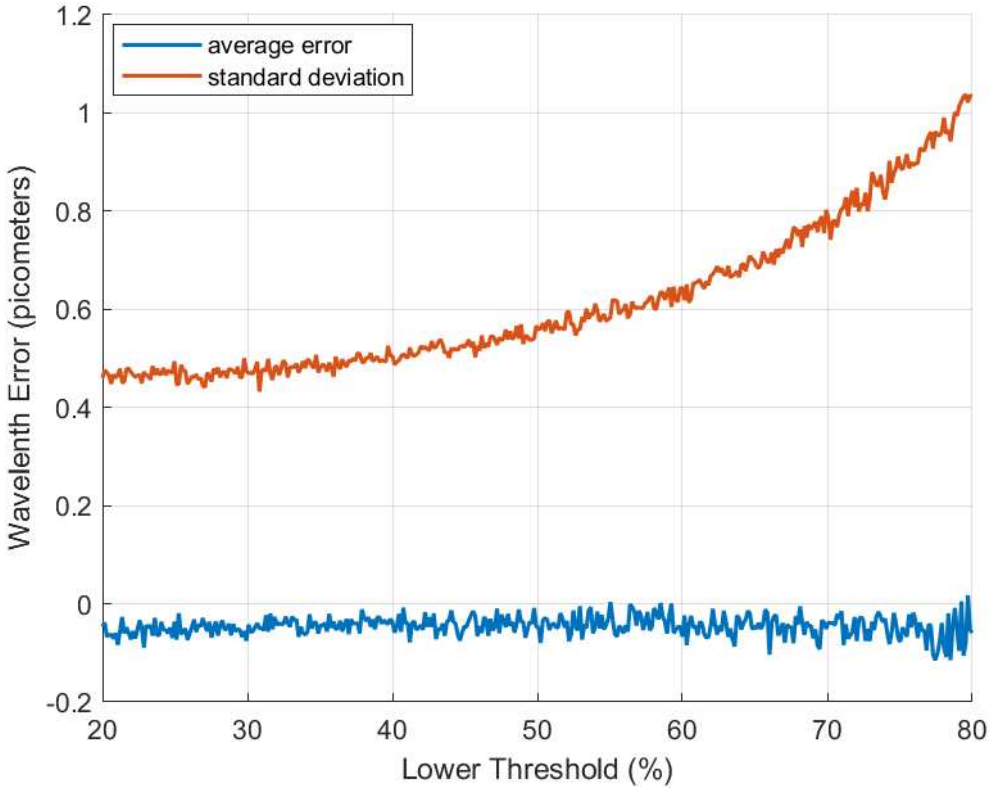

Figure 4.9 – Average Error and Standard Deviation vs. Threshold Graph for a High-Noise Signal.

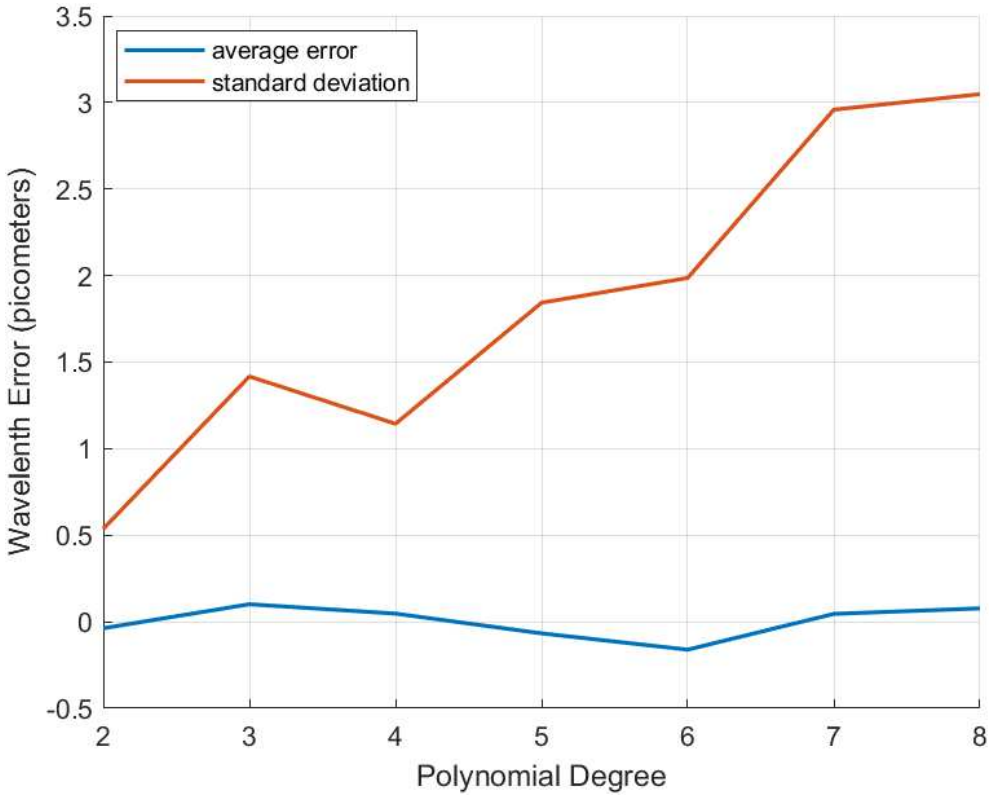

Figure 4.10 – Average Error and Standard Deviation vs. Polynomial Degree Graph for a High-Noise Signal.

Now, with the introduction of a noisier signal, the results corroborate the tests carried out for low noise. The wavelength discretization distance graph (Figure 4.8) exhibited similar patterns to those with low noise, with the main difference being a higher overall error, as expected. Furthermore, it can be inferred that reducing the discretization distance (by increasing the acquisition rate or reducing the scanning speed) to less than 5 pm consistently reduces the noise level to less than 1 pm. In the threshold graph (Figure 4.9), it is observed that for a noisier signal, thresholds between 40% and 50% are no longer optimal, with lower errors ocurring at thresholds between 20% and 30%. Lastly, regarding the polynomial degree graph (Figure 4.10), it corroborates that the second-degree polynomial is the more robust choice, as higher degrees result in significantly greater errors. Moreover, working with higher-order polynomials is computationally more demanding and may lead to processor overload. Therefore, using second-degree polynomials proved to be the optimal choice when evaluating both accuracy and execution time.

4.2 Emulation results

To validate the proposed algorithms, they were implemented in the (STM Microelectronics, 2023) microcontroller and tested with an emulated optical signal. The methodology employed for the simulation involved the emulation of the signal that would be returned by the optoelectronic circuit utilizing the DAC module. It is crucial to emphasize that, rather than using the DAC for direct control of the PZT, the utilization of the module was on emulating the signal of the optical circuit. Figure 4.11 provides an illustration of the optoelectronic circuit emulation process in a diagram, directly correlating with Figure 3.1, presented in the Chapter 3 - Interrogator Design. This emulation process doesn't require the use of any optical components, transimpedance amplifiers, or PZT actuators, allowing for the validation of the developed algorithms and the temporal control of the firmware that implements them. In the context of the acquisition process, the methodology remained the same as the explanation provided in the Interrogator Design chapter, incorporating both the ADC and the COMP modules.

Next, we present the results related to the data emulation, acquisition and the calculation of the Bragg wavelength for four FBGs. The graphs presented here had their data obtained from an oscilloscope, from the STM platform IDE and from LABView user's interface.

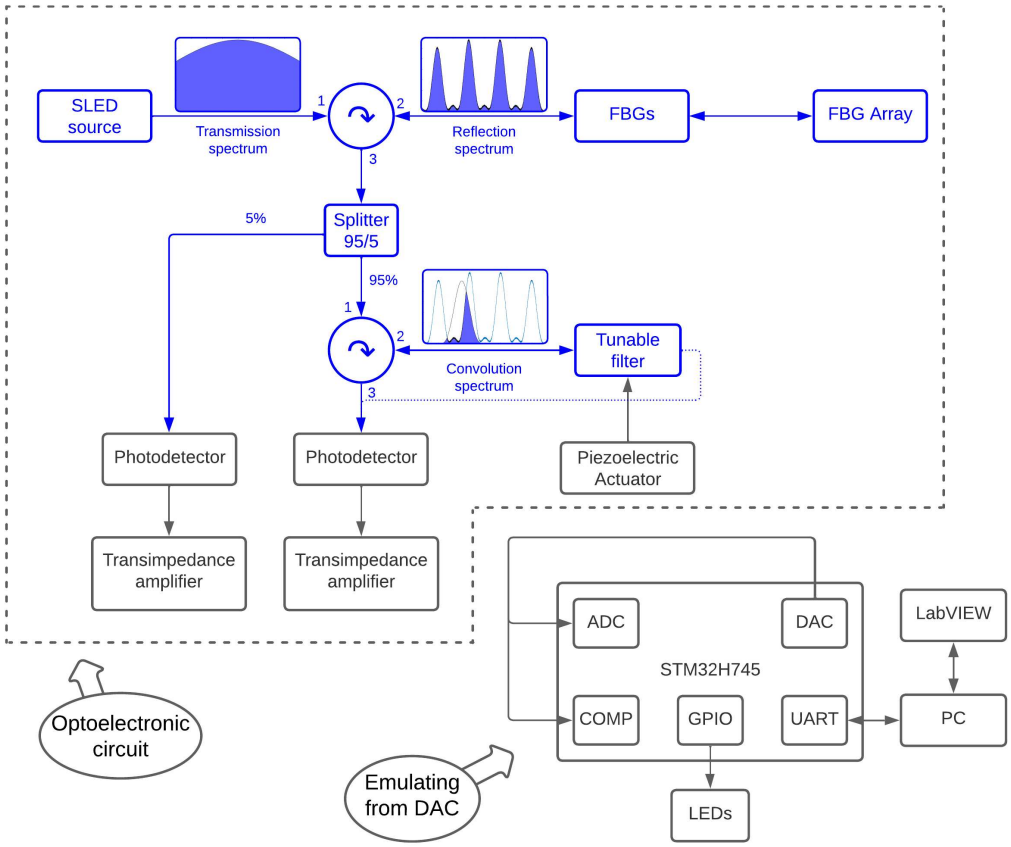

Figure 4.11 – Emulated optoelectronic circuit diagram.

Data acquisition results

Figure 4.12 presents the screen of the oscilloscope used to acquire the signals generated by the emulator. The signal acquired by Chanel 1 (cyan) corresponds to the convolution of the tunable FBG with four sensing FBGs, in both the ascending and descending phases of the tunable grating's sinusoidal excursion. Another auxiliar signal, displayed in yellow, sinalizes whether the current FBG is the first one, denoted by a low signal, or any other FBG, denoted by a high signal. Each cycle of the sinusoidal excursion starts with the yellow signal at a low value, representing the first FBG in the sequence. Following this, six FBGs are indicated by the yellow signal at high value. The first three represent FBGs 2, 3, and 4, respectively, in the ascending phase of the tunable filter's excursion, while the other three represent FBGs 4, 3, and 2 in the descending phase. The cycle ends with a final FBG at a low yellow signal, representing FBG 1, before the process repeats.

Figure 4.13 presents a detailed view of a single FBG (cyan signal), accompanied by a signal depicted in purple that represents the output of the DAC that provides the reference signal to the analog comparator (COMP) – both are embedded in the microcontroller. This signal

Figure 4.12 – Oscilloscope Emulation Results - Displaying Data from All Four FBGs.

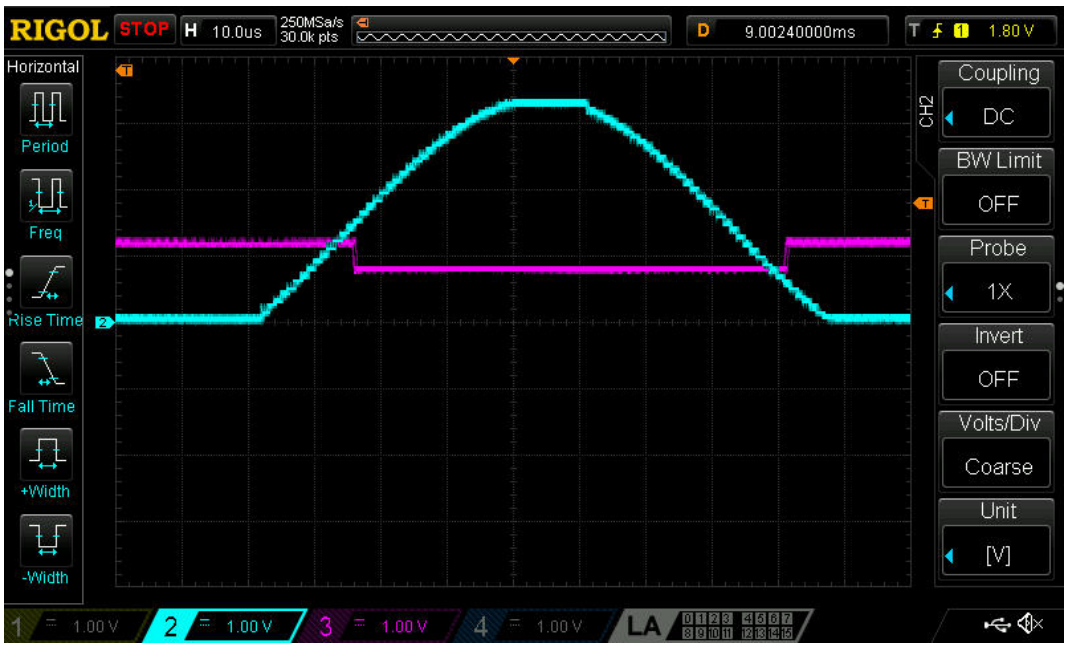

Figure 4.13 – Oscilloscope Emulation Results - Zoomed-in View of a Single FBG.

serves as a visual indicator, highlighting the distinction between the higher and lower thresholds. As the FBG signal intersects with the higher threshold, the system adjusts the comparison value to the lower threshold until it intersects with the FBG signal once more. It's important to note that this adjustment occurs a few microseconds after the intersection, as a result of the time taken by the microcontroller to enter the comparator's interrupt. Therefore, it is possible to see the proper functioning of the COMP's Callback function.

Figure 4.14 presents the vector of points acquired by the ADC. Additionally, the

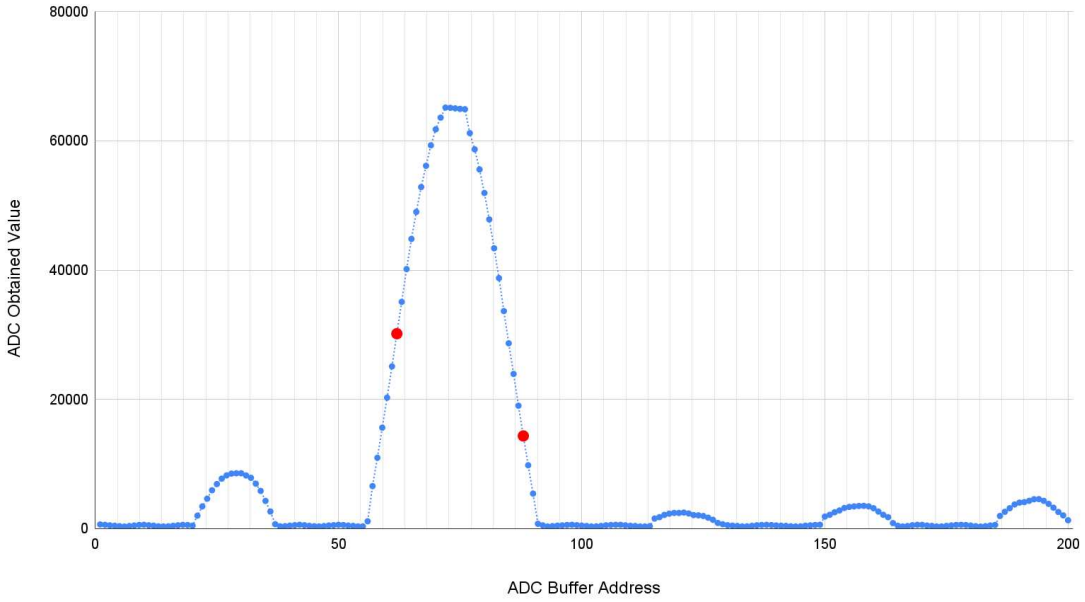

Figure 4.14 – Acquisition Results - Data Obtained from the ADC and COMP Modules.

buffer addresses obtained at corresponding COMP interruptions are depicted below and by red dots on the graph, indicating the beginning and the end of a FBG as perceived by the interrogator. It's noteworthy to emphasize that the x-axis of this graph solely denotes the address of each point from the ADC buffer. Moving on to Figure 4.15, we observe the same set of points through the LabVIEW interface, which represents the entire FBG spectrum obtained. However, in this case, we have removed all values lower than the higher threshold to ensure the signal is more symmetrical, thereby preventing the polynomial interpolation from leaning to one side, as mentioned in Section 3.3.1. Also, the x-axis represents the Bragg wavelength of the tunable grating related to each convolution power. These are indeed the data points used to perform the polynomial interpolation.

Both Figure 4.14 and Figure 4.15 display an unexpected behavior near the peak of the spectrum, characterized by a spike that is not present in the oscilloscope image shown in Figure 4.13. This discrepancy led to the identification of a saturation problem occurring near the reference voltage within the microcontroller's ADC module, a phenomenon not documented in any of STM's official manuals. To address this, we re-conducted the emulation with the curve attenuated by 10%, thereby ensuring that the voltage at the ADC input remained below its reference voltage. The revised results of the points acquired by the ADC and the updated visualization of the spectrum in LabVIEW are shown in Figures 4.16 and 4.17.

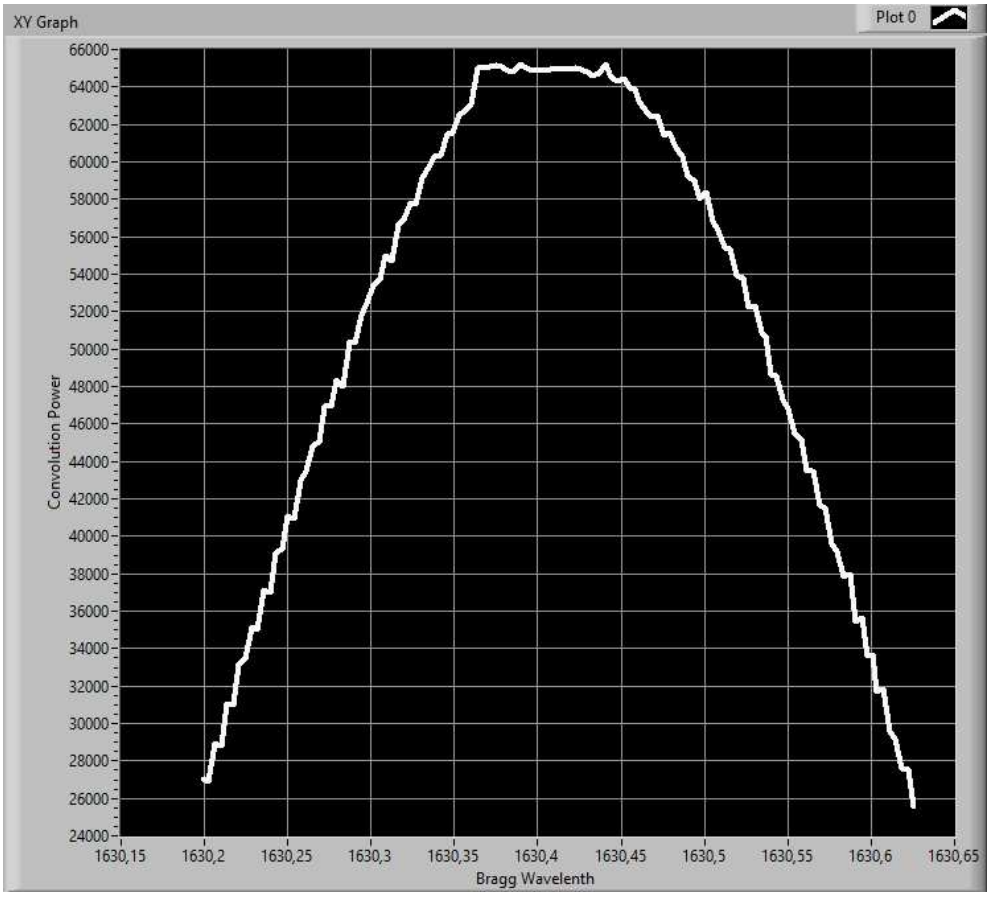

Figure 4.15 – LabVIEW Acquisition Results - FBG Spectrum.

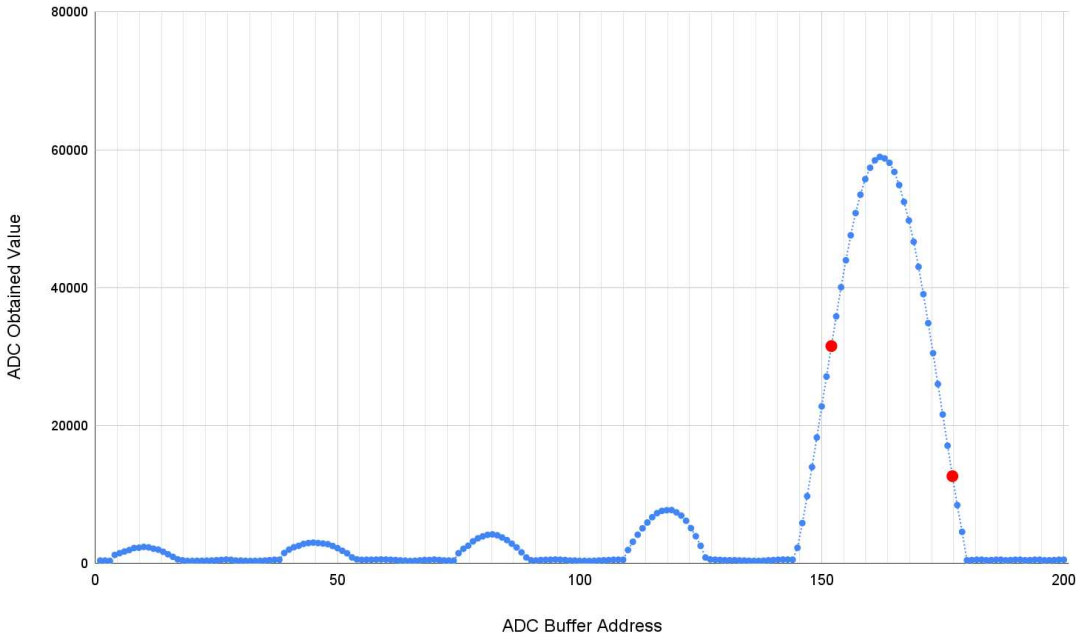

Figure 4.16 – Acquisition Results - Data Obtained from the ADC and COMP Modules - 10% Attenuated Signal.

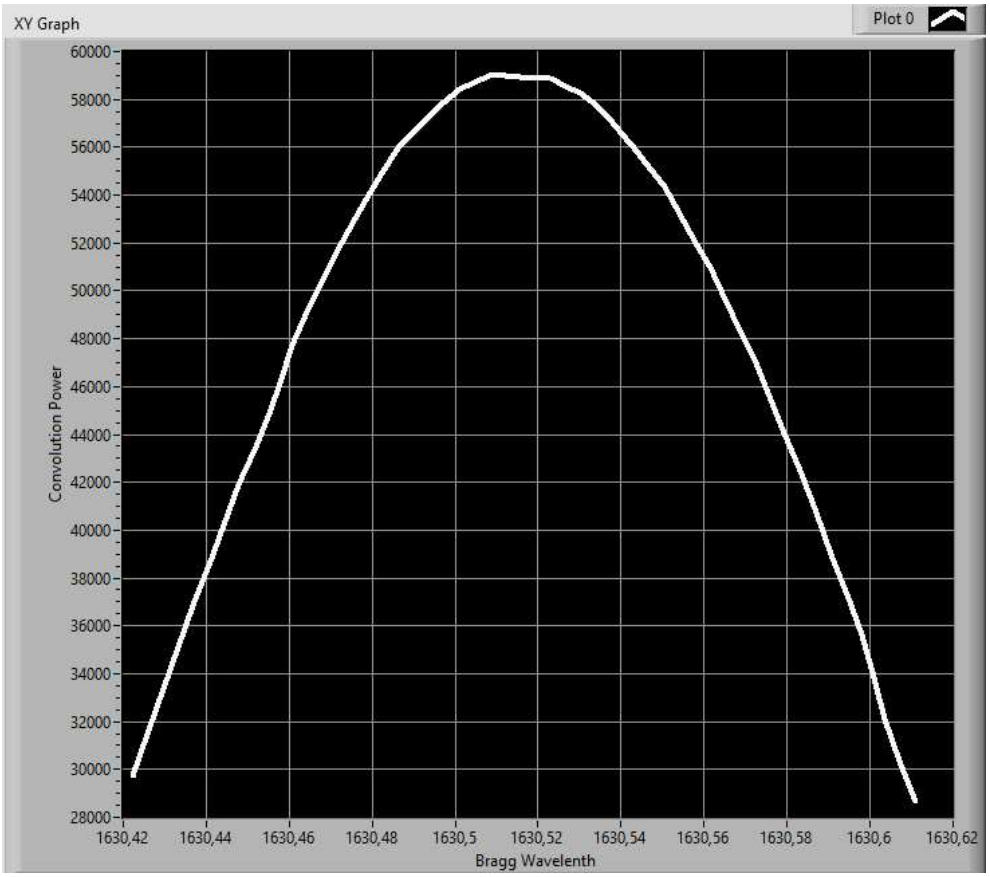

Figure 4.17 – LabVIEW Acquisition Results - FBG Spectrum - 10% Attenuated Signal.

Bragg wavelenth results

Figures 4.18 to 4.21 present an analysis of the Bragg wavelength for each of the four FBGs emulated. Each graph depicts the Bragg wavelength variation over time for a specific FBG, as acquired through the LabVIEW interface. The values obtained from the emulation show fluctuations of less than 0.01 pm, significantly below the project requirement of 5 picometers resolution. This demonstrates that the data processing method used can provide optimal results. Further work is needed to evaluate the overall system's performance and ensure if it can match the data processing capabilities.

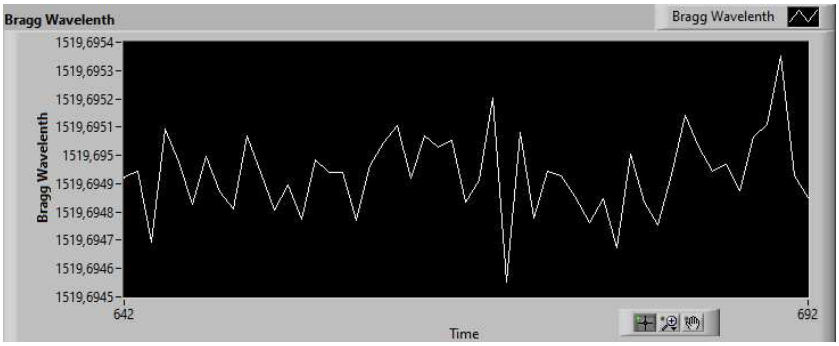

Figure 4.18 – Bragg Wavelength Results - FBG 1.

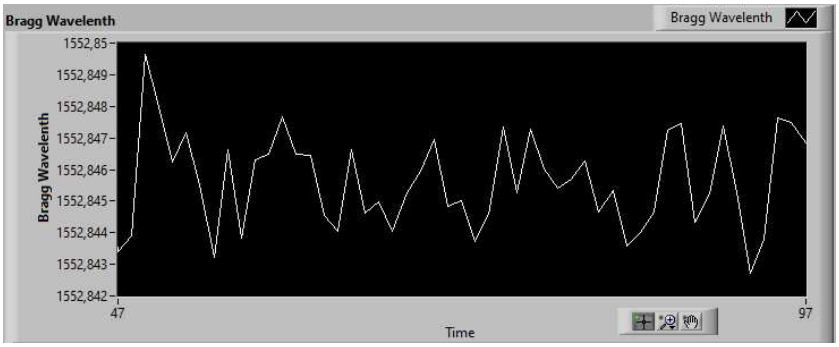

Figure 4.19 – Bragg Wavelength Results - FBG 2.

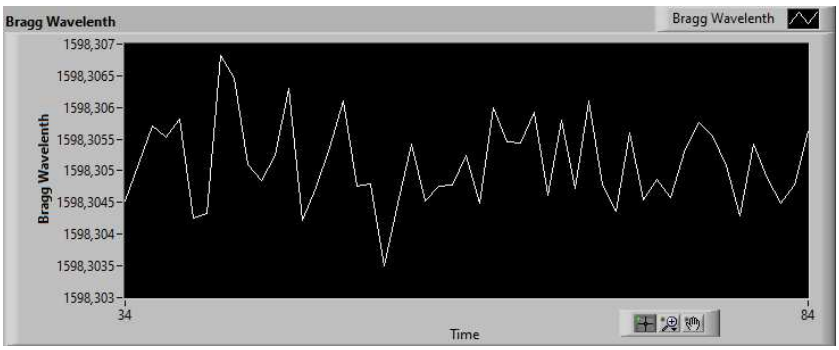

Figure 4.20 – Bragg Wavelength Results - FBG 3.

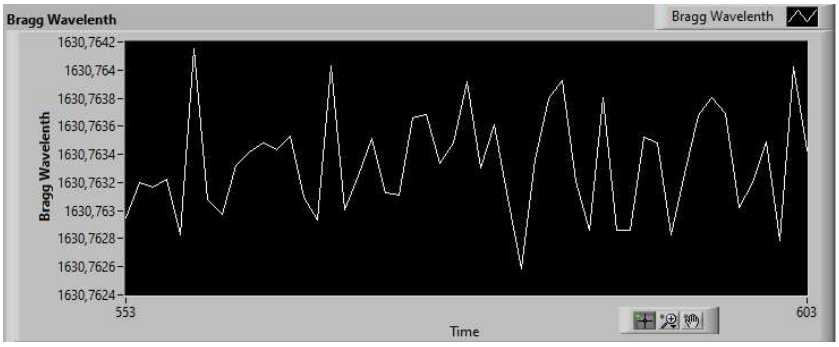

Figure 4.21 – Bragg Wavelength Results - FBG 4.

4.3 Experimental Results

This section presents the experimental validation of the developed interrogator, including tests that demonstrate the functioning of specific subsystems, such as the hysteresis compensation, temperature compensation, and outlier filtering. Figure 4.22 shows the experimental setup used to validate the interrogation system. The setup includes the optical components, the FBG tunable filter module, the signal acquisition circuitry and the microcontroller board responsible for real-time processing. This setup corresponds to the practical implementation of the schematic diagram shown in Figure 3.1, previously presented in Chapter 3.

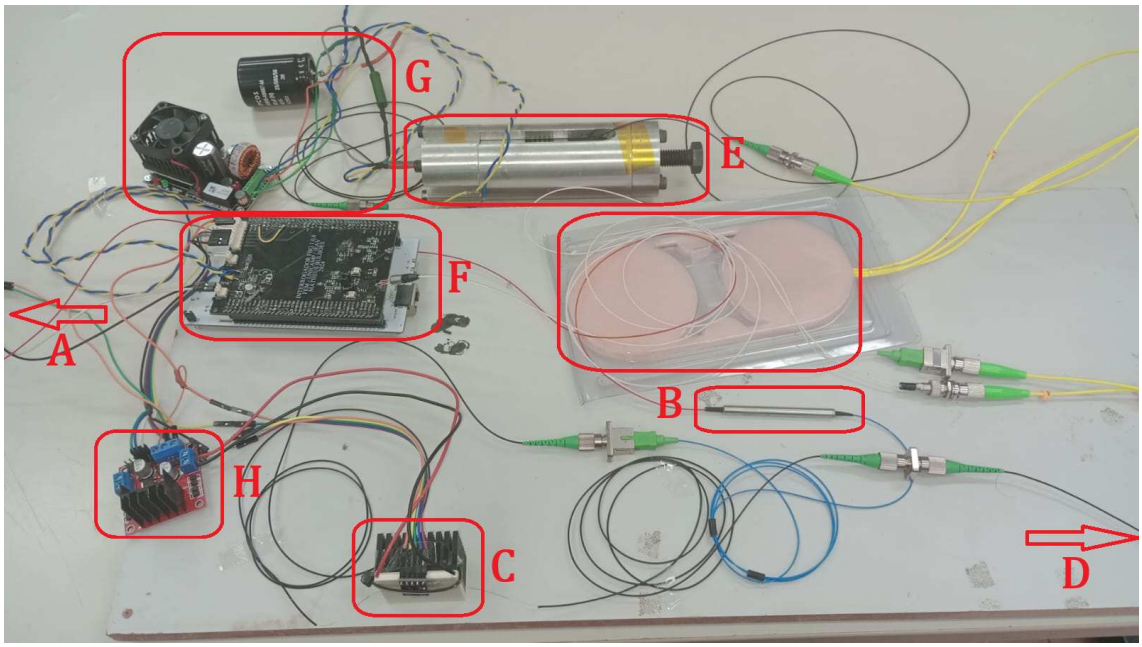

Figure 4.22 – Experimental setup containing the main components of the interrogator system: (A) optical and electronic input, (B) optical circulators, (C) reference FBG and peltier element, (D) sensing FBG array, (E) tunable FBG module, (F) piezo driver, (G) STM32 board and acquisition circuit board, (H) H-bridge peltier driver.

Although the current configuration supports interrogation of only a limited number of FBGs — due to the restricted tuning range of the FBG employed as the tunable filter — the system was tested using a single FBG, since multiple sensors with closely spaced Bragg wavelengths (within a 4 nm range) were not available. It is important to note, however, that the sweep range of the proposed interrogator can be extended by incorporating additional filter FBGs mounted on a single PZT actuator. This approach would require the use of optical filters and multiple photodetectors, one for each filter FBG, and its scheme is presented in Figure 4.23.

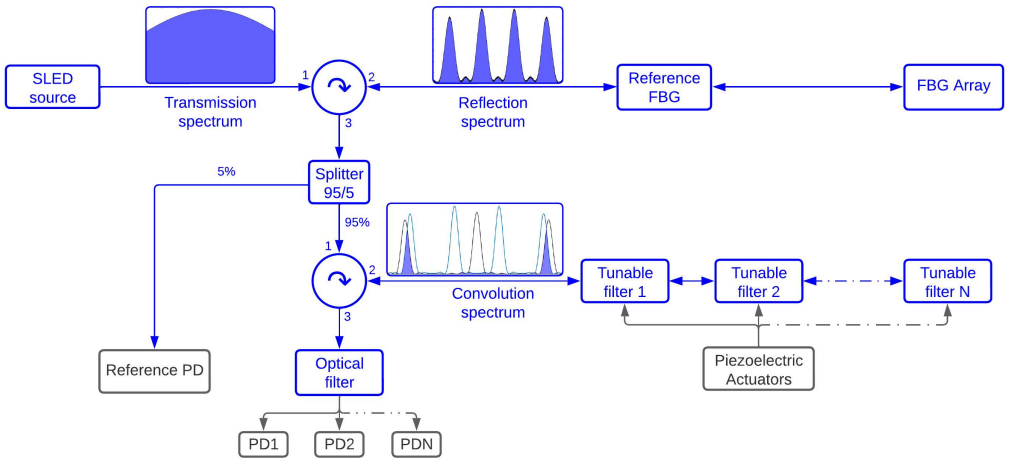

Figure 4.23 – Multiple filter FBG schematic.

4.3.1 Outlier Removal Algorithm

Initial tests of the interrogator revealed occasional outliers in the calculated Bragg wavelength measurements. Figure 4.24 shows the result of acquiring 10,000 data points at a sampling rate of 50 Hz, totaling 200 seconds of acquisition. In this test, the module composed by PZT actuador and a FBG was employed as the tunning device. These unexpected samples are believed to be outliers caused by the system missing the rising edge of the power convolution signal. When this happens, the comparator may incorrectly identify the intersection with the sensing FBG, and the algorithm assigns a wrong value for the Bragg wavelength. The exact reason behind this behavior is still under investigation. Nonetheless, it is important to highlight that these outliers represent only about 0.1% of the total calculated values. This observation led to the implementation of a filtering function to remove outliers in subsequent tests.

To mitigate the effect of these outliers, the microcontroller firmware was updated to discard values identified as outliers before transmission. The filtering algorithm evaluates whether the current measurement lies within a defined number of standard deviations from a sliding window of the last values. If the point falls within this range, it is accepted; otherwise, it is discarded and the previous valid measurement is retained. With this filtering implemented, a second test was performed under the same conditions. The results are shown in Figure 4.25.

4.3.2 Hysteresis Compensation Test

As discussed in Chapter 3, the tunable filter exhibits a hysteresis effect that causes the Bragg wavelength calculated during the increasing sweep of the control signal to differ from

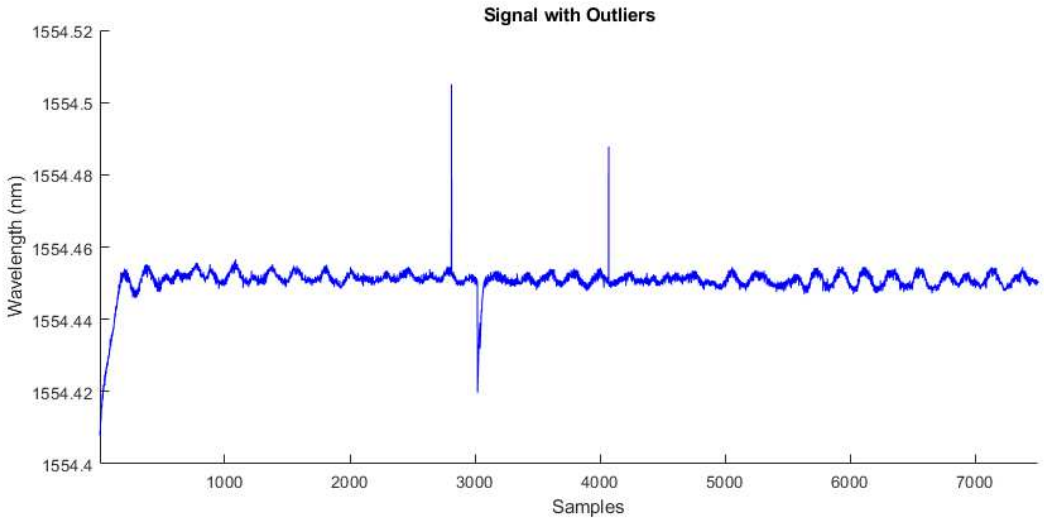

Figure 4.24 – Bragg wavelength signal with outliers.

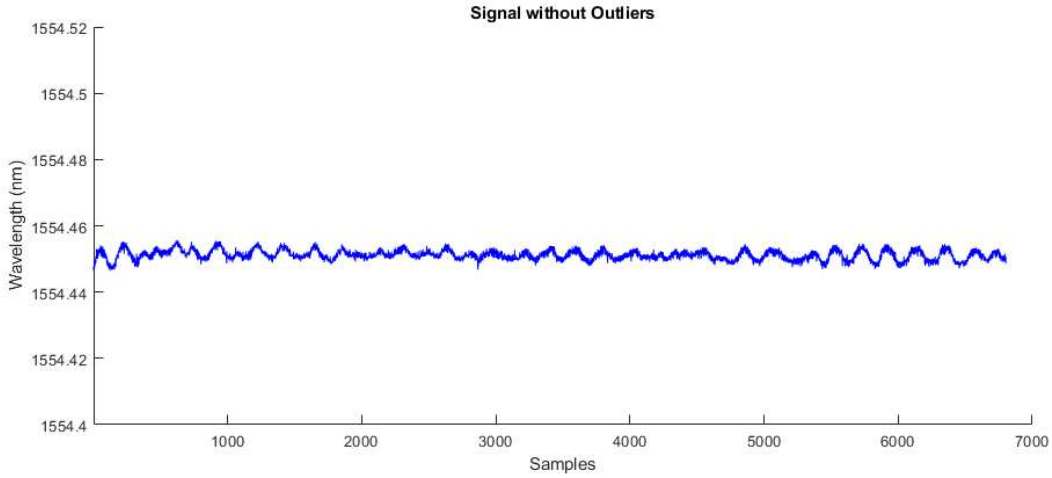

Figure 4.25 – Bragg wavelength filtered signal with no outliers.

that calculated during the decreasing sweep. To compensate for this behavior, a lookup table was implemented in the firmware.

Figure 4.26 shows the result of a test with the hysteresis compensation disabled. A noticeable offset (of approximately 550 pm) can be observed between the values acquired during the increasing and decreasing sweeps. This offset leads to inaccuracies in determining the true Bragg wavelength. To eliminate the difference between the measured values during the rising and falling sweeps, a hysteresis compensation algorithm was implemented, as described in Chapter 3. In contrast, Figure 4.27 shows the same test executed with the hysteresis compensation enabled. In this case, the curves corresponding to the increasing and decreasing sweeps are significantly more aligned.

Although the compensation significantly improved the alignment, a small difference

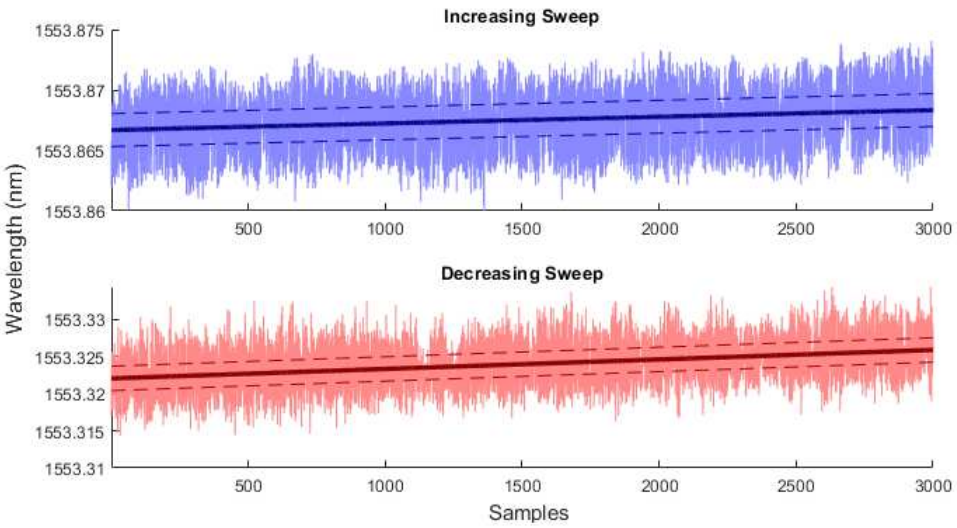

Figure 4.26 – Bragg wavelength acquisition without hysteresis compensation.

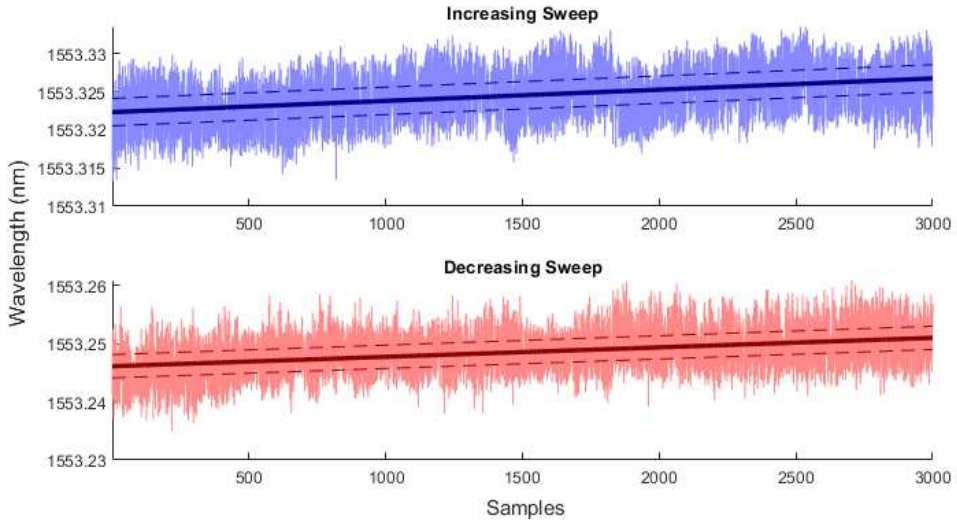

Figure 4.27 – Bragg wavelength acquisition with hysteresis compensation.

still remained between the Bragg wavelengths calculated during the two sweep directions. As a workaround, the average between the values from both sweeps was considered as the final Bragg wavelength.

4.3.3 Temperature compensation test

This test was designed to evaluate the effectiveness of the temperature compensation strategy implemented in the interrogator. As explained in Chapter 3, the system uses a reference FBG to estimate temperature-induced wavelength drifts in the tunable filter and subtracts them from the measurement of the sensing FBG. To test its performance, thermal disturbances were applied directly to the filter FBG using a hot air blower, with the Bragg wavelength of the

sensing FBG monitored over time. The tests were performed with the compensator turned off and on, and for the enabled cases, different cutoff frequencies were applied in the low-pass filter used to compute the temperature offset.

In the first experiment, a step-like disturbance was applied. The hot air blower was turned on and directed at the tunable FBG for a few seconds, then turned off. Figure 4.28 shows the behavior of the sensing FBG when no temperature compensation is applied. The Bragg wavelength visibly drops due to thermal expansion of the tunable grating and only stabilizes after the temperature returns to ambient levels. In this test, for a temperature variation of around 30 °C, the total wavelength shift was approximately 350 pm.

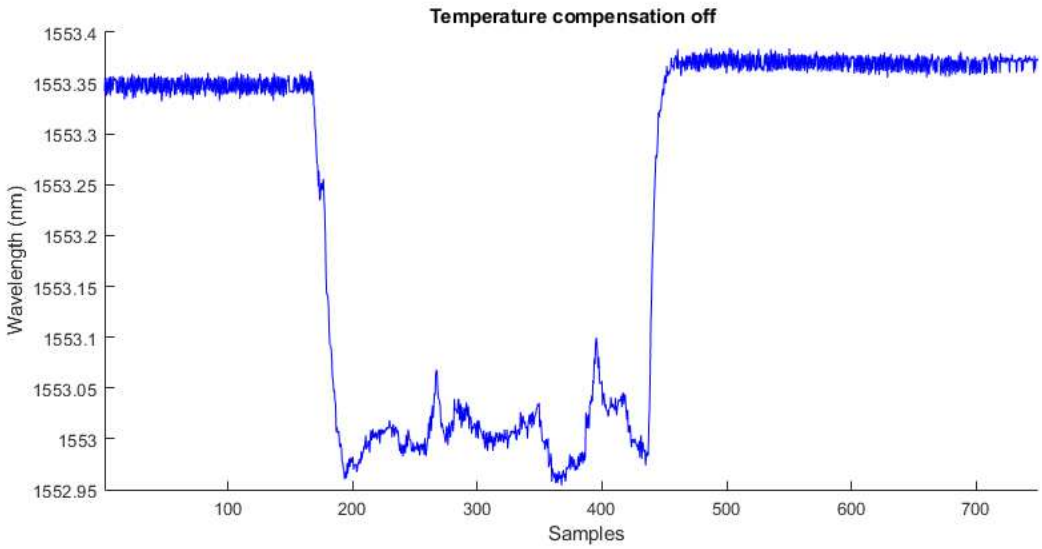

Figure 4.28 – Temperature compensation disabled.

When the compensation algorithm is enabled, the offset is subtracted from the measured values, and the system attempts to maintain the Bragg wavelength of the sensing FBG constant. Figure 4.29 shows the result for a 0.3 Hz filter applied to the offset signal. The compensation clearly improves the result, although high-frequency transient variations remain.

Figures 4.30 to 4.32 show the results for different filter bandwidths applied to the offset signal. The 1 Hz and 3.5 Hz filters introduce faster compensation, but also result in more transient distortion. Without filtering, the offset correction is instantaneous, but noise and high-frequency components are amplified.

A second experiment was conducted to test the compensation under slow thermal variation. In this test, the blower was initially turned on, then gradually cooled down, and later heated again before being removed. Figure 4.33 shows the sensing FBG response with

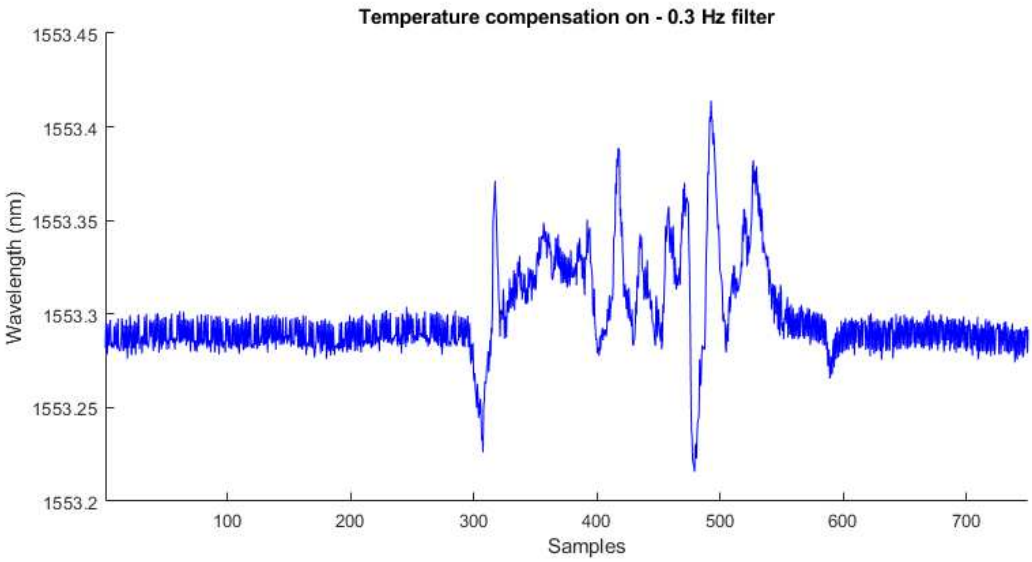

Figure 4.29 – Temperature compensation enabled with 0.3 Hz filtering.

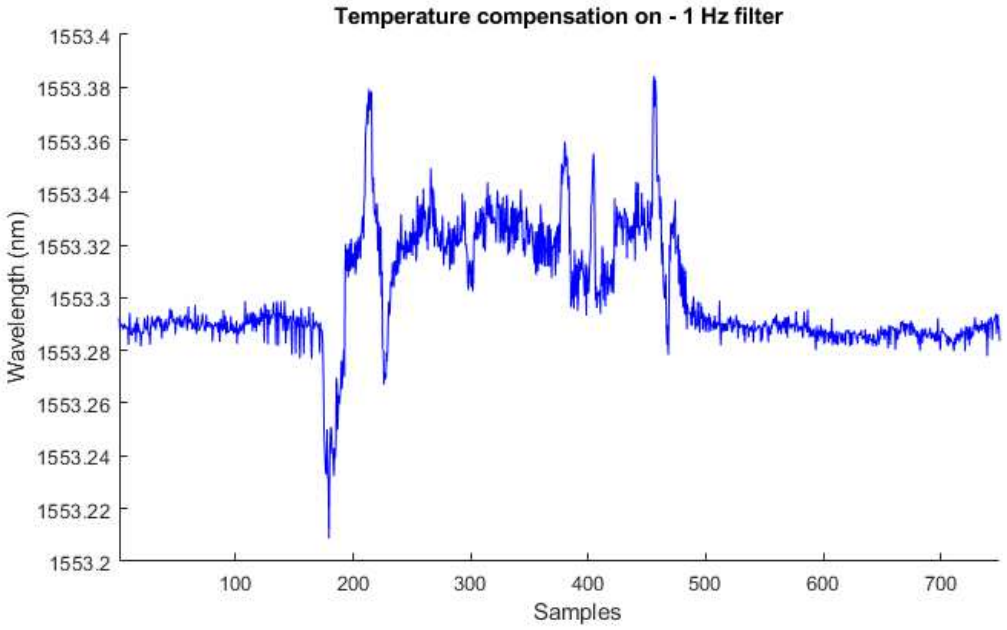

Figure 4.30 – Temperature compensation with 1 Hz filter.

compensation turned off. The Bragg wavelength tracks the thermal drift closely, confirming the tunable FBG's sensitivity to temperature.

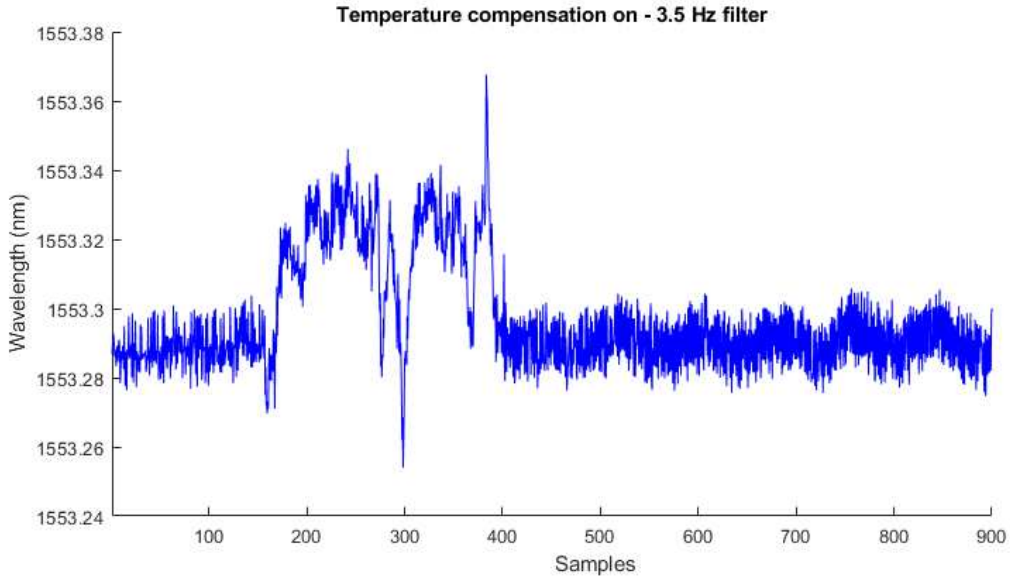

Figure 4.31 – Temperature compensation with 3.5 Hz filter.

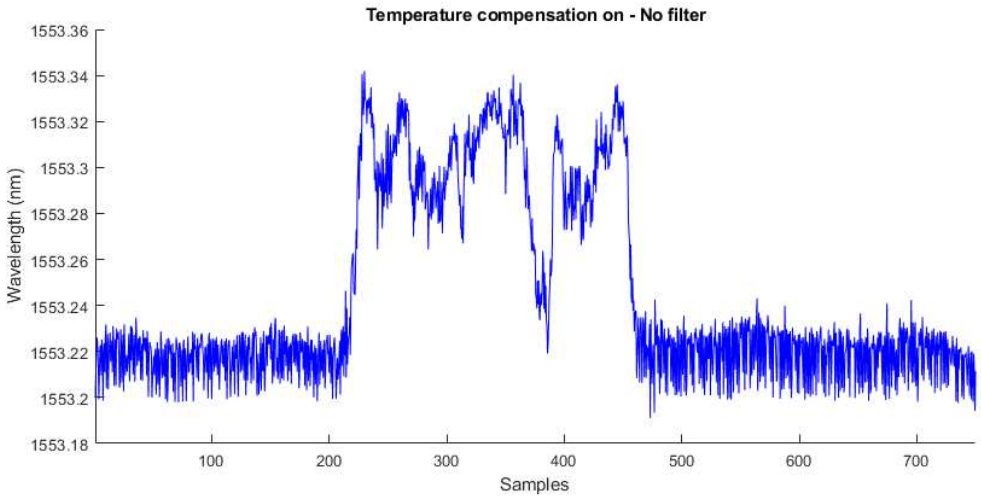

Figure 4.32 – Temperature compensation without filtering.

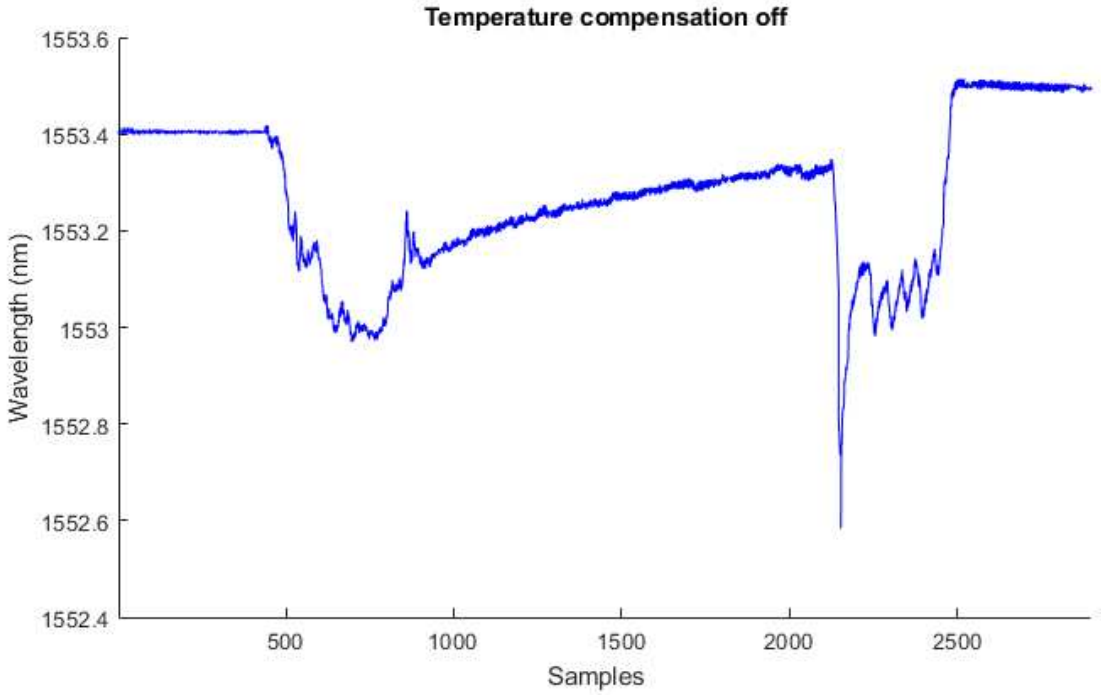

With compensation enabled, Figures 4.34 and 4.35 demonstrate significant suppression of the thermal drift when using 0.3 Hz and 1 Hz filters respectively. Both filter values showed good stability, but the 0.3 Hz filter also delays the compensation response slightly.

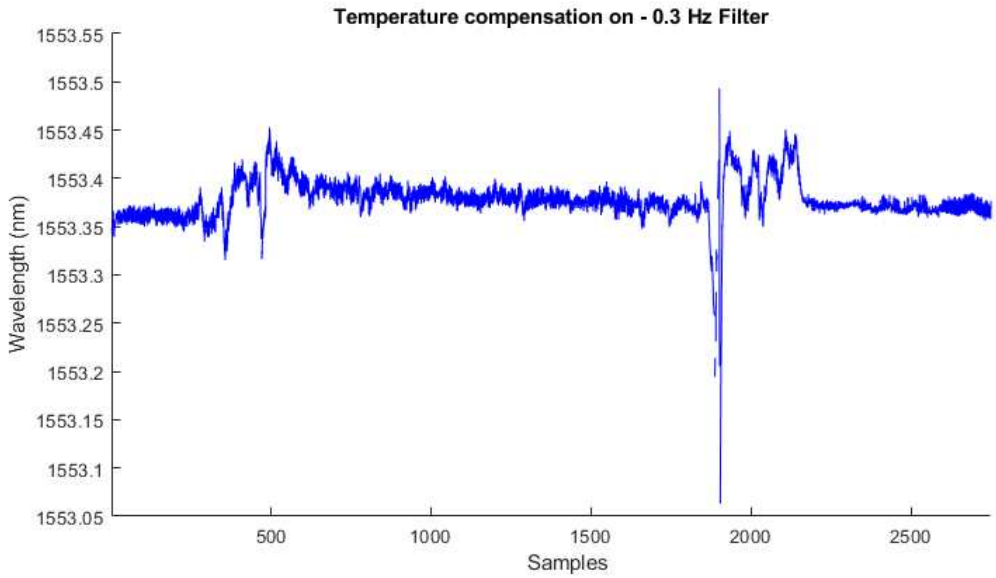

Figure 4.34 – Temperature compensation enabled with 0.3 Hz filter under slow thermal variation.

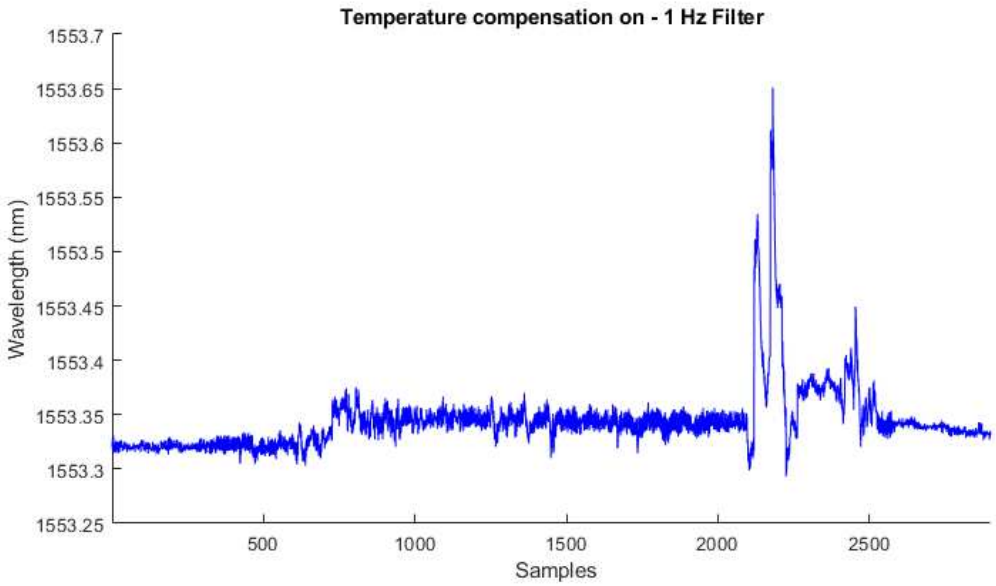

Figure 4.35 – Temperature compensation enabled with 1 Hz filter under slow thermal variation.

These results confirm that the implemented temperature compensation strategy, using a reference FBG and low-pass filtered offset correction, effectively mitigates low-frequency thermal disturbances in the interrogator. In practice, since the filter FBG will be located in-

side the interrogator enclosure, only slow temperature variations are expected, which are well compensated by the proposed method.

4.3.4 Final results using tunable FBG

After applying all compensation mechanisms and signal filtering strategies, the interrogator was able to track the Bragg wavelength of the sensing FBG with good stability. The final dataset was acquired with the system fully operational, including outlier removal, hysteresis compensation, and temperature compensation, as described in the previous sections.

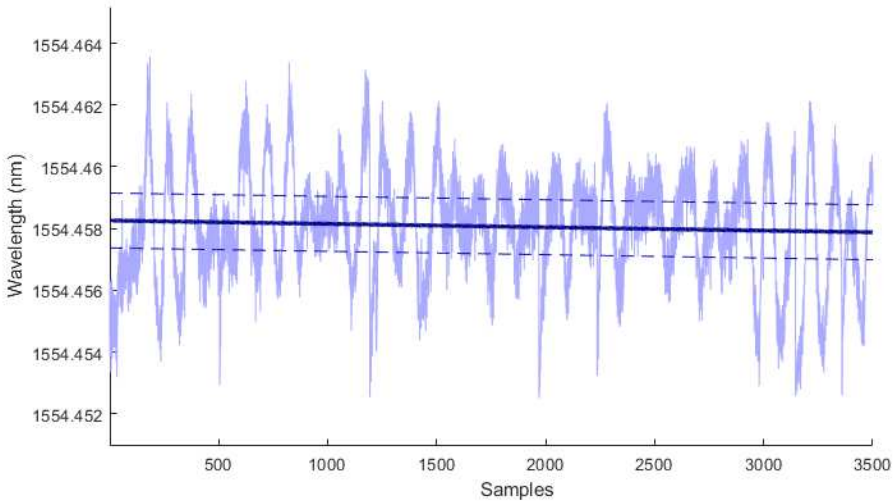

Figure 4.36 – Bragg wavelength values in final acquisition test using FBG as tunable filter.

Figure 4.36 shows the calculated Bragg wavelength values over time for the final acquisition. In this test, the filter FBG was kept on a laboratory bench, being exposed only to small ambient temperature fluctuations. The standard deviation of this signal was calculated to estimate the resolution of the interrogator.

The calculated standard deviation of the interrogator was around 1.5 pm. While this does not meet the 1 pm desired in the best scenario, the result is promising and shows that the methodology is robust. Moreover, this value is comparable to those achieved by high-performance commercial interrogators currently available. With further refinement, the target resolution is likely achievable in future iterations of the interrogator.

Figure 4.37 shows a screenshot of the LabVIEW graphical interface used to visualize the Bragg wavelength of the sensing FBG in real time. The interface continuously plots the calculated Bragg wavelength, as already mentioned in Chapter 3.

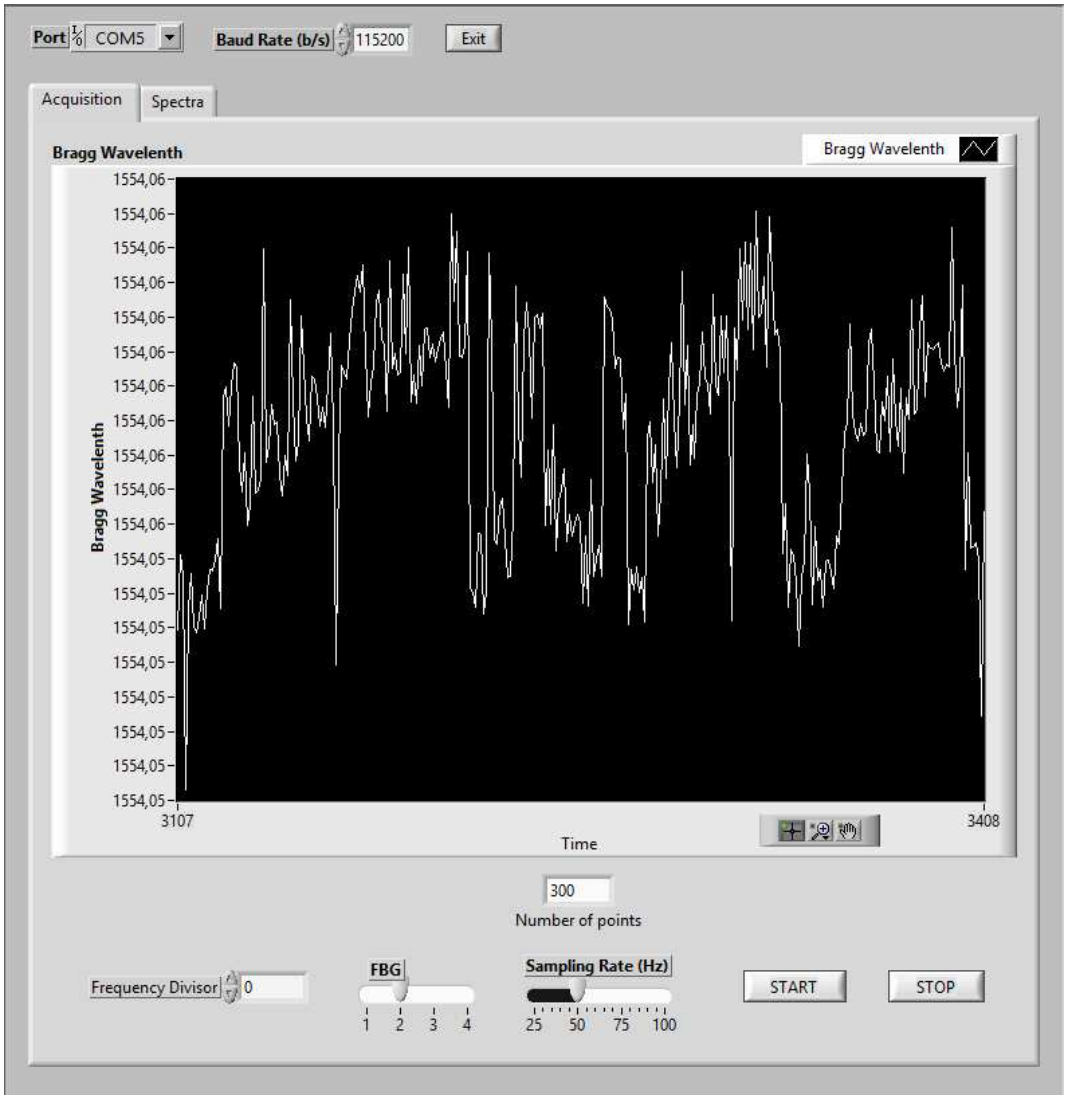

Figure 4.37 – LabVIEW interface showing real-time Bragg wavelength values.

These results validate the operation of the interrogation method and provide a solid basis for future improvements aimed at increasing the sweeping rate, accuracy, or sweeping range, thereby enabling the interrogation of larger FBG arrays.

4.3.5 Final Results Using Fabry-Perot Filter

Next, we present the test using the Fabry-Perot as the tunable filter. The interrogation system was evaluated with an array of FBGs and successfully computed the Bragg wavelength of all gratings simultaneously. Although the current LabVIEW interface displays only one wavelength at a time, the backend supports multi-FBG interrogation, and the interface could be easily adapted to present multiple readings in parallel.

To estimate the Bragg wavelength using the Fabry-Perot filter as a tunable element,

two methods were evaluated: polynomial interpolation and mean-based estimation. In all experiments, the sweeping range of the tunable filter was approximately 40 nm. This range can be extended up to 100 nm by applying a differential signal to the actuator at its maximum rated voltage, as specified in the datasheet.

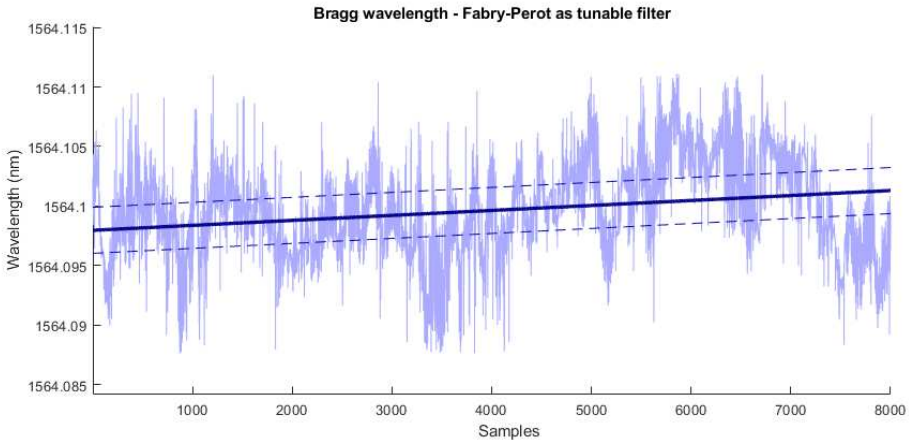

Figure 4.38 – Bragg wavelength estimation using polynomial interpolation method.

Initial tests with sweeping frequency of 50 Hz using second-order polynomial fitting (Figure 4.38) yielded good resolution, reaching a standard deviation of approximately 4 pm. However, as the scan frequency increased, the number of sampling points per scan decreased, and the presence of noise made the local curve fitting diverge significantly from the expected FBG spectrum, and, consequently, the calculated wavelength differed significantly. In addition, the execution time for calculating each value increased. Due to these limitations, the mean-based method was adopted as an alternative.

In this strategy, all Fabry-Perot central wavelength samples are averaged to estimate the Bragg wavelength of the sensor FBG. This approach was tested with scan frequencies of 50 Hz, 100 Hz, 200 Hz, and 500 Hz. In all cases, the resolution — evaluated as the standard deviation of the Bragg wavelength — remained between 10 pm and 15 pm. Figure 4.39 through Figure 4.42 show the data obtained at each frequency.

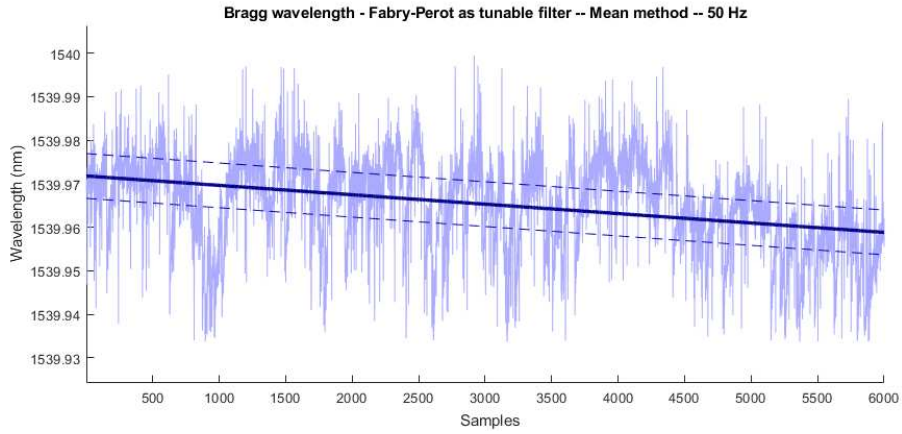

Figure 4.39 – Bragg wavelength estimation using Fabry-Perot filter at 50 Hz with mean method.

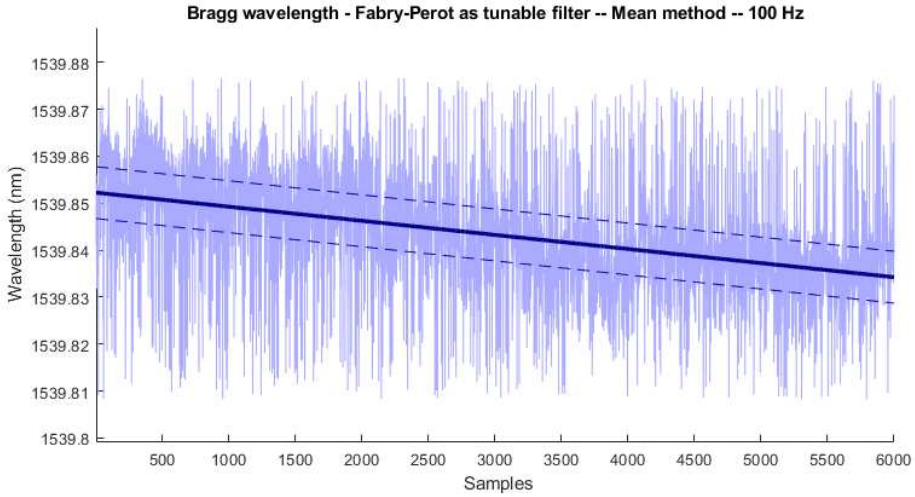

Figure 4.40 – Bragg wavelength estimation using Fabry-Perot filter at 100 Hz with mean method.

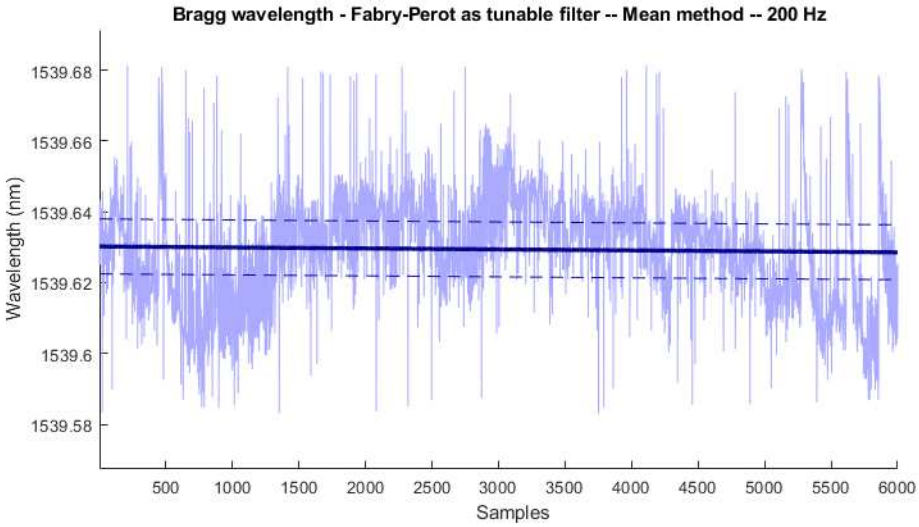

Figure 4.41 – Bragg wavelength estimation using Fabry-Perot filter at 200 Hz with mean method.

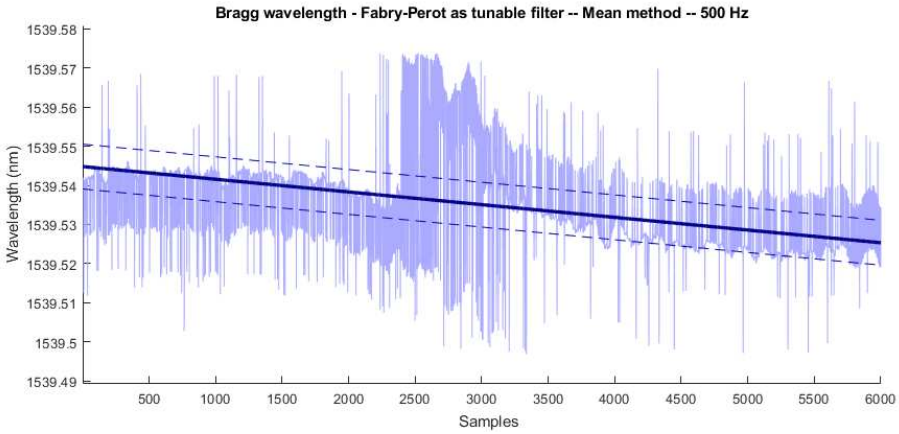

Figure 4.42 – Bragg wavelength estimation using Fabry-Perot filter at 500 Hz with mean method.

As the scan frequency increases, the signal becomes noisier and shows sharper deviations. This behavior is a consequence of the reduced number of entries in the lookup table (explained in Chapter 3) used to relate DAC values to the center wavelength of the Fabry-Perot filter. At higher frequencies, fewer points are available per scan cycle, increasing the spacing between adjacent wavelength values. This reduces the effective resolution of the actuator and amplifies quantization effects in the Bragg wavelength estimation.

Additionally, a practical upper limit around 500 Hz was identified for this interrogation approach. Beyond this frequency, the time required to process the signal and compute each Bragg wavelength can exceed the time interval between the reflections of two FBGs spaced by 10 nm, due to the faster scan rate. As a result, the system may fail to detect some peaks and generate delayed responses, compromising real-time operation and accuracy.

5 FINAL CONSIDERATIONS

In conclusion, this study aimed to design, develop, and evaluate an interrogation system for Fiber Bragg Grating (FBG) sensor arrays using the twin-grating technique and a tunable Fabry-Perot filter. Theoretical analysis showed that the proposed technique has the potential to achieve a maximum wavelength excursion of approximately 4.8 nm when using a tunable FBG, and up to 100 nm when using a tunable Fabry-Perot filter. Simulations performed in MATLAB, which incorporated estimated optical and electronic acquisition noise, confirmed the robustness of the proposed signal processing algorithms and indicated that the system has the potential to achieve a resolution better than 0.15 pm.

From an experimental standpoint, several aspects of the system were validated. The real-time firmware was successfully deployed on a microcontroller, utilizing its internal hardware modules — such as timers, interrupts, and DMA — to achieve synchronization and implement a high-performance interrogator. This approach enabled features typically implemented on FPGAs, whose development is more expensive and complex, thereby resulting in a more practical and maintainable solution. The system demonstrated the ability to detect Bragg wavelength variations with a measured resolution of approximately 1.5 pm using the FBG as the tunable filter, and supported sweeping rates up to 500 Hz when using the Fabry-Perot filter. Tests also validated the effectiveness of the implemented hysteresis compensation and thermal compensation mechanisms, as well as the outlier filtering algorithm.

Below, we summarize the planned objectives that were successfully achieved in this project, followed by an outline of potential future work to further advance the project.

Achieved Objectives

1. An in-depth comprehension of interrogation techniques for FBGs was acquired, laying the foundation for the subsequent development phases;

2. A tunable Bragg Grating filter module employing a piezoelectric actuator was designed, constructed, and characterized;

3. The optical circuit of the interrogator was designed;

4. Algorithms were successfully implemented to facilitate the acquisition, filtering, and processing of data from FBG sensor arrays;
5. Thermal compensation techniques were developed and implemented;
6. An experimental comparative analysis of the interrogator using FBG-based tunable filter and Fabry-Perot filter was conducted;
7. The design of an electronic circuit for the interrogator was executed, ensuring the integration of electronic components for the system operation;
8. A comprehensive sensor noise model, encompassing main optical and electronic noises, was developed, contributing to the understanding and mitigation of potential sources of noise;
9. A LabVIEW program was developed for interfacing with the interrogator;
10. The performance of the developed interrogator was experimentally evaluated.

Future work

1. Incorporate the capability to perform FBG characterization via deconvolution of the signal obtained from the sensor-grating scan by the filter-grating;
2. Experimentally validate the conducted noise analysis;
3. Investigate low-cost actuators for implementation of the tunable filter;
4. Develop new interrogation techniques capable of operating at rates above 1 kHz.

Among the proposed future directions, particular attention should be given to the development of low-cost actuators for the tunable filter and to the creation of new interrogation techniques capable of operating above 1 kHz. The development of a low-cost actuator would enable the design of interrogation systems with substantially reduced cost compared to those currently found in the literature, thereby broadening the range of applications where FBG sensors can be viably adopted. On the other hand, interrogation techniques capable of operating at kilohertz-level rates would address the needs of high-speed dynamic sensing applications, such as vibration monitoring or real-time structural health assessment. These future researches

can yield significant contributions to the literature: the development of low-cost FBG array interrogators and high-frequency, high-resolution FBG array interrogators.

BIBLIOGRAPHY

Buck, J. A.; Jacobs, I. Fundamentals of Optical Fibers . **Physics Today**, 1996.

Dai, S.; Chen, G. Y.; Yang, Q.; Jin, G.; Wu, Z.; Ning, Y.; Liu, T. A Low-Power-Consumption FBG Sensor Interrogator. **Proceedings - 2022 3rd International Conference on Electronics, Communications and Information Technology, CECIT 2022**, p. 242–246, 2022.

Damjanovic, D. Hysteresis in Piezoelectric and Ferroelectric Materials. In: **The Science of Hysteresis**. [S.l.: s.n.], 2006. ISBN 9780124808744.

Dante, A. **Módulo sensor óptico com grades de Bragg em fibra óptica e cerâmicas piezoelétricas para medida de alta tensão com transformadores de potencial**. Tese (Doutorado) — Universidade Estadual de Campinas, 2016.

Díaz, C. A.; Leitão, C.; Marques, C. A.; Domingues, M. F.; Alberto, N.; Pontes, M. J.; Frizera, A.; Ribeiro, M. R.; André, P. S.; Antunes, P. F. Low-cost interrogation technique for dynamic measurements with fbg-based devices. **Sensors (Switzerland)**, v. 17, 2017.

Elaskar, J.; Luda, M.; Codnia, J.; Oton, C. J. High-speed FBG interrogator based on fiber interferometry and FPGA real-time processing. In: **2021 IEEE Photonics Conference, IPC 2021 - Proceedings**. [S.l.: s.n.], 2021. ISBN 9781665416016.

Fernández, M. P.; Rossini, L. A. B.; Cruz, J. L.; Andrés, M. V.; Caso, P. A. C. High-speed and high-resolution interrogation of fbg sensors using wavelength-to-time mapping and gaussian filters. **Optics Express**, v. 27, 2019.

Fracarolli, J. P.; Argentato, M. C.; Costa, E. F.; Nogueira, J. R.; Melo, A. G.; Benetti, D. FBG interrogator based on two-stage digital PI controller for high-frequency signals. In: **2019 SBMO/IEEE MTT-S International Microwave and Optoelectronics Conference, IMOC 2019**. [S.l.: s.n.], 2019. ISBN 9781728130996.

Guo, G.; Pankow, M.; Peters, K. High-speed interrogation approach for fbg sensors using a vcsel array swept source. **IEEE Sensors Journal**, v. 19, 2019.

Hegde, G.; Asokan, S.; Hegde, G. Fiber Bragg grating sensors for aerospace applications: a review. **ISSS Journal of Micro and Smart Systems**, 2022.

Heywang, W.; Lubitz, K.; Wersing, W. Piezoelectricity - Evolution and Future of a Technology. **Springer Series in Materials Science**, 2008.

Hill, K. O.; Fujii, Y.; Johnson, D. C.; Kawasaki, B. S. Photosensitivity in optical fiber waveguides: Application to reflection filter fabrication. **Applied Physics Letters**, v. 32, n. 10, p. 647–649, 1978.

Hill, K. O.; Malo, B.; Bilodeau, F.; Johnson, D. C.; Albert, J. Bragg gratings fabricated in monomode photosensitive optical fiber by UV exposure through a phase mask. **Applied Physics Letters**, v. 62, n. 10, p. 1035–1037, 1993.

Hill, K. O.; Meltz, G. Fiber Bragg grating technology fundamentals and overview. **Journal of Lightwave Technology**, 1997.

Inphenix. **IPSDS1509 SLD Light Source Module**. 2023. <https://www.inphenix.com/pro/Superluminescent%20Diodes%20Module/IPSDS1509.pdf>. Product specification, Rev. 1.1.

Jeong, S. Y.; Choi, S. J.; Pan, J. K. An implementation of fbg interrogator with a tunable fabry-perot filter. In: **Optics InfoBase Conference Papers**. [S.l.: s.n.], 2017. ISSN 21622701.

Ji, Y.; Chung, Y.; Sprinzak, D.; Heiblum, M.; Mahalu, D.; Shtrikman, H. An electronic Mach-Zehnder interferometer. **Nature**, 2003.

Lei, M.; Zou, W.; Li, X.; Chen, J. Ultrafast FBG Interrogator Based on Time-Stretch Method. **IEEE Photonics Technology Letters**, 2016.

Luna. **FFP-TF/TF2 Fiber Fabry-Perot Tunable Filter**. 2020. <https://lunainc.com/sites/default/files/assets/files/resource-library/LUNA-Data-Sheet-Micron-FFP_TF_TF2-v3.pdf>.

Marin, Y. E.; Celik, A.; Faralli, S.; Adelmini, L.; Kopp, C.; Pasquale, F. D.; Oton, C. J. Integrated Dynamic Wavelength Division Multiplexed FBG Sensor Interrogator on a Silicon Photonic Chip. **Journal of Lightwave Technology**, 2019.

Marin, Y. E.; Nannipieri, T.; Oton, C. J.; Pasquale, F. D. Integrated FBG Sensors Interrogation Using Active Phase Demodulation on a Silicon Photonic Platform. **Journal of Lightwave Technology**, 2017.

Meltz, G.; Morey, W. W.; Glenn, W. H. Formation of Bragg gratings in optical fibers by a transverse holographic method. **Optics Letters**, 1989.

Milne, J. S.; Dell, J. M.; Keating, A. J.; Faraone, L. Widely tunable MEMS-based fabry - Perot filter. **Journal of Microelectromechanical Systems**, 2009.

NXP. **LM75A Digital temperature sensor and thermal watchdog**. 2007. <https://br.mouser.com/datasheet/2/302/LM75A-3137821.pdf>. Datasheet.

Ostertagová, E. Modelling using polynomial regression. In: **Procedia Engineering**. [S.l.: s.n.], 2012. ISSN 18777058.

Othonos, A.; Kalli, K.; Pureur, D.; Mugnier, A. Fibre Bragg gratings. **Springer Series in Optical Sciences**, 2006.

Panda, P. K.; Sahoo, B. PZT to lead free piezo ceramics: A review. **Ferroelectrics**, 2015.

Pereira, L.; Min, R.; Woyessa, G.; Bang, O.; Marques, C.; Varum, H.; Antunes, P. Interrogation method with temperature compensation using ultra-short fiber bragg gratings in silica and polymer optical fibers as edge filters. **Sensors**, v. 23, 2023.

PiezoDrive. **MX200 V10 200V 1A Piezo Driver**. 2021. <https://www.piezodrive.com/wp-content/uploads/2021/03/MX200-V10-Datasheet-R4.pdf>. Datasheet.

Rohan, R.; Venkadeshwaran, K.; Ranjan, P. Recent advancements of fiber Bragg grating sensors in biomedical application: a review. **Journal of Optics (India)**, 2023.

Sadot, D.; Boimovich, E. Tunable optical filters for dense WDM networks. **IEEE Communications Magazine**, 1998.

Sahota, J. K.; Gupta, N.; Dhawan, D. Fiber Bragg grating sensors for monitoring of physical parameters: a comprehensive review. **Optical Engineering**, 2020.

STM Microelectronics. **RM0433 Reference manual**. 2023. <https://www.st.com/resource/en/reference_manual/dm00314099-stm32h742-stm32h743-753-and-stm32h750-value-line-advanced-arm-based-32-bit-mcus-stmicroelectronics.pdf>.

Texas Instruments. **OPA356, 2356: 200MHz, Video CMOS Operational Amplifier**. 2001. <https://www.ti.com/lit/ds/symlink/opa356.pdf>. Datasheet (Rev. A).

Thorlabs. **FABRY-PEROT INTERFEROMETER TUTORIAL**. 2024. <https://www.thorlabs.com/newgrouppage9_pf.cfm?guide=10&category_id=&objectgroup_id=9021>. Accessed: 2024.

Tkachenko, A. Y.; Lobach, I. A.; Guskov, L. N. Fiber sensor interrogator based on self-sweeping fiber laser. p. 348–351, 2016.

Tosi, D. Advanced interrogation of fiber-optic bragg grating and fabry-perot sensors with klt analysis. **Sensors (Switzerland)**, v. 15, 2015.

Tosi, D. **Review and analysis of peak tracking techniques for fiber bragg grating sensors**. 2017.

Wilson, J.; Hawkes, J. F. B.; Faris, J. J. Optoelectronics: An Introduction . **American Journal of Physics**, 1984.

Wu, Q.; Semenova, Y.; Sun, A.; Wang, P.; Farrell, G. High resolution temperature insensitive interrogation technique for FBG sensors. **Optics and Laser Technology**, v. 42, n. 4, p. 653–656, 2010.

Xiaolin, T.; Yong, W.; Qiang, Z.; Yunzhou, L.; Huanxin, L.; Jiaojiao, Q.; Dongbin, Z. A miniaturized, low-cost and portable fiber bragg grating interrogation system for remote monitoring. **Optik**, v. 248, 2021.

Yao, K.; Zhu, W.; Uchino, K.; Zhang, Z.; Lim, L. C. Design and fabrication of a high performance multilayer piezoelectric actuator with bending deformation. **IEEE Transactions on Ultrasonics, Ferroelectrics, and Frequency Control**, 1999.

Zhang, X.; Niu, H.; Hou, C.; Di, F. An edge-filter fbg interrogation approach based on tunable fabry-perot filter for strain measurement of planetary gearbox. **Optical Fiber Technology**, v. 60, 2020.

Appendix

APPENDIX A – MATLAB INTERROGATOR ALGORITHM SIMULATION CODES

A.1 Main algorithm

```
clear
clc
close all

%Pseudo-continous period
T = 1e-6;

%Discrete period
Td = 0.02;

%Wavelength Limits
ws = 1549;
we = 1551;

%Noise values
noise_rms = 0.0005;

%Comp thresholds
pth = 0.2;
pth2 = pth + 0.1;
th = pth*3.3;
th2 = pth2*3.3;

%Polynomial degree
ni = 2;
```

```
%Bragg Wavelength
wb = 1550;

%
t = ws:T:we;
w = sinc((t-wb)*5)*3.2;

mult_noise = 500;

for j = 1:1
    a = noise_rms*mult_noise;
    snr = 20*log10(3.3/a);
    u = awgn(w, snr);

    %create discrete time
    td = ws:Td:we;
    sd = u(floor((td-ws)/T+1));

    wt = sd;

    flag = 0;
    ti = 0;
    tf = 0;
    for i = 1:length(wt)
        if(flag == 0)
            if(wt(i) < th2 && ti == 0)
                wt(i) = nan;
            elseif(ti == 0)
                ti = (i-1)*Td+ws;
                pi = i;
                flag = 1;
            end
```

```
        else
            if(wt(i) < th && tf == 0)
                tf = (i-2)*Td+ws;
                pf = i-1;
            elseif(tf ~= 0)
                wt(i-1) = nan;
            end
        end
    end
    wt = wt(pi:pf);

    n = ni;
    tt = ti:Td:tf;
    if(n >= length(tt))
       n = length(tt)-1;
    end
    [p, s, mu] = polyfit(tt, wt, n);

    tp = ti:T:tf;
    y = polyval(p, tp, s, mu);

    [m, index] = max(y);
    tmax = ti + index*T;
    error(j) = tmax - wb;
end

length(tt)
std = std(error)
e_max = max(error)

%% Plot
figure(1)
```

```
hold on
xlabel("Wavelength (nm)");
ylabel("Voltage (V)");
plot(t, u, 'c', 'linewidth', 1.5);
plot(t, w, 'm:', 'linewidth', 1.5);
plot(td, sd, 'ko');
plot(tt, wt, 'ro', 'linewidth', 1.5);
plot(tp, y, 'b', 'linewidth', 1.5);
plot(tmax, m, 'y*', 'linewidth', 2.5);
legend('Signal with noise', 'Original signal', 'Discretized
   signal','Post-Threshold signal', 'Polynomial fitting', '
   Curve peak')
```

A.2 Varying parameters and calculating resulting error

```
clear
clc
close all

% Pseudo-continous period
T = 1e-6;

% Number of points
N = 200;

% Wavelength Limits
ws = 1549.5; %nanometers
we = 1550.5; %nanometers

% Base noise value
noise_rms = 0.00035; %V
```

```
% Noise multiplier
mult_noise = 200;
%mult = linspace(1, 300, N); % Uncomment if simulating noise

% Discrete period
Td = 0.006;
%Tdk = linspace(0.001,0.05,N); % Uncomment if simulating period

% Comp thresholds
pth = 0.4;
%pthk = linspace(0.2,0.8,N); % Uncomment if simulating
   threshold

% Polynomial degree
ni = 2;
%nik = 2:8; % Uncomment if simulating poly degree

%Bragg Wavelength
wb = 1550; %nanometers

%Voltage
v = 3.3; %V

%
t = ws:T:we;

%
for k = 1:N % Replace for length(nik) if simulating poly degree

    % Uncomment which of these is being simulated
    %mult_noise = mult(k);
    %Td = Tdk(k);
```

```
%pth = pthk(k);
%ni = nik(k);

% Simulating
th = pth*3.3;
th2 = (pth+0.1)*3.3;
a = noise_rms*mult_noise;
snr = 20*log10(v/a);

for j = 1:20
    % Generating random Bragg Wavelenth
    wbVar = rand(1)/50-0.01; %varying 10 pm
    w = sinc((t-wb-wbVar)*5)*v;

    % Sum signal to noise
    u = awgn(w, snr);

    % Create discrete time
    td = ws:Td:we;
    sd = u(floor((td-ws)/T+1));

    wt = sd;

    flag = 0;
    ti = 0;
    tf = 0;
    for i = 1:length(wt)
        if(flag == 0)
            if(wt(i) < th2 && ti == 0)
                wt(i) = nan;
            elseif(ti == 0)
                ti = (i-1)*Td+ws;
```

```
                pi = i;
                flag = 1;
            end
        else
            if(wt(i) < th && tf == 0)
                tf = (i-2)*Td+ws;
                pf = i-1;
            elseif(tf ~= 0)
                wt(i-1) = nan;
            end
        end
    end
    wt = wt(pi:pf);

    n = ni;
    tt = ti:Td:tf;
    if(n >= length(tt))
       n = length(tt)-1;
    end
    [p, s, mu] = polyfit(tt, wt, n);

    tp = ti:T:tf;
    y = polyval(p, tp, s, mu);

    [m, index] = max(y);
    tmax = ti + index*T;
    error(j) = tmax - wb - wbVar;
end
k

std_d(k) = std(error);
e_med(k) = mean(abs(error));
```

```
    e_max(k) = max(abs(error));
end

%% Plotting results
figure(1)
hold on

% var = mult;
% xlabel('Noise Multiplier');
% xaxis(1,300);

% var = Tdk*1000;
% xlabel('Discretization Period (picometers)');
% xaxis(1,50);

% var = pthk*100;
% xlabel('Lower Threshold (%)');
% xaxis(20,80);

% var = nik;
% xlabel('Polynomial Degree');
% xaxis(2,8);

plot(var, std_d*1000, 'linewidth', 1.5);
plot(var, e_med*1000, 'linewidth', 1.5);
plot(var, e_max*1000, 'linewidth', 1.5);
grid;
ylabel('Wavelenth Error (picometers)');
legend('error standard deviation', 'average error', 'maximum
   error')
```

APPENDIX B – PCB PROJECT

The electronic acquisition and control circuit of the interrogator was developed using Altium Designer. The schematic was divided into functional blocks, each dedicated to a specific stage of the signal acquisition or generation process, ensuring modularity and clarity.

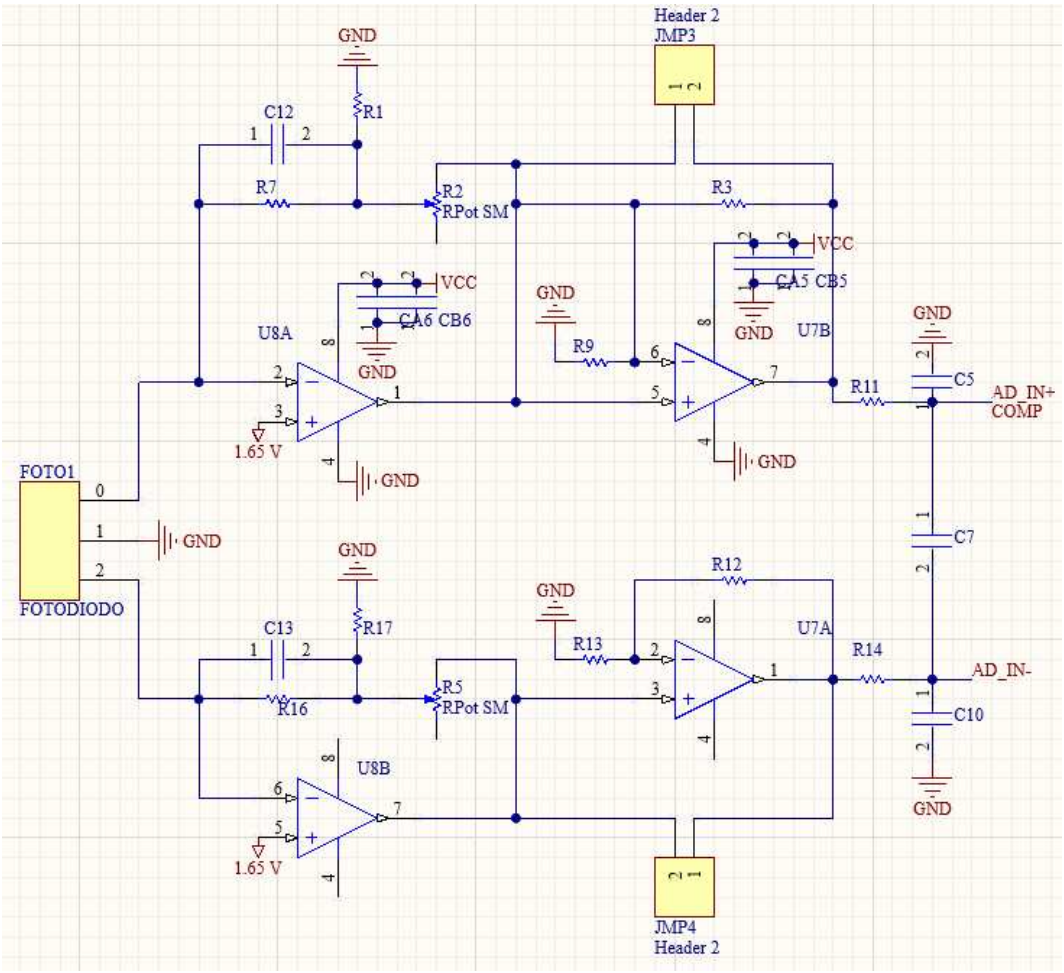

Figure B.1 – Altium Schematic - Main Transimpedance Amplifier circuit.

The first block (Figure B.1) presents the main transimpedance amplifier stage, responsible for converting the photocurrent from the convolution between the sensor FBGs and the tunable grating into voltage. A T-network with a trimpot is employed in the feedback path of each operational amplifier, allowing the adjustment of higher gains without having to use high resistor values, which would increase electronic noise. This stage also includes a cascaded amplifier for further gain increase, although in the current implementation, only the first stage is actively used.

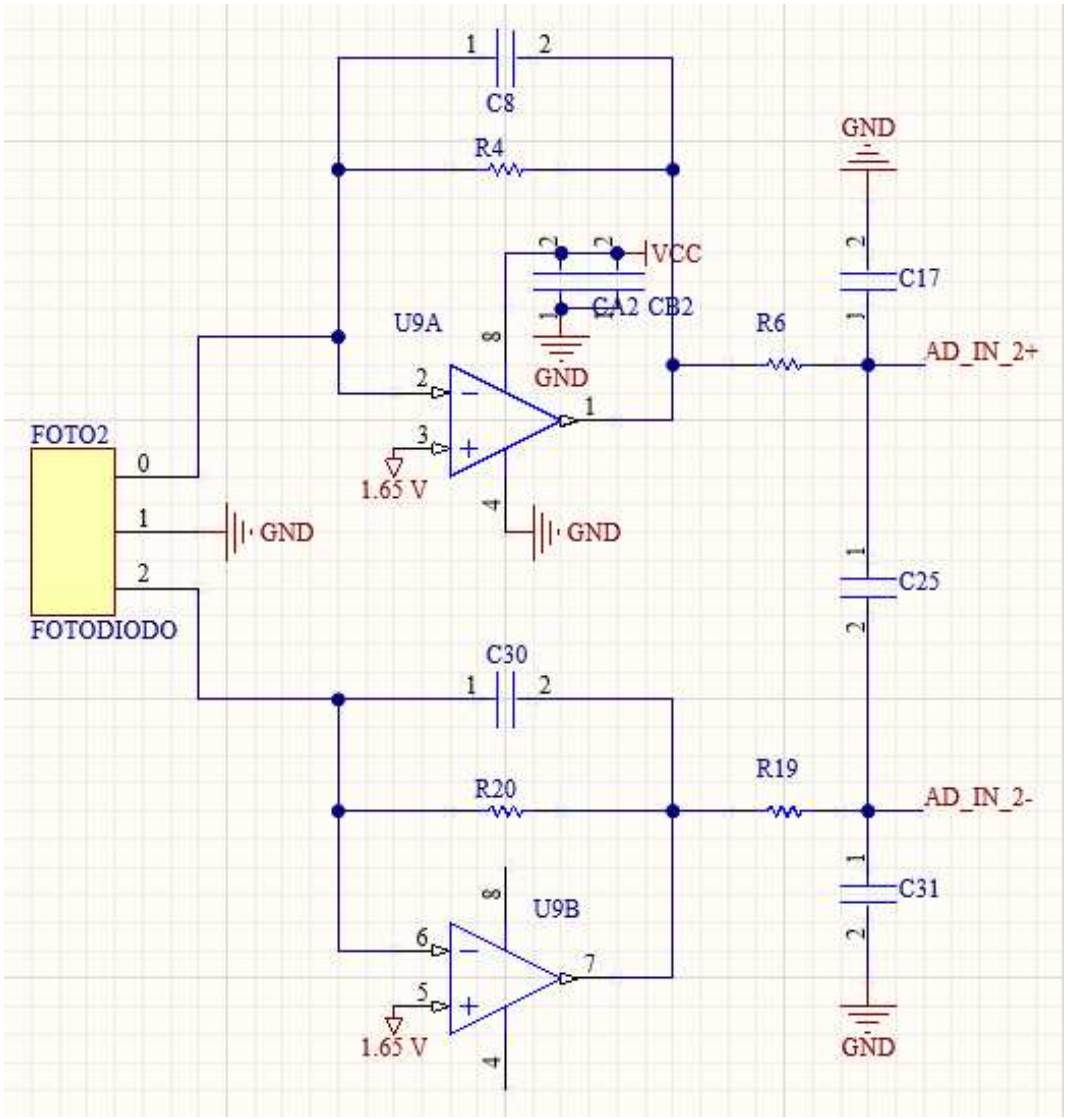

Figure B.2 – Altium Schematic - Reference Transimpedance Amplifier circuit.

The second transimpedance amplifier circuit (Figure B.2) is intended to receive the optical power from the reference source, providing data for dynamic compensation of source fluctuations. Although this compensation has not been implemented yet, the circuit was included for future scalability.

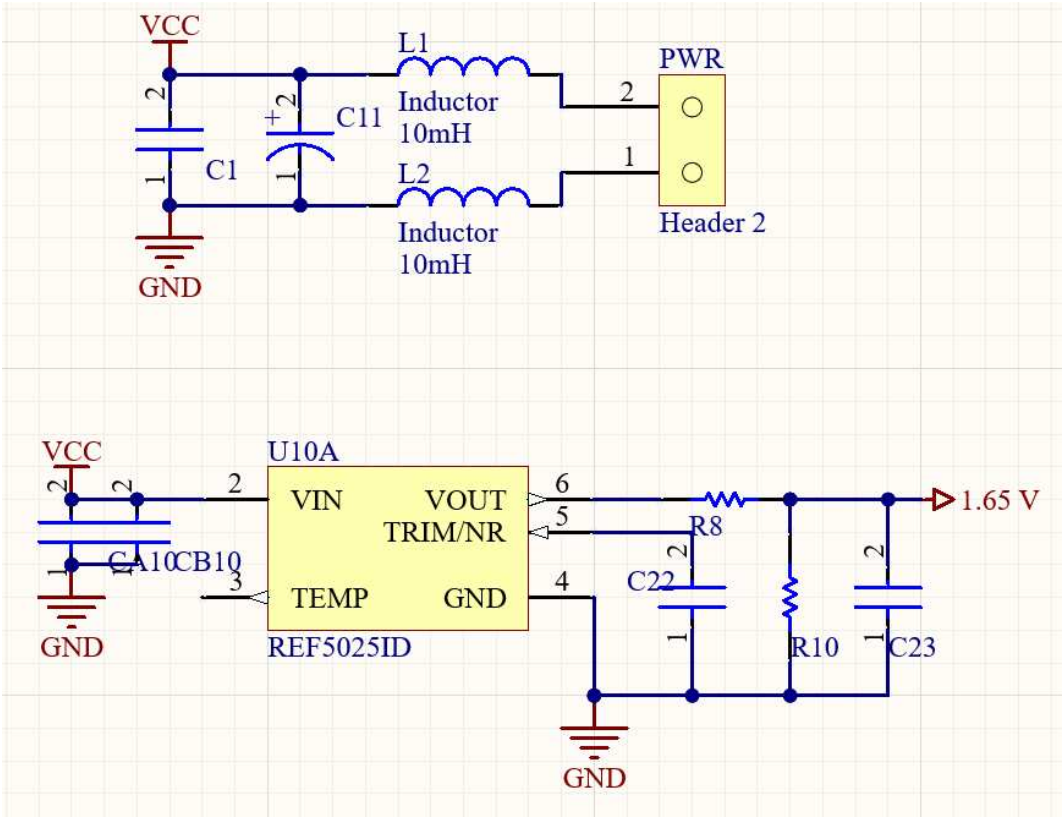

Figure B.3 – Altium Schematic - Power Supply and Voltage Reference circuits.

The power supply block (Figure B.4) includes inductors and bypass capacitors to suppress noise from the input power line. A voltage reference (REF5025) and a voltage divider generate a mid-supply reference voltage of 1.65,V, used as the reference voltage in the transimpedance amplifiers.

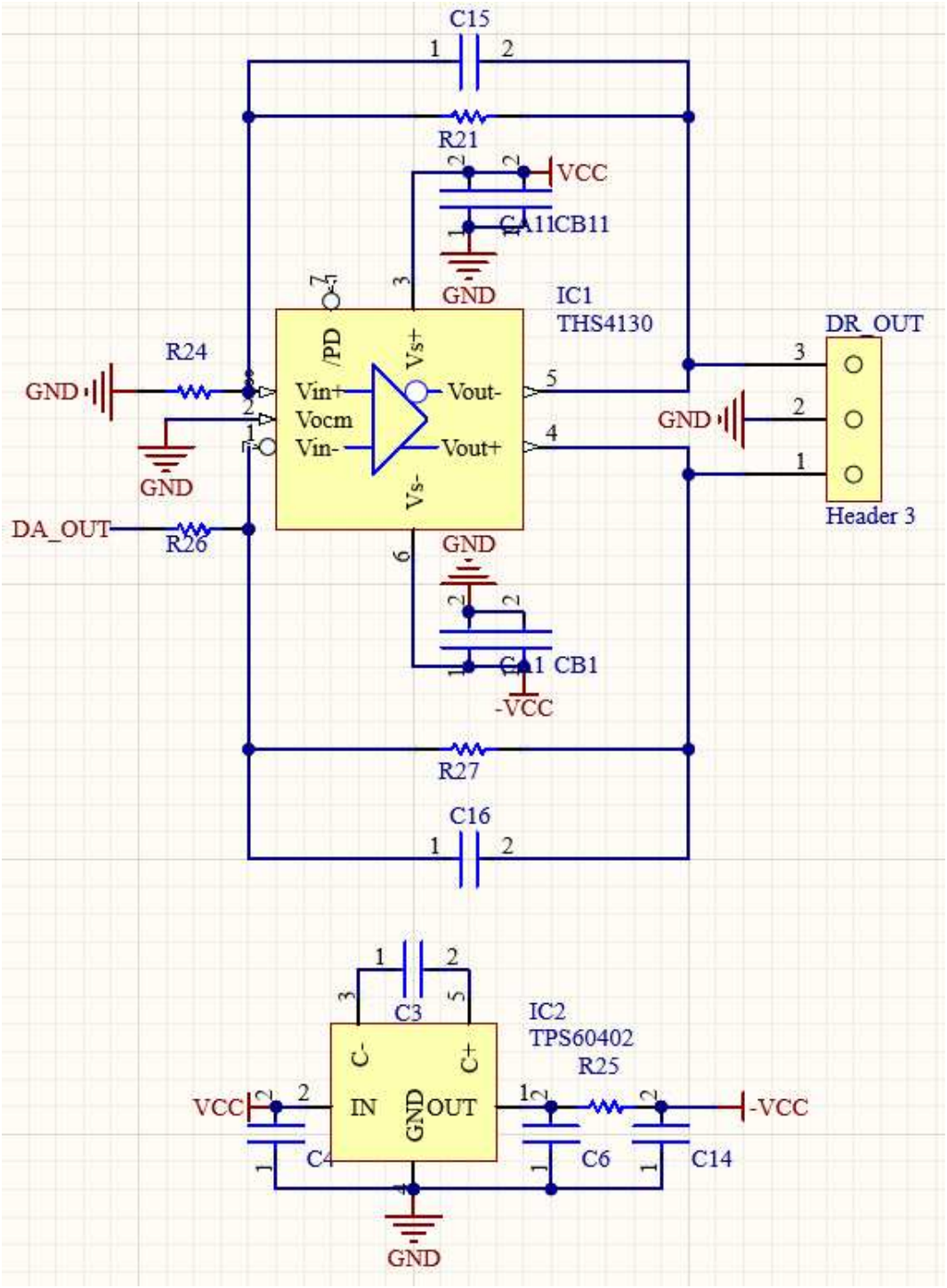

Figure B.4 – Altium Schematic - Output Wave circuit.

To deliver the sinusoidal signal that drives the tunable filter, a voltage amplifier circuit (Figure **??**) was designed. This circuit amplifies a 3.3 V peak-to-peak sine wave to 10 V using a differential driver (THS4130) powered by a charge pump circuit (TPS60402), which provides -5 V rails.

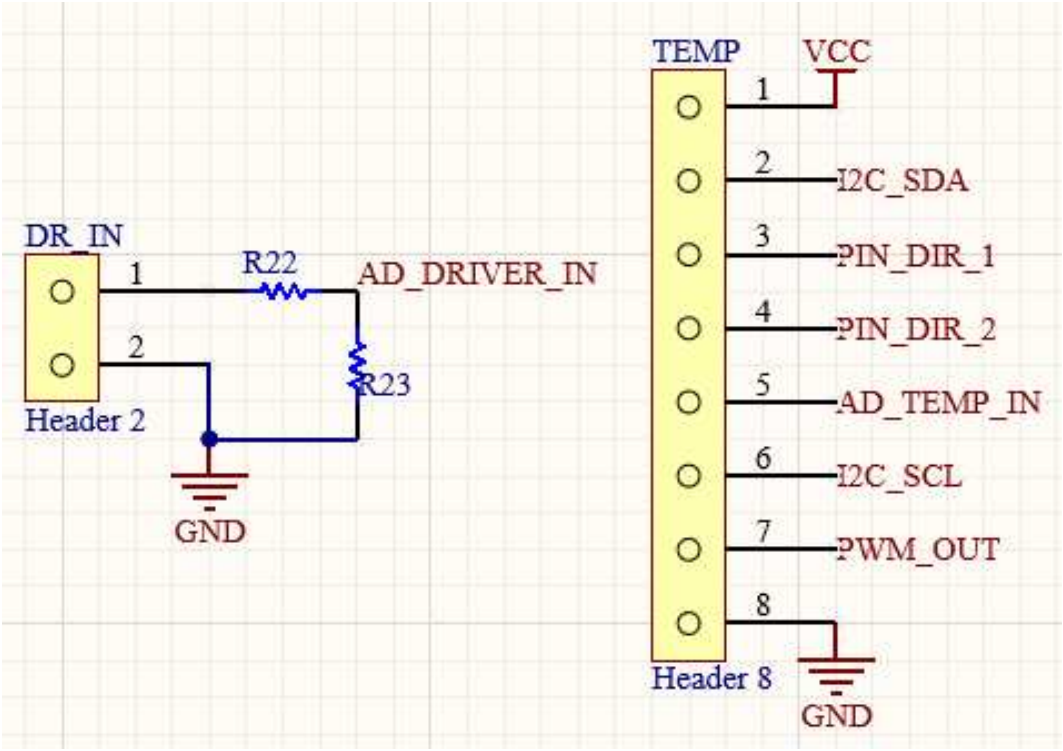

Figure B.5 – Altium Schematic - Input voltage divider and microcontroller connections.

Figure B.5 shows a voltage divider utilized to capture the instantaneous voltage generated by the external driver amplifier and reduce its amplitude to a maximum of 3.3 V. This capture is necessary to estimate the delay introduced by the driver. Additionally, several microcontroller pins are directly connected to a header to handle the input and output signals associated with the temperature controller.

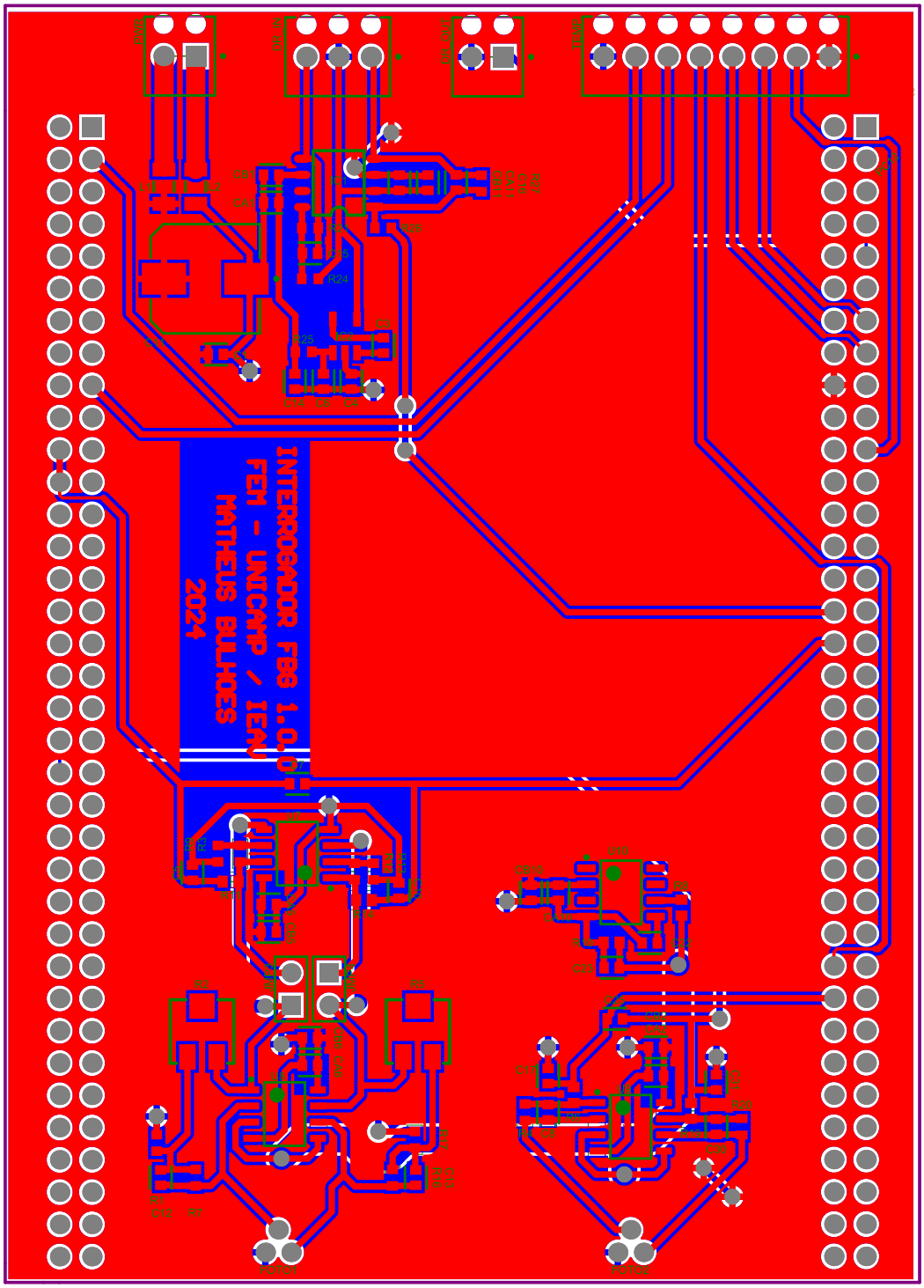

Figure B.6 – Altium PCD - Front Layout.

The PCB (Figure B.6) was designed as a two-layer board. The top layer is predominantly used for the VCC plane, signal routing and component placement, while the bottom layer is dedicated to the ground plane. The power input and filtering circuits are placed near the input header, while the reference generation and analog signal processing circuits are located

next to each other to minimize trace lengths and noise. In addition, decoupling capacitors were placed as close as possible to each integrated circuit to help stabilize the local power supply.

APPENDIX C – FBG ASSEMBLING PROCEDURE

To ensure effective mechanical coupling between the fiber Bragg grating (FBG) and the piezoelectric actuation mechanism, a careful identification and mounting process was developed. This appendix details the step-by-step methodology adopted for locating the FBG on the optical fiber and securing it with appropriate pre-tension.

The first step was to connect the fiber to an external interrogator and monitor the Bragg wavelength in real time. A fixed point along the fiber is carefully pressed, while a nearby section is slowly pulled. The first indication of a shift in the Bragg wavelength marks the location of one extremity of the FBG. Once identified, the procedure is repeated from the opposite direction while holding the first extremity fixed. By observing the spectral response, the second end is determined at the point where the spectrum ceases to deform and shifts uniformly under applied tension.

Figure C.1 – First extremity bonded and fixed with Kapton tape.

To attach the FBG to the aluminum structure of the mechanism, epoxy adhesive was used. First, the identified starting point of the grating was glued to one of the fixed surfaces of the mechanism. The epoxy was spread carefully beyond this point, always away from the grating, to ensure strong adhesion over a larger area without risking that the glue would reach and immobilize the grating itself (Figure C.1).

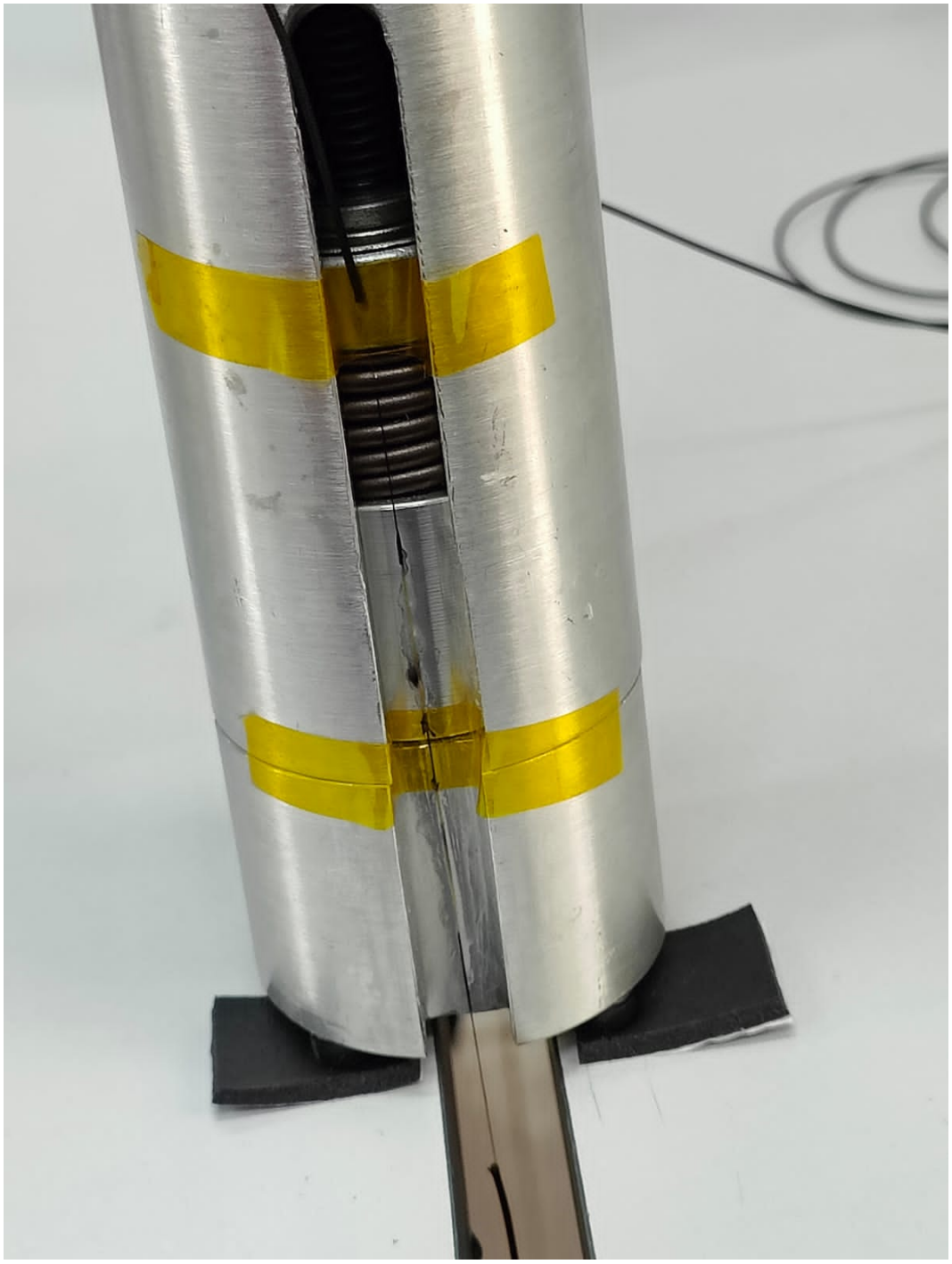

Figure C.2 – Second extremity bonded under tension with spacers beneath the mechanism.

Next, a pre-tensioning mass of 50 grams was attached to the other extremity of the fiber. This pre-load allows the mechanism to later apply compressive or tensile strain without risking mechanical slack. With the fiber under tension, the second extremity was bonded in the same manner as the first. During this step, two spacers were placed beneath the mechanism to induce a slight inclination and ensure that the entire fiber section was in full contact with the aluminum surface (Figure C.2).

During the whole the attaching process, a Kapton tape was applied over the fiber, holding it against the aluminum surface. This was done to make sure the epoxy wouldn't flow into the region where the grating is located. It was essential to keep the FBG itself unglued — otherwise, the strain wouldn't be distributed properly along the grating, and its spectral response could get distorted during operation.

This whole process ensures that the FBG stays well fixed and that the strain is applied evenly along its length, giving reliable Bragg wavelength readings when tension is applied.

Annex

ANNEX A – AN0X/8500B PZT ACTUATOR DATASHEET

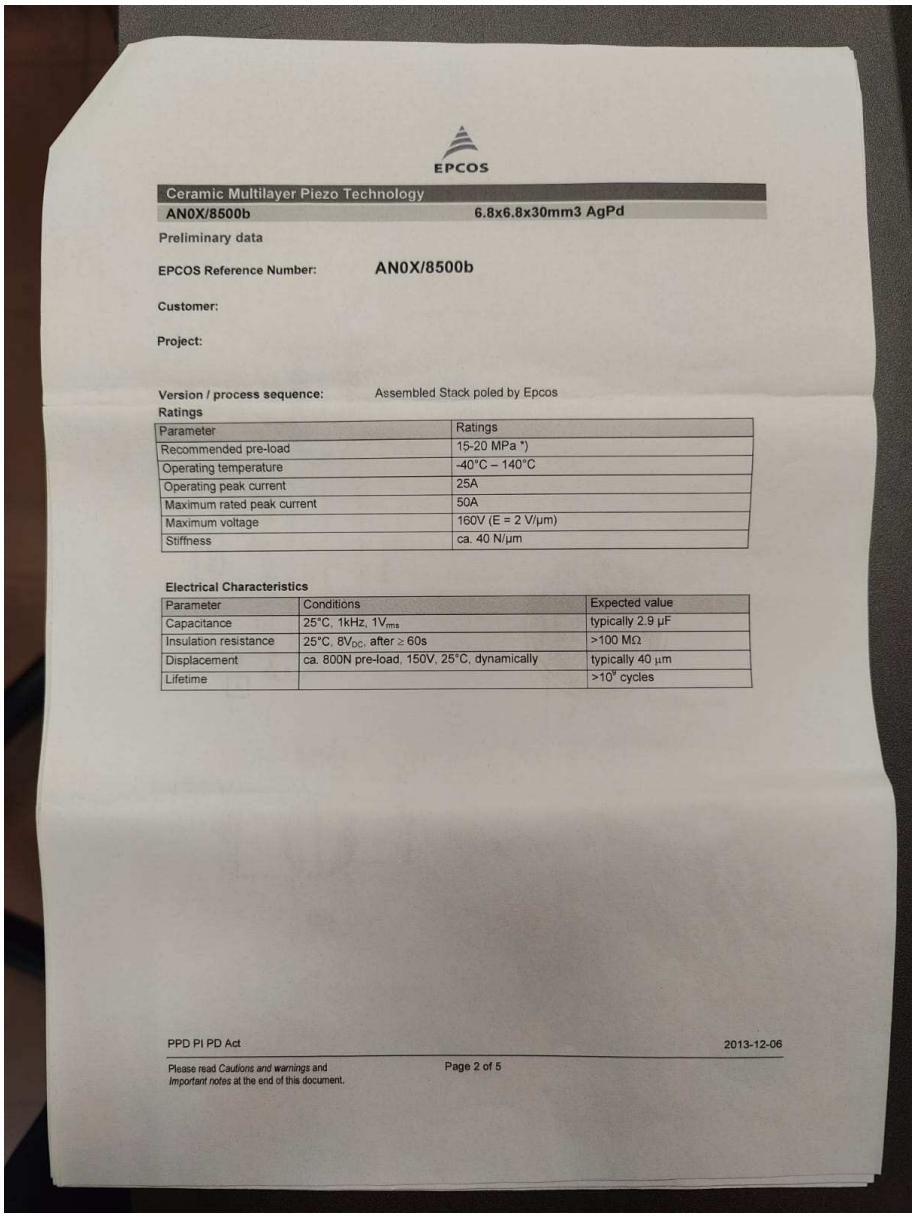

EPCOS

Ceramic Multilayer Piezo Technology

AN0X/8500b **6.8x6.8x30mm3 AgPd**

Preliminary data

EPCOS Reference Number: **AN0X/8500b**

Customer:

Project:

Version / process sequence: Assembled Stack poled by Epcos

Ratings

Parameter	Ratings
Recommended pre-load	15-20 MPa *)
Operating temperature	-40°C – 140°C
Operating peak current	25A
Maximum rated peak current	50A
Maximum voltage	160V (E = 2 V/µm)
Stiffness	ca. 40 N/µm

Electrical Characteristics

Parameter	Conditions	Expected value
Capacitance	25°C, 1kHz, $1V_{rms}$	typically 2.9 µF
Insulation resistance	25°C, $8V_{DC}$, after ≥ 60s	>100 MΩ
Displacement	ca. 800N pre-load, 150V, 25°C, dynamically	typically 40 µm
Lifetime		$>10^9$ cycles

PPD PI PD Act 2013-12-06

Please read *Cautions and warnings* and *Important notes* at the end of this document.

Page 2 of 5

Figure A.1 – PZT Datasheet